Astronomy Letters, Vol. 29, No. 6, 2003, pp. 353–360. Translated from Pis'ma v Astronomicheskiĭ Zhurnal, Vol. 29, No. 6, 2003, pp. 403–411.

Spectra and Light Curves of GRB Afterglows

A. G. Tolstov[1] and S. I. Blinnikov[1,2*]

[1] *Institute for Theoretical and Experimental Physics, ul. Bol'shaya Cheremushkinskaya 25, Moscow, 117218 Russia*

[2] *Sternberg Astronomical Institute, Universitetskiĭ pr. 13, Moscow, 119992 Russia*

Received December 20, 2002

Abstract—We performed accurate numerical calculations of angle-, time-, and frequency-dependent radiative transfer for the relativistic motion of matter in gamma-ray burst (GRB) models. Our technique for solving the transfer equation, which is based on the method of characteristics, can be applied to the motion of matter with a Lorentz factor up to 1000. The effect of synchrotron self-absorption is taken into account. We computed the spectra and light curves from electrons with a power-law energy distribution in an expanding relativistic shock and compare them with available analytic estimates. The behavior of the optical afterglows from GRB 990510 and GRB 000301c is discussed qualitatively. © *2003 MAIK "Nauka/Interperiodica".*

Key words: *plasma astrophysics, hydrodynamics, and shock waves; gamma-ray bursts.*

INTRODUCTION

The nature of the central sources of cosmic gamma-ray bursts (GRBs) has not yet been established. However, it is clear that GRBs with afterglows are at cosmological distances and release energy $\sim 10^{51}$ erg on a time scale of the order of 100 s. The observed GRB peculiarities (nonthermal spectra and rapid temporal variability) require an ultrarelativistic motion of the emitting plasma with characteristic Lorentz factors $\Gamma \sim 100$–300 (see Piran 2000; Blinnikov 2000).

In the standard GRB model (Rees and Mészáros 1992), a photon–lepton fireball is produced (see Postnov 1998; Piran 2000). Initially, however, the GRB energy can also be electromagnetic (Usov 1994; Spruit 1999; Blandford 2002), and it probably propagates in a narrow cone (jet). The observed gamma-ray photons are generated by a nonthermal mechanism at the fronts of relativistic shocks (although the apparent nonthermal spectrum can also be explained in terms of the model of optically thick shells moving at relativistic velocities; see Blinnikov *et al.* 1999).

Here, we develop a technique for solving the angle-, time-, and frequency-dependent transfer equation, which is based on the method of characteristics. It can be applied to the motion of matter with a Lorentz factor up to 1000. The main object of application of this technique must be the early generation phases of gamma-ray emission (during collisions between internal shocks), for which the optical-depth effects can be noticeable. For now, however, we consider the radiation from the matter behind the front of an external shock and use an analytic solution (Blandford and McKee 1976) to describe the postshock matter by taking into account the synchrotron self-absorption (cf. Downes *et al.* (2002), where the self-absorption was disregarded but the hydrodynamics and spectrum of the ultrarelativistic particles were computed in a self-consistent way). We computed the spectra and light curves from electrons with a power-law energy distribution in an expanding relativistic shock and compare them with available analytic estimates.

FORMULATION OF THE PROBLEM

One of the most popular models for GRB afterglows involves the propagation of a relativistic shell being decelerated by an external medium. The relativistic shock heats up the captured matter as it enters the shell and causes the particles to be accelerated to ultrarelativistic energies. The X-ray and optical afterglows from GRBs in these models are associated with the nonthermal (synchrotron) the radiation of the relativistic particles at the front of an external shock being decelerated in a circumstellar or interstellar medium (Mészáros and Rees 1997). We consider this problem in more detail by highlighting the most important points.

*E-mail: sergei.blinnikov@itep.ru

1063-7737/03/2906-0353$24.00

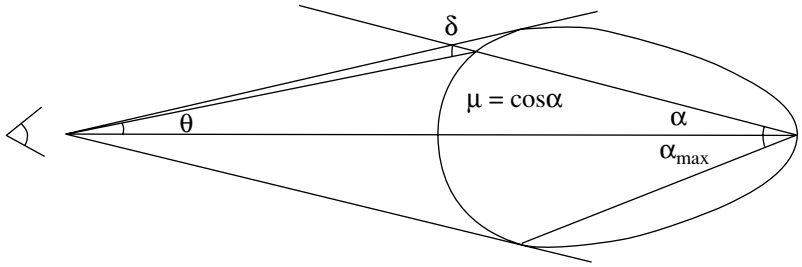

Fig. 1. The shape of the surface (the quasi-ellipsoid on the right) from which photons reach a remote observer (on the left) simultaneously. The explosion center is located at the vertex of the angle α. The farthest point of the visible surface lies at a small distance of $\sim(1-\beta)$ of the semimajor axis from the explosion center; the semiminor axis is $\sim 1/\gamma$ of the semimajor axis.

The Propagation of Radiation from a Relativistic Shell

Because of the high shock velocity, light from the ellipsoidal structure shown in Fig. 1 reaches the observer at a certain time. Let us determine the shape of the surface more accurately.

Consider an emitting spherical shell of initial radius $R(t_0) = R_0$ with an observer located at a distance D from its center. The shell begins to expand as $R = R(t)$. We assume that the time t_0 at which the shell expansion begins corresponds to the time $t_{0\mathrm{obs}}$ at which the observation begins; $t_{0\mathrm{obs}} = t_0 + (D - R_0)/c$, where c is the speed of light.

The radiation from points of a sphere with a radius depending on the cosine of the angle $\mu = \cos\alpha$ will reach the observer at some time t_{obs}. For convenience, t_{obs} is defined in such a way that it is equal to zero at the arrival time of the first signal of the shell motion. To determine the shape of the surface from which the radiation arrives, we take into account the fact that the time at which the propagation of photons from points of a sphere with a μ-dependent radius R begins is the same and specified only by t_{obs}.

In other words,

$$t + \frac{(D^2 + R^2 - 2RD\mu)^{1/2}}{c} = t_{\mathrm{obs}} + t_{0\mathrm{obs}}.$$

The surface shape can be determined from this equation by substituting in $t = R^{-1}(t)$. If we consider the simplest shell propagation equation

$$R = R_0 + \beta c(t - t_0), \quad 0 < \beta < 1,$$

where β is the v/c ratio and $\gamma = (1-\beta^2)^{-1/2}$ is the Lorentz factor, then we obtain the equation of the surface

$$\frac{R - R_0}{\beta c} + t_0 + \frac{(D^2 + R^2 - 2RD\mu)^{1/2}}{c} = t_{\mathrm{obs}} + t_{0\mathrm{obs}},$$

$$R = \frac{\beta c t_{\mathrm{obs}} + R_0(1-\beta)}{1 - \mu\beta} \quad (D \gg R).$$

As we see, in the approximation $D \gg R$, this equation is the equation of an ellipse (Rees 1967). In Fig. 1, the shape is more complex, because it corresponds to a variable velocity, as suggested by the solution of Blandford and McKee (1976).

Each point on the sphere is characterized by the intensity $I_0(\mu, r, \nu_0, \cos\delta_0)$ in the comoving frame of reference. In the observer's frame of reference, we write this intensity as $I(\mu, r, \nu, \cos\delta)$.

The intensity along the line of light propagation does not change in the absence of emission and absorption sources, and at the point of observation it will be the same as that at the point of radiation. Therefore, denoting $\mu' = \cos\theta$, we have for the flux

$$F_\nu = 2\pi \int\limits_{\cos\theta_{\max}}^{1} I(\mu, r, \nu, \cos\delta)\mu' d\mu'.$$

Here, it is more convenient to pass from integration over θ to integration over α (Fig. 1):

$$F_\nu = 2\pi \int\limits_{\mu_{\min}}^{1} I(\mu, r, \nu, \cos\delta)\mu'(\mu) d\mu'(\mu).$$

We denote $R(\mu)/D = p(\mu)$ and express $\cos\theta$ and $d\cos\theta$ in terms of $p(\mu)$ and μ. The dependence $R(\mu)$ appears in the observer's frame of reference. It should be remembered that p also depends on t and t, in turn, can be expressed in terms of t_{obs}. However, to simplify our formulas, we will omit this dependence. For our subsequent calculations, we will need the following geometrical relations between the angles:

$$\cos\theta = \frac{1 - \mu p(\mu)}{l(\mu)}, \quad d\cos\theta = p^2 \frac{\mu - p(\mu)}{l^3(\mu)},$$

$$\cos\delta = \frac{\mu - p(\mu)}{l(\mu)}, \quad \cos\delta_0 = \frac{\cos\delta - \beta}{1 - \beta\cos\delta},$$

$$\frac{\nu}{\nu_0} = \frac{1}{\gamma(\mu)(1 - \cos\delta\beta(\mu))},$$

where $l(\mu) = (1 + p^2(\mu) - 2p(\mu)\mu)^{1/2}$. For the flux, we then have

$$F_\nu(t_{\rm obs}) = 2\pi \int\limits_{\mu_{\rm min}}^{1} \frac{(\mu - p(\mu))(1 - \mu p(\mu))}{(1 + p^2(\mu) - 2p(\mu)\mu)^2} p^2 I_0 \quad (1)$$
$$\times \left(r(\mu), \nu\left(\frac{\nu_0}{\nu}\right), \cos\delta_0(\cos\delta)\right) \left(\frac{\nu}{\nu_0}\right)^3 d\mu.$$

When the flux is calculated, the condition imposed on the lower integration limit $\mu_{\rm min}$ is determined by the angle that corresponds to the maximum angular size of the shell from the point of observation:

$$p'_\mu(1 - \mu^2) - p(\mu - p) = 0.$$

Our subsequent calculations are associated with a specific expression for the intensity $I(r, \nu_0, \cos\delta_0)$ on the shell surface and a specific shell propagation law $R(t)$.

The Transfer Equation

For the intensity on the surface of a relativistic emitting shell to be calculated, we must solve the transfer equation in a comoving frame of reference. This is Eq. (2.12) from Mihalas (1980):

$$\frac{\gamma}{c}(1 + \beta\mu)\frac{\partial I(\mu,\nu)}{\partial t} + \gamma(\mu + \beta)\frac{\partial I(\mu,\nu)}{\partial r} \quad (2)$$
$$+ \gamma(1 - \mu^2)\Big[\frac{(1 + \beta\mu)}{r} - \frac{\gamma^2}{c}(1 + \beta\mu)\frac{\partial\beta}{\partial t}$$
$$- \gamma^2(\mu + \beta)\frac{\partial\beta}{\partial r}\Big]\frac{\partial I(\mu,\nu)}{\partial\mu} - \gamma\Big[\frac{\beta(1 - \mu^2)}{r}$$
$$+ \frac{\gamma^2}{c}(1 + \beta\mu)\frac{\partial\beta}{\partial t} + + \gamma^2\mu(\mu + \beta)\frac{\partial\beta}{\partial r}\Big]\nu\frac{\partial I(\mu,\nu)}{\partial\nu}$$
$$+ 3\gamma\Big[\frac{\beta(1 - \mu^2)}{r} + \frac{\gamma^2\mu}{c}(1 + \beta\mu)\frac{\partial\beta}{\partial t}$$
$$+ \gamma^2\mu(\mu + \beta)\frac{\partial\beta}{\partial r}\Big]I(\mu,\nu) = \eta(\nu) - \chi(\nu)I(\mu,\nu).$$

Here, η is the emission coefficient and χ is the absorption coefficient; the subscript 0 was omitted, because all quantities refer to the comoving frame.

Our numerical method of solution is described in the next section.

Hydrodynamics

The transfer equation (2) explicitly or implicitly (via η and χ) includes variables of the medium: its velocity, density, temperature, etc. For these variables to be determined, we must solve the system of hydrodynamic equations. In general, the transfer and hydrodynamic equations constitute a combined system of equations. In our problem, however, we solve the transfer equation separately from the hydrodynamic equations. At the same time, to determine the variables of the medium, we use a self-similar solution for a relativistic shock (with a Lorentz factor of the postshock matter $\gamma \gg 1$) in the spherically symmetric case for an ultrarelativistic gas (Blandford and McKee 1976). Let us give the formulas of this solution that we will need below.

Taking the law of time variations in the shock-front Lorentz factor in the form $\Gamma^2 \propto t^{-m}$ and choosing, for convenience, the self-similar variable $\zeta = [1 + 2(m + 1)\Gamma^2](1 - r/t)$, we derive the following expressions for the pressure, velocity, and density of the postshock matter from the conditions at the shock front:

$$p = \frac{2}{3}w_1\Gamma^2 f(\zeta), \qquad \gamma^2 = \frac{1}{2}\Gamma^2 g(\zeta), \qquad (3)$$
$$n' = 2n_1\Gamma^2 h(\zeta).$$

Here, w_1 is the enthalpy of the preshock matter, n_1 is its density, Γ is the shock-front Lorentz factor, and n' is the density of the post-shock matter in the observer's frame of reference. The matter density in the comoving frame of reference is related to the latter by $n' = \gamma n$.

Substituting Eqs. (3) into the hydrodynamic equations yields a system of equations for $f(\zeta)$, $g(\zeta)$, and $h(\zeta)$ parameterized by m. Consider the case $m = 3$, which corresponds to the conservation of total shell energy. The shock energy contained in the layer between the radii $R_0(t)$ and $R_1(t)$ is given by the expression

$$E(R_0, R_1, t) = \int\limits_{R_0}^{R_1} 16\pi p\gamma^2 r^2 dr.$$

If we substitute in the solution for the functions $f(\zeta)$, $g(\zeta)$, and $h(\zeta)$ at $m = 3$:

$$f = \zeta^{-17/12}, \quad g = \zeta^{-1}, \quad h = \zeta^{-7/4}, \qquad (4)$$

then the total energy will be $E = 8\pi w_1 \times \times t^3\Gamma^2/17$, which gives the proportionality constant between Γ^2 and t^{-3}.

Synchrotron Radiation

An accurate calculation of the spectrum requires knowing not only the hydrodynamic quantities but also the electron energy spectrum and the magnetic-field strength.

We assume that the electrons have a power-law distribution and that their total energy behind the

shock front accounts for a fraction ϵ_e of the internal energy:

$$N(\gamma) = K_0\gamma^{-p}, \gamma \geq \gamma_{\min,0} = \frac{\epsilon_e e_0}{n_0 m_e c^2},$$

where m_e is the electron rest mass and $K_0 = (p-1)n_0\gamma_{\min,0}^{p-1}$.

The magnetic field is parameterized by the quantity ϵ_B, which is equal to the fraction of the internal energy contained in the magnetic field: $B^2 = 8\pi\epsilon_B e$. The magnetic field is randomly oriented and decreases with time due to the adiabatic shell expansion. Other assumptions about the magnetic-field evolution and orientation weakly affect the resulting spectrum (Granot 1999).

After the electrons have derived energy immediately behind the shock front, they begin to lose it through adiabatic cooling determined by the solution of Blandford and McKee (1976) and through synchrotron radiation. This process was described in more detail by Granot and Sari (2001). We present only the basic formulas for synchrotron radiation used in our calculations.

The spectral power of a single electron averaged over the pitch angle is

$$P(\omega) = \frac{3^{5/2}}{8\pi}\frac{P_{\text{sync}}}{\omega_c}F\Big(\frac{\omega}{\omega_c}\Big),$$

where

$$P_{\text{sync}} = \frac{1}{6\pi}\sigma_T c B^2(\gamma_e^2 - 1), \quad \omega_c = \frac{3\pi}{8}\frac{eB}{m_e c}\gamma_e^2$$

and $F(u)$ is the standard function of synchrotron radiation (Rybicki and Lightman 1979). The synchrotron absorption coefficient is specified by the formula

$$\chi = \frac{1}{8\pi m_e \nu^2}\int\limits_{\gamma_{\min}}^{\gamma_{\max}} d\gamma \frac{N(\gamma)}{\gamma^2}\frac{d}{d\gamma}\Big(\gamma^2 P(\omega,\gamma)\Big).$$

NUMERICAL SOLUTION OF THE TRANSFER EQUATION

The numerical solution of the problem is based on the simple and well-known method of characteristics (Mihalas 1980). We consider the relativistic transfer equation (2) in the spherically symmetric case in a comoving frame of reference.

The main complexity of the equation is the presence of four independent variables. The linearity of the equation allows its complexity to be decreased by constructing the characteristics for a given velocity field along which the differential operator is a total differential. If we choose the rays by describing them by a set of parameters and define s as some length along the ray, then we can determine the characteristics, the paths $[t(s), r(s), \mu(s), \nu(s)]$, in such a way that

$$\frac{dI}{ds} = \frac{dr}{ds}\frac{\partial I}{\partial r} + \frac{d\mu}{ds}\frac{\partial I}{\partial \mu} + \frac{d\nu}{ds}\frac{\partial I}{\partial \nu} + \frac{dt}{ds}\frac{\partial I}{\partial t}.$$

We then derive the following system of equations that describe the characteristics from Eq. (2):

$$\frac{dt}{ds} = \frac{\gamma}{c}(1+\beta\mu),$$
$$\frac{dr}{ds} = \gamma(\mu+\beta),$$
$$\frac{d\mu}{ds} = \gamma(1-\mu^2)\Big[\frac{1+\beta\mu}{r} - \frac{\gamma^2}{c}(1+\beta\mu)\frac{\partial\beta}{\partial t} - \gamma^2(\mu+\beta)\frac{\partial\beta}{\partial r}\Big],$$
$$\frac{d\nu}{ds} = \gamma\Big[\frac{\beta(1-\mu^2)}{r} + \frac{\gamma^2}{c}(1+\beta\mu)\frac{\partial\beta}{\partial t} + \gamma^2\mu(\mu+\beta)\frac{\partial\beta}{\partial r}\Big]\nu.$$

With the introduction of the characteristic rays, the transfer problem simplifies to

$$\frac{dI(s)}{ds} = \eta(s) - \chi'(s)I(s),$$

where

$$\chi'(s) = \chi(s) + 3\gamma\Big[\frac{\beta(1-\mu^2)}{r} + \frac{\gamma^2\mu}{c}(1+\beta\mu)\frac{\partial\beta}{\partial t} + \gamma^2\mu(\mu+\beta)\frac{\partial\beta}{\partial r}\Big].$$

The characteristics are numerically computed by the fourth-order Runge–Kutta method with an adaptive step. The step is adaptive, because for β close to unity, a small increment along the ray can lead to a significant angular jump comparable to the angular size of the emitting region.

Note also that the variable quantities in the method must be of the order of unity, as follows from the constraint imposed on the cosine of the angle. Therefore, it is convenient to use a new system of units. We denote the physical and dimensionless (used in the program) quantities by the subscripts r and p, respectively. So, let

$$r_r = Rr_p, \quad t_r = Tt_p, \quad m_r = Mm_p.$$

Denoting

$$c_r = Cc_p, \quad I_r = YI_p,$$
$$\eta_r = J\eta_p, \quad \chi_r = X\chi_p,$$

where c is the speed of light and R, T, C, Y, J,and X are constants, we then derive the following expression

for C, Y, J, and X in terms of R, T, and M after simple work with the dimensions:

$$C = RT^{-1}, \quad Y = MT^{-2},$$
$$J = MR^{-1}T^{-2}, \quad X = R^{-1}.$$

The Analytic Solutions Used to Test the Numerical Method

Below, we give some of the analytic solutions that we used to test the numerical method.

Let us first consider the time- and frequency-independent transfer equation (2):

$$\gamma(\mu+\beta)\frac{\partial I(r,\mu)}{\partial r} + \gamma(1-\mu^2) \times \Big[\frac{1+\mu\beta}{r} - \gamma^2(\mu+\beta)\frac{\partial\beta}{\partial r}\Big]\frac{\partial I(r,\mu)}{\partial\mu} + 3\gamma\Big[\frac{\beta(1-\mu^2)}{r} + \gamma^2\mu(\mu+\beta)\frac{\partial\beta}{\partial r}\Big]I(r,\mu) = \eta(r,\mu) - \chi(r,\mu)I(r,\mu).$$

For constant emission and absorption coefficients and $\beta = 0$, the characteristics have the shape of straight lines $r\sqrt{1-\mu^2} = p$ (p is the parameter) and the equation has the analytic solution

$$I(r,\mu) = \frac{\eta}{\chi}\Big[1 - \exp\Big\{-\chi\Big(\mu r + \sqrt{R^2 - r^2(1-\mu^2)}\Big)\Big\}\Big].$$

If we now assume β to be constant, then the shape of the characteristics changes: $p(1+\beta\mu) = r\sqrt{1-\mu^2}$, and the solution becomes slightly more complex,

$$I(s) = I(r,\mu) = \frac{\eta}{\chi}\Big\{1 - \exp\Big[-\chi\Big(\frac{\gamma\mu r}{1+\beta\mu} - \frac{\gamma\xi(p)R}{1+\beta\xi(p)}\Big)\Big]\Big\},$$

where

$$\xi(p) = \frac{-\beta p^2 - \sqrt{\beta^2p^4 + (R^2+\beta p^2)(R^2-p^2)}}{R^2+\beta^2p^2}.$$

In the absence of absorption and for a constant emission coefficient on the right-hand side of the transfer equation, the analytic solution for the central characteristic ($\mu = \pm 1$) is

$$I(0) = \frac{\eta R}{\gamma(1-\beta)}, \qquad I(R) = 2\eta R\gamma,$$

at $\beta = \text{const}$ and

$$I(0) = \eta R\Big[2\frac{\ln(1+B)}{B} - 1\Big],$$
$$I(R) = 2\eta R\Big(\frac{1-B}{1+B}\Big)^{3/2}\Big[\frac{1}{B}\ln\frac{1+B}{1-B} - 1\Big],$$

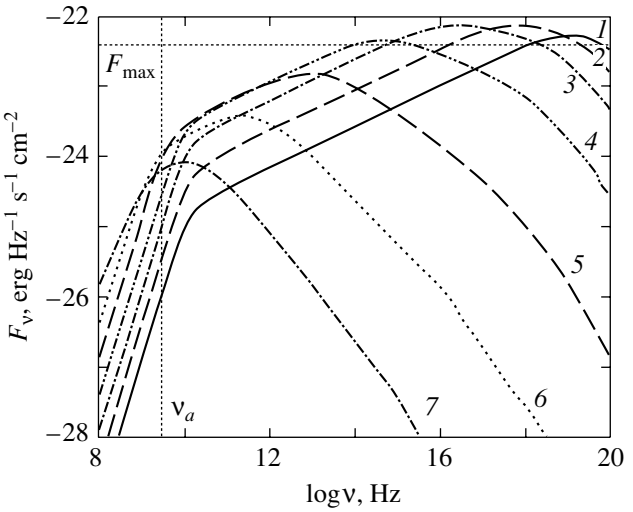

Fig. 2. Instantaneous afterglow spectra at various times $t = 10^N$ s, where N is the number near the curve; F_m and ν_a are the analytically estimated flux and self-absorption frequency, respectively.

where $B = \beta(R)$, at $\beta \sim r$.

To test the temporal component, we used the problem of the change in intensity near the surface of an emitting static transparent spherical shell with time when the emission coefficient abruptly changes from η_0 to η_1. If we use the notation $p = R/D$ is the ratio of the shell radius to the distance from the shell center to the point of observation, t_+ is the time measured from the beginning of the intensity change at the point of observation, c is the speed of light, $\tau = t_+c/D$, and $d = 1 - p + \tau$, then the solution for this problem is

$$F_1(\tau) = G_1(\eta_1,(1-p)^2) - G_1(\eta_1,d^2) + G_1(\eta_0,d^2) - G_1(\eta_0,1-p^2),$$

$$G_1(\eta,x) = \frac{\pi\eta R}{4p}\Big[\frac{2}{3}\frac{(1-p^2)^3}{x^{3/2}} - 2\frac{(1-p^2)^2}{x^{1/2}} + 2(1-p^2)x^{1/2} - \frac{2}{3}x^{3/2}\Big].$$

Here, τ changes from 0 to $\tau^* = \sqrt{1-p^2} - 1 + p$, i.e., within the interval during which the changes at the point of observation occur, and $F_1(\tau)$ is the flux. In the static case, this flux is

$$F = 2\pi\int_0^p \frac{(\mu-p)(1-\mu p)p^2}{(1+p^2-2p\mu)^2} I(\mu^*)\,d\mu,$$

where

$$\mu^* = \frac{\mu-p}{(1+p^2-2p\mu)^{1/2}}$$

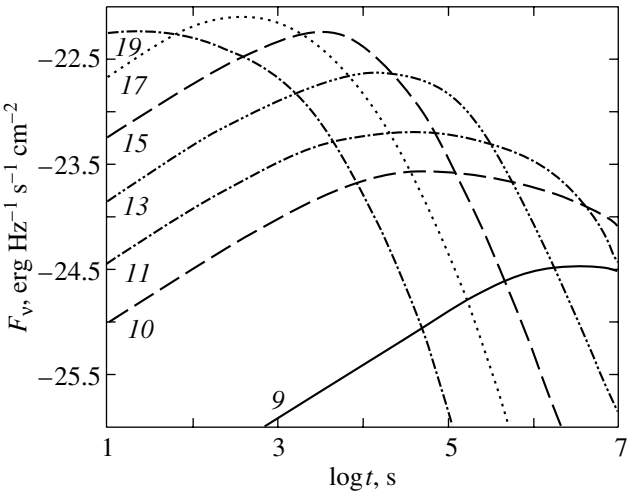

Fig. 3. Afterglow light curves for a set of frequencies $\nu = 10^N$ Hz, where N is the number near the curve.

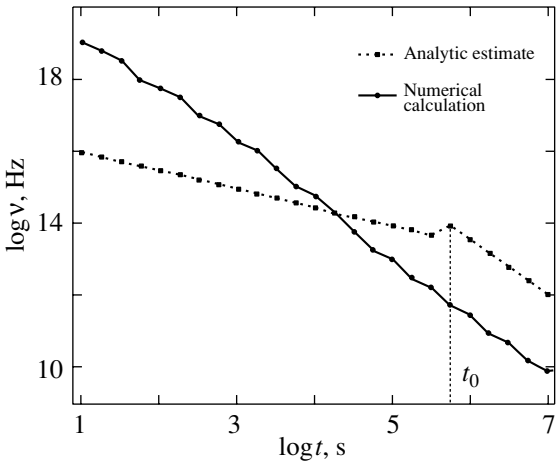

Fig. 4. Comparison of the frequencies that correspond to the maximum flux of the instantaneous spectra in the numerical calculations and analytic estimates.

is the cosine of the angle to the normal to the sphere surface on which the intensity depends.

Comparison of the solutions considered above with the calculations based on our numerical method shows that the numerical method is applicable to the motion of matter up to Lorentz factors $\gamma \sim 1000$ with an error of less than 1%.

RESULTS OF THE NUMERICAL SOLUTION

We chose the following parameters for our numerical calculations of the afterglow spectra. These include the parameters that describe the hydrodynamics: the energy E_0 released through the process that leads to a GRB and the ambient density n_1; the parameters that describe the radiation: the fraction of the internal energy contained in the magnetic field ϵ_B, the fraction of the internal energy transferred to electrons ϵ_e, and the power-law index in the electron energy distribution p; and one more parameter: the photometric distance to the GRB D.

Our main calculation, whose results are presented here, is based on the following published parameters: $E_0 = 10^{53}$ erg, $n_1 = 1\,\mathrm{cm}^{-1}$, $\epsilon_e = 0.5$, $\epsilon_B = 0.1$, $p = 2.5$, and $D = 10^{27}$ cm.

The large amount of released energy E_0 is related to the spherical symmetry of the problem, while the observed GRBs can represent a jet with a solid angle Ω. The total energy will then be lower by a factor of $\Omega/4\pi$.

The computed spectra and light curves are shown in Figs. 2 and 3. Here and below, the time is measured in the observer's frame of reference. Let us compare our results with available theoretical estimates (Hurley *et al.* 2002). In these estimates, the synchrotron spectrum is described by the maximum flux $F_{\max}$ and three characteristic frequencies ($\nu_{\min}, \nu_{\mathrm{cool}}, \nu_a$), where $\nu_{\min}$ is the synchrotron frequency of the electron with minimum energy whose Lorentz factor is $\gamma_{\min,0}$, ν_{cool} is the cooling frequency, and ν_a is the self-absorption frequency. For these four parameters, the theoretical estimates are given by the formulas

$$\nu_a = 2\times10^9\ \mathrm{Hz}\ E_{52}^{1/5} n_1^{3/5} \epsilon_e^{-1} \epsilon_B^{1/5} = 4\times10^9\ \mathrm{Hz},$$

$$\nu_{\mathrm{cool}} = 9\times10^{12}\ \mathrm{Hz}\ E_{52}^{-1/2} n_1^{-1} \epsilon_B^{-3/2} t_{\mathrm{day}}^{-1/2}$$

$$= 2.66\times10^{16}\ \mathrm{Hz}\ t_{\mathrm{s}}^{-1/2},$$

$$\nu_{\min} = 5\times10^{15}\ \mathrm{Hz}\ E_{52}^{1/2} \epsilon_e^2 \epsilon_B^{1/2} t_{\mathrm{day}}^{-3/2}$$

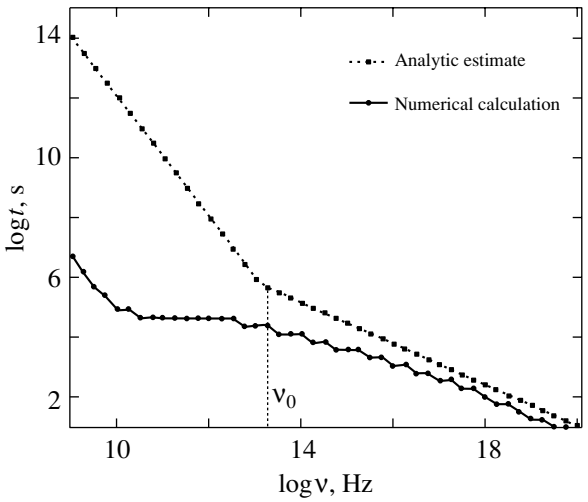

Fig. 5. Comparison of the times that correspond to the maximum flux of the light curves in the numerical calculations and analytic estimates.

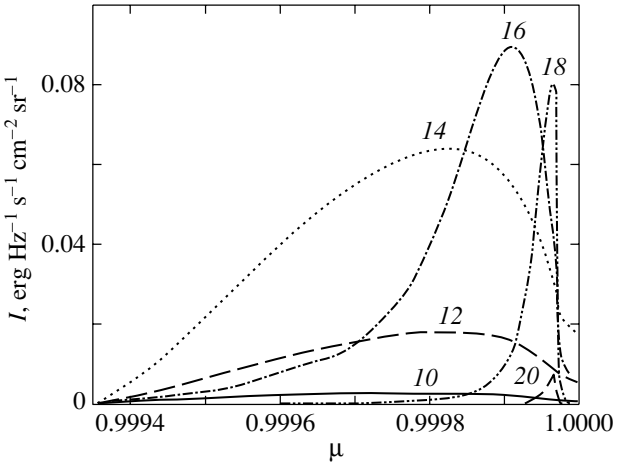

Fig. 6. The intensity on the radiation surface for a set of frequencies $\nu = 10^N$ Hz, where N is the number near the curve.

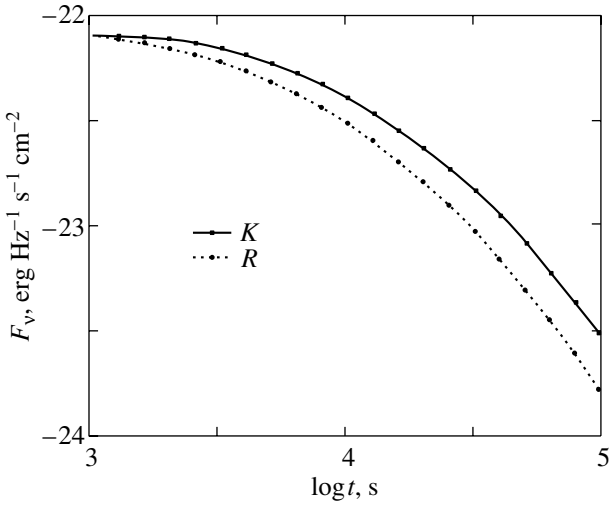

Fig. 7. Part of the theoretical light curve near the R and K bands.

$$= 3.80 \times 10^{22}\ \text{Hz}\ t_{\rm s}^{-3/2},$$

$$F_{\rm max} = 20\ \text{mJy}\ E_{52} n_1^{1/2} \epsilon_B^{1/2} d_{28}^{-2} = 6.32 \times 10^{-23}\ \text{mJy}.$$

Between these frequencies, the spectrum is a power law with indices $(2, 1.3, -1/2, -p/2)$ for $t < t_0 = 4.2 \times 10^5$ s and $(2, 1.3, -(p-1)/2, -p/2)$ for $t > t_0$.

Let us also compare the computed light curves with theoretical estimates (Sari *et al.* 1998), in which the characteristic times $(t_{\rm min}, t_{\rm cool})$ were calculated from the flux $F_{\rm max}$ and the characteristic frequencies $(\nu_{\rm min}, \nu_{\rm cool}, \nu_a)$:

$$t_{\rm cool} = 7.3 \times 10^{-6} E_{52}^{-1} n_1^{-2} \epsilon_B^{-3} \nu_{15}^2\ \text{day} = 63 \nu_{15}^{-2}\ \text{s},$$

$$t_{\rm min} = 0.69 E_{52}^{1/3} \epsilon_e^{4/3} \epsilon_B^{1/3} \nu_{15}^{-2/3}\ \text{day}$$

$$= 2.37 \times 10^4 \nu_{15}^{-2/3}\ \text{s}.$$

By introducing the frequency $\nu_0 = \nu_{\rm cool}(t_0) = t_{\rm min}(t_0) = 1.14 \times 10^{13}$ Hz, we separate two cases: $t_{\rm min} < t_{\rm cool}$ for $\nu > \nu_0$ and $t_{\rm min} > t_{\rm cool}$ for $\nu < \nu_0$.

The results of our comparison are presented in Figs. 4 and 5. These figures show the frequencies for the spectra and the times for the light curves that correspond to the maximum flux calculated numerically and analytically, in accordance with the above estimates.

The plot of afterglow intensity versus observation angle $(\alpha \sim \theta)$ (Fig. 6) at different frequencies reveals a bright ring attributable to the hotter matter at the early afterglow stages. The higher the radiation frequency, the larger the contrast between the center and the edge of the image. The same result was obtained by Granot *et al.* (1999).

The GRB energy must be released in a narrow cone, a jet. However, at early stages, the pattern for an observer near the cone axis will differ only slightly from the pattern produced by a spherical shock. At late stages, the jet becomes spherical.

In Fig. 7, the part of the theoretical light curve near the R and K bands is highlighted. We see that the light curve goes into a decline more slowly at longer wavelengths than it does at shorter wavelengths. This chromatic behavior is characteristic of the optical afterglows from GRB 990510 (Stanek *et al.* 1999) and GRB 000301c (Jensen *et al.* 2001).

These objects deserve more detailed study, but so far our model disregards several physical effects (inverse Compton radiation, the Klein–Nishina effect, the non-power-law shape of the self-consistent electron spectrum, and others). Therefore, it cannot be directly used to interpret the spectra of early GRB afterglows. The work to take these effects into account is continuing.

CONCLUSIONS

The most popular method for analytically estimating the spectra and light curves of GRB afterglows involves deriving the characteristic frequencies and times, determining their behavior, and calculating the corresponding flux and constructing the power-law segments of the spectra and light curves from the derived values. These methods are extensively presented in the literature (Granot and Sari 2001; Sari *et al.* 1998; Wijers and Galama 1999; Waxman 1997). The characteristic frequencies in different papers of the same cases occasionally differ by a factor of 70, including those of the same authors, suggesting that these treatments are insufficient.

Our calculations unambiguously describe the afterglow spectra and light curves in terms of the model

under consideration by removing the uncertainty in the characteristic parameters and without using the subsequent approximations. The behavior of our results shows a relationship to the observed afterglows, which gives us confidence that our technique can be used to study the early generation phases of gamma-ray emission (during collisions between internal shocks).

ACKNOWLEDGMENTS

This study was supported by the Russian Foundation for Basic Research (project no. 02-02-16500). We are grateful to K.A. Postnov and D.K. Nadyozhin for valuable discussions.

REFERENCES

1. R. Blandford, *Lighthouses of the Universe*, Ed. by M. Gilfanov, R. Sunyaev, E. Churasov (Springer, Berlin, 2002), p. 381.
2. R. D. Blandford and C. F. McKee, Phys. Fluids **19**, 1130 (1976).
3. S. I. Blinnikov, Surv. High Energy Phys. **15**, 37 (2000); astro-ph/9911138.
4. S. I. Blinnikov, A. V. Kozyreva, and I. E. Panchenko, Astron. Zh. **76**, 838 (1999) [Astron. Rep. **43**, 739 (1999)].
5. T. P. Downes, P. Duffy, and S. S. Komissarov, Mon. Not. R. Astron. Soc. **332**, 144 (2002).
6. K. Hurley, R. Sari, and S. G. Djorgovski, astro-ph/0211620 (2002).
7. J. Granot and R. Sari, Astrophys. J. **568**, 820 (2002).
8. J. Granot, T. Piran, and R. Sari, Astrophys. J. **527**, 236 (1999).
9. B. L. Jensen, J. U. Fynbo, J. Gorosabel, *et al.*, Astron. Astrophys. **370**, 909 (2001).
10. P. Mészáros and M. J. Rees, Astrophys. J. **476**, 232 (1997).
11. D. Mihalas, Astrophys. J. **237**, 574 (1980).
12. T. Piran, Phys. Rep. **333**, 529 (2000).
13. K. A. Postnov, Usp. Fiz. Nauk **169**, 545 (1998) [Phys.-Usp. **42**, 469 (1998)].
14. M. J. Rees, Mon. Not. R. Astron. Soc. **135**, 345 (1967).
15. M. J. Rees and P. Mészáros, Mon. Not. R. Astron. Soc. **258**, P41 (1992).
16. G. B. Rybicki and A. P. Lightman, *Radiative Processes in Astrophysics* (Wiley, New York, 1979).
17. R. Sari, T. Piran, and R. Narayan, Astrophys. J. Lett. **497**, L17 (1998).
18. H. Spruit, Astron. Astrophys. **341**, L1 (1999).
19. K. Z. Stanek, P. M. Garnavich, J. Kaluzny, *et al.*, Astrophys. J. Lett. **522**, L39 (1999).
20. V. V. Usov, Mon. Not. R. Astron. Soc. **267**, 1035 (1994).
21. E. Waxman, Astrophys. J. Lett. **489**, L33 (1997).
22. R. A. M. J. Wijers and T. J. Galama, Astrophys. J. **523**, 177 (1999).

Translated by V. Astakhov

Astronomy Letters, Vol. 29, No. 6, 2003, pp. 361–362. Translated from Pis'ma v Astronomicheskiĭ Zhurnal, Vol. 29, No. 6, 2003, pp. 412–413.

The Coincidence of Friedmann Integrals

O. B. Karpov*

Moscow State Mining University, Moscow, 119991 Russia

Received January 15, 2003

Abstract—The expansion of a two-component Universe with an arbitrary spatial curvature is considered. It is shown that the Friedmann integrals of an almost flat Universe do not coincide. © *2003 MAIK "Nauka/Interperiodica".*

Key words: *theoretical and observational cosmology, expansion of Universe, cosmic coincidences.*

The photometric distance–redshift relation for type Ia supernovae is known to reveal an acceleration of the cosmological expansion (Riess *et al.* 1998; Perlmutter *et al.* 1999). The latter is possible if there is a cosmological repulsion, which is usually described by the Λ term in the Einstein equations or, equivalently, by the presence of a vacuumlike medium with a negative pressure. The expansion becomes accelerated when the doubled vacuum density exceeds the decreasing matter density. These two components are described by two evolution constants of the Universe called Friedmann integrals. Recently, Chernin (2001, 2002) has claimed that the coincidence of the Friedmann integrals should be added to the well-known cosmic coincidences (Garriga and Vilenkin 2001) and investigated the possible causes and effects of this coincidence. In this paper, we show that the Friedmann integrals of our almost flat Universe do not and cannot coincide.

The dynamics of the two-component Universe is described by the Einstein field equation for the expansion factor a:

$$\dot{a}^2 = \frac{A_m}{a} + \frac{a^2}{A_v^2} - k, \qquad (1)$$

where $k = 1$, 0, and -1 for positive, zero, and negative spatial curvature in a frame comoving with the cosmological expansion. The factor a has the meaning of the radius of space curvature for $k = \pm 1$ and is defined to within an arbitrary scale transformation for the flat Universe $k = 0$. Below, we use a system of units with $c = 1$.

The Friedmann integrals A_m and A_v,

$$A_m = \frac{8\pi}{3} G\rho_m a^3, \quad A_v^{-2} = \frac{8\pi}{3} G\rho_v = \frac{\Lambda}{3}, \qquad (2)$$

determine the evolution of the Universe. Here, ρ_m is the matter density, including hidden mass (dark matter); ρ_v is the vacuum energy density; Λ is the cosmological constant; and G is the gravitational constant. Denote

$$U_m = -\frac{A_m}{a}, \quad U_v = -\frac{a^2}{A_v^2}, \quad U = U_m + U_v.$$

The functions $U_m(a)$, $U_v(a)$, and $U(a)$ are plotted in the figure.

For $k = 1$, the Friedmann integral A_m is the maximum radius of curvature in the standard $\Lambda = 0$ model; the integral A_v is equal to the initial value of a in the de Sitter Universe $\rho_m = 0$. At the point $a = \tilde{a}$,

$$\tilde{a}^3 = \frac{1}{2} A_m A_v^2, \qquad (3)$$

the maximum $\tilde{U}$ of the potential barrier $U(a)$ is located:

$$\tilde{U} = U(\tilde{a}) = -\left(\frac{\alpha A_m}{A_v}\right)^{2/3}, \qquad (4)$$

where $\alpha = 3\sqrt{3}/2$. At this point, a balance between matter gravitation and vacuum antigravitation is reached, $\rho_m = 2\rho_v$, and the deceleration parameter q changes its sign:

$$q = -\frac{\ddot{a}a}{\dot{a}^2} = \frac{\tilde{a}^3 - a^3}{a^3 - aA_v^2 + 2\tilde{a}^3}. \qquad (5)$$

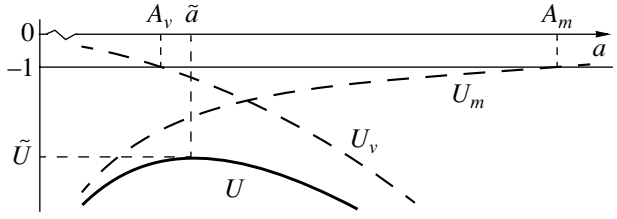

A potential barrier and the Friedmann integrals.

*E-mail: karpov@msmu.ru

1063-7737/03/2906-0361$24.00

The density parameters are $\Omega_m = \rho_m/\rho_c$ and $\Omega_v = \rho_v/\rho_c$, where ρ_c is the critical density, $\rho_c = 3H^2/8\pi G$, $H = \dot{a}/a$ is the Hubble constant. The Einstein field equation (1) relates the density parameters and the Friedmann integrals by

$$(\Omega - 1)^3 = \left(\frac{A_v}{A_m}\right)^2 \Omega_m^2 \Omega_v k^3, \qquad (6)$$

where Ω is the total density parameter, and $\Omega = 1$ for the flat universe; in model (1), $\Omega = \Omega_m + \Omega_v$.

As we see from the figure, the Friedmann integrals coincide if the point of intersection of the $U_m(a)$ and $U_v(a)$ curves is at the level $U = -1$. If the $U = -1$ level line passes through the vertex of the potential barrier, then $A_v = \alpha A_m$. For $|\tilde{U}| > 1$, i.e., when $A_v > \alpha A_m$, the closed universe cannot overcome the potential barrier and cannot expand with acceleration.

According data from Chernin (2001, 2002), A_v differs from A_m by no more than an order of magnitude;[1] $A_v > A_m$ and the scale factor a_0 is currently equal to A_v. For our almost flat Universe, $\Omega_v \simeq 0.7$ and $\Omega_m \simeq 0.3$. As we see from relation (6), irrespective of the curvature sign, the ratio of the Friedmann integrals A_v/A_m is related to the degree of spatial flatness of the Universe: $\Omega \to 1 \Leftrightarrow A_v/A_m \to 0$, and the vertex of the potential barrier $\tilde{U}$ (4) goes downward from the $U = -1$ level. For this reason, a_0 and A_v for the almost flat Universe are not equal either:

$$\left(\frac{a_0}{A_v}\right)^3 = \frac{\Omega_v}{\Omega_m}\frac{A_m}{A_v} \gg 1, \qquad (7)$$

and $a/A_v \to \infty$ when $\Omega \to 1$. In this case,

$$\left(\frac{a_0}{A_m}\right)^3 = \frac{\Omega_v}{\Omega_m}\frac{A_v}{A_m} \ll 1. \qquad (8)$$

The latest data on the cosmic microwave background anisotropy constrain the spatial curvature of the Universe (Benoit *et al.* 2002): $|\Omega - 1| \leq 0.03$. According to (6), this corresponds to $A_v/A_m \leq 2 \times 10^{-2}$. We emphasize that the foregoing assertions regarding the ratio of the Friedmann integrals are valid for $k = \pm 1$. A flat space is the limiting case of a curved space where $A_v/A_m \to 0$. The latter can also be seen from the fact that A_v does not depend on the radius of curvature and $A_m \propto a^3$ (2). For the formally flat Universe when $k = 0$, Eq. (6) turns into an identity and the parameter a in Eq. (1) becomes an arbitrary scale factor. Redefining the latter, we can make A_m arbitrary and the ratio of the Friedmann integrals becomes meaningless.

REFERENCES

1. A. Benoit, P. Ade, A. Amblard, *et al.*, astro-ph/0210306.
2. A. D. Chernin, Usp. Fiz. Nauk **171**, 153 (2001).
3. A. D. Chernin, New Astron. **7**, 113 (2002).
4. J. Garriga and A. Vilenkin, Phys. Rev. D **64**, 023517 (2001).
5. S. Perlmutter, G. Aldering, G. Goldhaber, *et al.*, Astrophys. J. **517**, 565 (1999).
6. A. G. Riess, A. V. Philipenko, P. Challis, *et al.*, Astron. J. **116**, 1009 (1998).

Translated by O. Karpov

[1] In Chernin (2002), the dark-matter Friedmann integral A_D is related to the integral A_m (2) by the relation $A_m = 2A_D$.

Astronomy Letters, Vol. 29, No. 6, 2003, pp. 363–371. Translated from Pis'ma v Astronomicheskiĭ Zhurnal, Vol. 29, No. 6, 2003, pp. 414–423.

Photometry of the Low-Luminosity Spiral Galaxy NGC 4136

A. S. Gusev[1,2*], A. V. Zasov[1], and S. S. Kaisin[3***]**

[1] *Sternberg Astronomical Institute, Universitetskii pr. 13, Moscow, 119992 Russia*

[2] *Korean Astronomical Observatory, Taejon 305-348, Korea*

[3] *Special Astrophysical Observatory, Russian Academy of Sciences, Nizhnii Arkhyz, 357147 Karachai-Cherkessian Republic, Russia*

Received January 8, 2003

Abstract—Multicolor $BVRI$ surface photometry of the low-luminosity ($M_V \approx -18^m$) spiral galaxy NGC 4136 is presented. The photometric parameters of its components and the color distribution over the galactic disk are estimated. The color indices and the corresponding effective ages are determined for the brightest star-forming regions. The disk-to-dark halo mass ratio is derived from the measured rotation curve of the galaxy. The disk mass dominates within the optical boundaries of the galaxy, so its disk can be considered as a self-gravitating system. © *2003 MAIK "Nauka/Interperiodica"*.

Key words: *low-luminosity spiral galaxies, multicolor photometry.*

1. GENERAL INFORMATION

The goal of our study is to perform detailed multicolor surface photometry of the spiral galaxy NGC 4136 and its brightest star-forming regions.

NGC 4136 is a nearby SBc spiral galaxy observed almost face-on. The most important parameters of the galaxy adopted here are listed in Table 1. Figure 1 reproduces our V-band CCD image of the galaxy. Its distance is highly uncertain: the line-of-sight velocity relative to the Local Group is less than 600 km s^{-1} and the distance is 7.6 Mpc for the Hubble constant $H_0 = 75$ km s^{-1} Mpc^{-1}.[1] The galaxy has a bar and a ring, as well as a well-developed spiral structure in its outer disk (Fig. 1). The galaxy luminosity is unusually low: for the assumed distance, the absolute magnitude is $M_V \approx -18^m$.

Surface photometry of NGC 4136 was published in several reviews: in the B, V (Gavazzi *et al.* 1994), r (Grosbol 1985), R and J (Conselice 1997) bands. However, no detailed photometric studies of the galaxy have been carried out previously.

Measurements show that the brightness of the galactic disk exponentially decreases with distance r from its center with a radial scale length of $25.6''$ (Grosbol 1985; Baggett *et al.* 1998), while the decrease in bulge brightness follows de Vaucouleurs' law with an effective radius of $76.2''$ (Baggett *et al.* 1998). However, the bulge contribution to the total galaxy luminosity is extremely small (less than 1%) (Grosbol 1985). According to the classification scheme for the central regions of galaxies by van den Bergh (1995), a diffuse nucleus is located at the center of NGC 4136. Conselice (1997) pointed out that the brightness of the outer regions in NGC 4136 are azimuthally asymmetric. A short, thick bar with an axial ratio of $b/a = 0.7$ (Martin 1995; Chapelon *et al.* 1999) that stretches to the ring of NGC 4136 is observed (Fig. 1).

An H I study of the galaxy (Allsopp 1979) showed a marked difference between the radial velocities of

Table 1. Basic Parameters of NGC 4136

Parameters	Values
Type	SBc
m_B, mag.	11.83
$M_B^{0,i}$, mag.	−18.41
$V_{\rm LG}$, km s^{-1}	568
R, Mpc ($H_0 = 75$ km s^{-1} Mpc^{-1}	7.6
D_{25}, arcmin	3.93
i, deg	22.4
P.A., deg	72

*E-mail: gusev@sai.msu.ru

**E-mail: zasov@sai.msu.ru

***E-mail: kaj@rebus.sao.ru

[1] Given that the velocity field is anisotropic in the vicinity of the Local Group, the distance to NGC 4136 is 8 Mpc with a probable error of ±1–2 Mpc (D.I. Makarov, private communication).

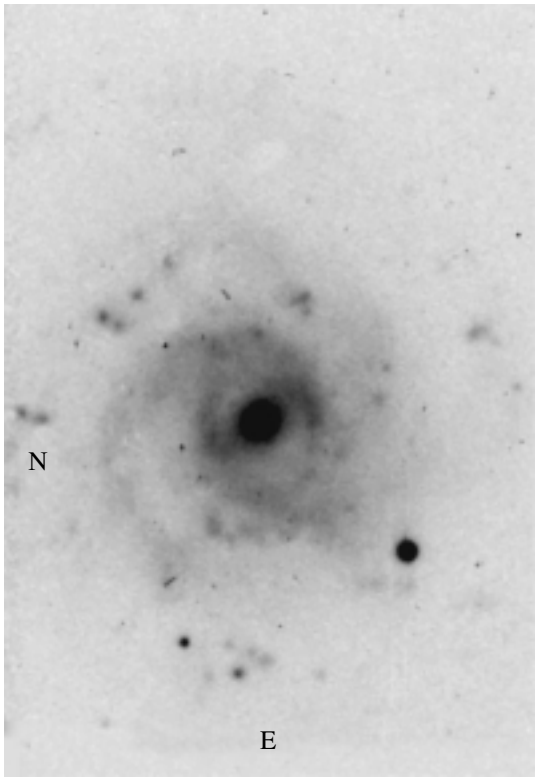

Fig. 1. A V-band CCD image of NGC 4136. The size is $2.5' \times 4.0'$.

NGC 4136 determined from optical and 21-cm observations (445 ± 50 and 596 ± 13 km s^{-1}, respectively). The H I mass in the galaxy recalculated to the assumed distance of 7.6 Mpc is $M(\mathrm{H\,I}) = 4.8 \times 10^8 M_\odot$, while the total mass of NGC 4136 within 3.3′ of its center is $9.6 \times 10^9 M_\odot$ (Allsopp 1979). The mass-to-light ratio of the galaxy is reported to be low, $(M/L)_{\mathrm{total}} = 4.6 \pm 1.5 (M/L)_\odot$. However, this quantity is uncertain, because the inclination of NGC 4136 to the line-of-sight is small (Allsopp 1979).

The H_2 mass in the galaxy is lower than the H I mass: $M(\mathrm{H_2}) = 3.3 \times 10^8 M_\odot$ (Sage 1993).

The disk-to-dark halo mass ratio for the galaxy has not been estimated previously.

Basic information on the galaxy is presented in Table 1, where all of the data were taken from the RC3 (de Vaucouleurs *et al.* 1991) and LEDA catalogs, except for the position angle of NGC 4136. The value determined by Fridman *et al.* (2003) from kinematic and photometric data is given for the latter.

2. OBSERVATIONS AND DATA REDUCTION

NGC 4136 was observed on January 22/23, 1998, with a regular CCD photometer (Zin'kovskiĭ *et al.* 1994) attached to a 1-m Zeiss-1000 telescope at the Special Astrophysical Observatory (with a focal length of 13.3 m). A K585 CCD camera used in combination with broadband B, V, R, and I filters reproduced a photometric system similar to the standard Johnson–Cousins $BVRI$ system. The CCD array size is 530×580 pixels, which provides a $143'' \times 212''$ field of view for an image scale of $0.28'' \times 0.37''$ per pixel.

Three exposures were taken in each photometric band; the telescope was slightly displaced by several arcseconds between these exposures to reduce the effect of CCD defects. The duration of each exposure in all bands was 600 s. The seeing was $2.0''$–$3.0''$.

Standard stars from the list of Majewski *et al.* (1994) (PG0220, PG1407, RU149, and S101429), whose images were obtained on the same observing night, were used for photometric calibration. We also used the aperture photometry of galaxies taken from the catalog of Prugniel and Heraudeau (1998).

The primary image processing was performed at the Special Astrophysical Observatory. A dark frame, which is a mean of several exposures taken with the same integration time as the object when the shutter was closed, was subtracted from the integrated images of the object and the standard stars to allow for the electronic zero shift and for the effect of hot pixels. The integrated twilight-sky images taken in each band with a signal-to-noise ratio of at least 60–80 were used as a flat field. All images were divided by the flat field to allow for a nonuniform detector pixel sensitivity.

The subsequent processing was performed at the Sternberg Astronomical Institute on the basis of a standard procedure using the ESO–MIDAS image processing systems. The main processing stages included the following:

(a) an image reduction to the same scale ($0.37''$ per pixel) and galaxy image matching (to within 0.1 pixel); due to the image displacement relative to one another, we managed to effectively remove cosmic-ray particle hits and the effects of individual hot pixels and bad CCD columns;

(b) the sky-background determination and subtraction from each image;

(c) the addition of galaxy images taken in the same bands;

(d) and allowance for the air mass;

(e) the transformation of counts to a logarithmic scale (magnitudes per square arcsec) based on photometric calibration;

(f) a correction for the difference between the instrumental photometric system and the standard Johnson–Cousins system (an allowance for the color equations derived from standard stars);

(g) the comparison of galaxy images taken in different bands and a mapping of the color distribution.

The photometric calibration accuracy was 0.04^m in B, V, and I and 0.06^m in R.

We corrected all of our data (brightnesses and color indices) for galactic extinction (using the catalog of de Vaucouleurs *et al.* 1991). In constructing the two-color diagrams, we formally applied a correction for the disk inclination to the color excesses, although it is small ($\approx 0.01^m$) in our case. The color excesses for $B-V$, $V-R$, and $R-I$ are 0.06^m, 0.03^m, and 0.04^m, respectively. Below, the corrected quantities are denoted by the indices 0, i.

The image scale for the assumed distance to the galaxy is 13.6 pc per pixel.

3. ANALYSIS OF THE PHOTOMETRIC MEASUREMENTS

3.1. Photometric Profiles and Morphology of the Galaxy

A bright region (the central part of a bulge or a circumnuclear disk) can be distinguished at the galactic center (Figs. 2a–2c). The maximum surface brightness within several pixels at the galactic center (in the region $12'' = 0.45$ kpc in diameter) is $m_V = 18.7^m$ arcsec^{-2}. Outside the circumnuclear region, the bulge has a low luminosity and cannot be traced by the photometric profiles. A short, bright bar with a flat photometric profile can be distinguished in the inner galaxy (Fig. 2b). The length of the semimajor axis of the bar is 0.55 kpc ($15''$) and its mean surface brightness is $m_V = 20.75 \pm 0.05^m$ arcsec^{-2}. The bar position angle is $22^\circ \pm 2^\circ$; i.e., the bar is almost perpendicular to the major axis of the galaxy (Figs. 2c and 3b). The isophotal ellipticity of the bar is $e = 0.18 \pm 0.04$; this parameter suggests that the bar belongs to the category of weak bars.

Two bright, short symmetric arms and two long, tightly wound spiral arms emerge from the bar ends, with the short and long spiral arms being wound in opposite directions (Figs. 1 and 2c). The oppositely wound arms intersect to form a ring 2.4 kpc ($65''$) in diameter. The ring position angle (P.A. $= 120^\circ \pm 10^\circ$) slightly increases with passband wavelength but remains close to the position angle of the galaxy as a whole (Fig. 3b). The isophotal ellipticity of the ring reaches its maximum at the distance $r = 25''$ from the center, being 0.21 ± 0.01 in B, V, and R and 0.33 ± 0.01 in I (Fig. 3a). The azimuthally averaged disk surface brightness of NGC 4136 within the ring decreases only slightly with distance, being, on average, 21.3 ± 0.1^m arcsec^{-2} in V (Figs. 2a and 2c).

Table 2. Parameters of the disk and bulge in NGC 4136 (in the V band)

Parameters	Disk	Inner disk	Bulge
r, arcsec	20–80	20–46	2–6
$\mu_V(0)$	20.39 ± 2.66	20.29 ± 0.39	17.67
$\mu_V(r_e)$	–	–	25.99 ± 0.92
r_0, kpc	1.08 ± 0.28	1.02 ± 0.02	–
r_0, arcsec	29.34 ± 7.63	27.87 ± 0.71	–
r_e, kpc	–	–	0.58 ± 0.11
r_e, arcsec	–	–	15.73 ± 2.99

Several bright and many faint diffuse regions (H II regions) are observed in the outer disk in the galactic spiral arms; their color indices are considered in Subsect. 3.4. The two bright starlike objects east of NGC 4136, one object in the northeast (see the lower part of Fig. 1) and the other, brightest object in the southeast, turned out to be the stars of our Galaxy projected onto NGC 4136. The starlike object east of NGC 4136 belongs to the galaxy itself (see Subsect. 3.4).

A large difference between the galaxy position angles in I and in B, V, R is observed in Fig. 3b at $r = 40''$. This difference results from the influence of radiation from the spiral arms of NGC 4136 at this galactocentric distance. In the I band, the outer parts of the spiral arms are visually unseen and give no contribution when plotting P.A. against distance. Nevertheless, the position angle of the major axis cannot be accurately determined without invoking additional data on the galaxy. The position angles of the major axis estimated for the galactic region under consideration (outside the bar) from the orientation of the major axes of isophotes fitted with ellipses lie within the range 90°–140°, which differs from the estimate (72°) obtained by Fridman *et al.* (2003) from averaging up to large galactocentric distances. The small disk inclination prevents an accurate estimation of P.A. For definiteness, the photometric profiles in Figs. 2a, 4, and 5a are shown for P.A. $= 135^\circ$.

The isophotes on the periphery of NGC 4136 are nearly circular. Their ellipticity reaches a minimum of 0.05 ± 0.01 at $r = 40''$ (Fig. 3a). The sharp increase in isophotal ellipticity at $r = 50''$ is an artifact associated with the influence of a bright field star and bears no relation to NGC 4136. The isophotal ellipticities obtained for the I-band galaxy images at $r > 25''$ are 0.1 larger than those for the B, V, and R bands. This is attributable to the locations of the

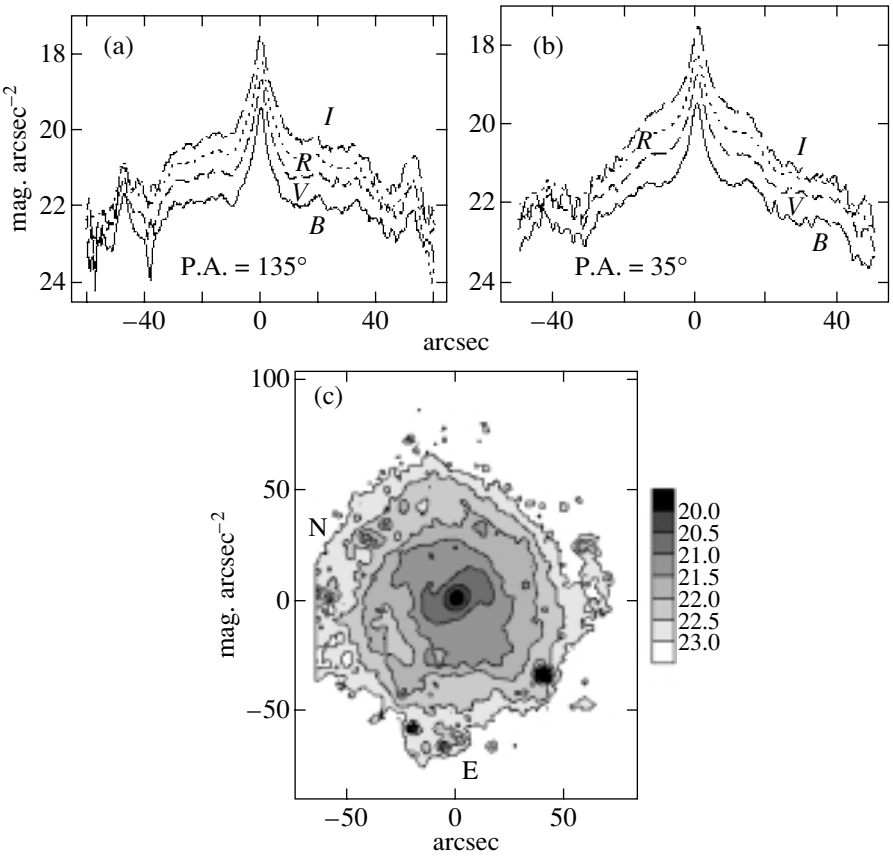

Fig. 2. Photometric profiles (in mag. arcsec^{-2}): (a) along the major axis of NGC 4136 and (b) along the major axis of the galactic bar in B (solid lines), V (short dashes), R (dots), and I (long dashes), and (c) a V-band image of the galaxy.

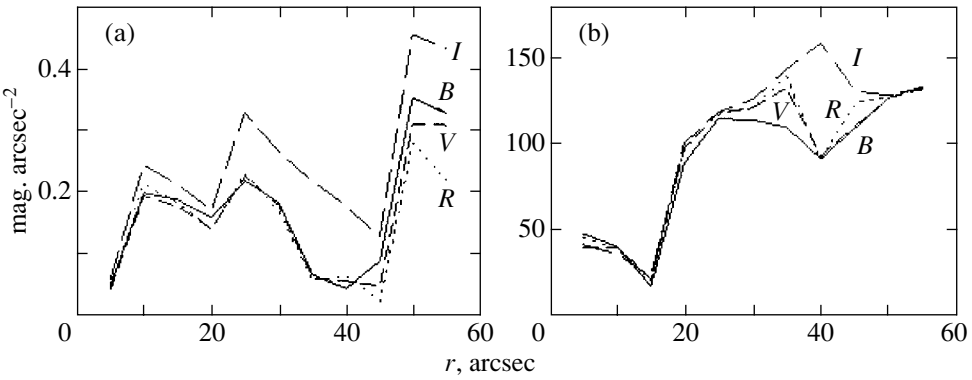

Fig. 3. (a) Isophotal ellipticity $e = 1 - b/a$ and (b) position angle of NGC 4136 versus the distance r from the galactic center in B, V, R, and I.

spiral arms in NGC 4136, which stretch it in width in shorter-wavelength bands. In general, the galactic disk inclination determined from the isophotal ellipticity at $r \approx 1'$ is $i = 35° \pm 3°$. This value is slightly larger than the value presented in the LEDA ($i = 22°$) or RC3 (de Vaucouleurs *et al.* 1991) catalogs (according to RC3, the logarithm of the galaxy axial ratio is $\log a/b = 0.03 \pm 0.03$, which corresponds to $i = 0°$–$30°$) and the value of $i = 18°^{+5°}_{-10°}$ from Fridman *et al.* (2003).

Figure 4 shows the averaged photometric profiles constructed for the derived P.A. and b/a. The local increase in surface brightness at $r = 54''$ can be explained by the influence of a field star. Analysis of the photometric profiles indicates that the disk brightness of NGC 4136 within $r = 20''$–$46''$ de-

creases exponentially with a scale length of 1.02 ± 0.03 kpc ($27.9'' \pm 0.7''$) in the V band and a central surface brightness $\mu_V(0) = 20.29 \pm 0.39^m$ arcsec^{-2}. The profile decomposition into a disk with an exponential brightness decrease and a bulge shows that the decrease in brightness at $r = 2''$–$6''$ follows de Vaucoulers' law. The galactic bulge has the following parameters in the V band: an effective radius $r_e = 0.58 \pm 0.11$ kpc ($15.3'' \pm 3.0''$) and $\mu_V(r_e) = 26.0 \pm 0.9^m$ arcsec^{-2}. These data confirm the conclusion of van den Bergh (1995) about the presence of a compact bulge (nucleus) in NGC 4136, in contrast to the conclusion of Baggett *et al.* (1998) about the presence of an extended bulge in this galaxy.

The total V luminosity of the galactic bulge is $L_V^{\rm bulge} = (0.006 \pm 0.002) L_V^{\rm disk}$.

The decrease of the disk brightness in I is appreciably larger than that in bluer bands (Fig. 4). This is probably because the relative number of young, hot stars increases to the periphery of the galaxy. Unfortunately, because of the high sky background level in I and, as a result, the low signal-to-noise ratio, we could not study the parameters of the outer disk in NGC 4136 in this band.

The integrated bulge and disk parameters are given in Table 2.

3.2. The Color Distribution in the Disk of NGC 4136

The total color index of NGC 4136 is $B - V = 0.6^m$ (de Vaucouleurs *et al.* 1991), which is typical of late-type galaxies. Note, however, that our measurements refer only to the inner galactic region with a diameter that is approximately half D_{25}.

The galactic nucleus is moderately red; its color indices are $B - V = 0.76^m \pm 0.03^m$, $V - R = 0.52^m \pm 0.03^m$, and $R - I = 0.73^m \pm 0.08^m$ (Figs. 5a–5e), with the central region of the galaxy within $2''$ of its center being bluer than its surroundings by 0.05^m in $B - V$ and $V - R$. The galaxy blues to $B - V = 0.55^m \pm 0.10^m$, $V - R = 0.3^m \pm 0.1^m$, and $R - I = 0.35^m \pm 0.05^m$ with increasing distance from its center (Figs. 5a, 5c–5e), which reflects an increase in the relative number of young stars in the outer galaxy.

The bar of NGC 4136 also becomes bluer toward the periphery. Despite the small length of the bar, its color indices appreciably decrease with increasing galactocentric distance from $0.76^m \pm 0.01^m$ to $0.65^m \pm 0.01^m$ in $B - V$, from $0.58^m \pm 0.01^m$ to $0.40^m \pm 0.02^m$ in $V - R$, and from $0.65^m \pm 0.01^m$ to $0.49^m \pm 0.02^m$ in $R - I$ (Fig. 5b). Such an enhancement of the star-formation rate on the bar periphery is a frequent occurrence (Gusev 2000).

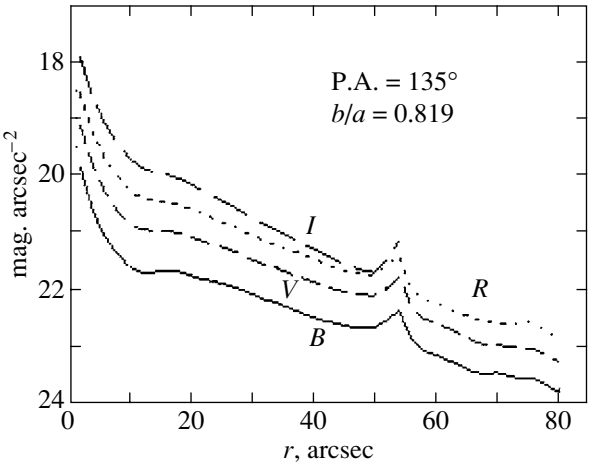

Fig. 4. Averaged B, V, R, and I photometric profiles of NGC 4136 (in mag. arcsec^{-2}).

The color of the inner disk in NGC 4136 within the ring changes only slightly with distance from its center. The color indices in this region are, on average, $0.65^m \pm 0.05^m$ in $B - V$, $0.38^m \pm 0.03^m$ in $V - R$, and $0.50^m \pm 0.05^m$ in $R - I$ (Fig. 5a); beyond the ring, the disk becomes bluer (Figs. 5a, 5c–5e).

An astonishingly sharp decrease in $R - I$ is observed along the minor axis of NGC 4136 (Fig. 5b). As was noted in Subsect. 3.1, this decrease can be explained by the contribution from young stars in the spiral arms. Their radiation gives a small contribution in I and a larger contribution in R (apart from the stellar radiation, the Hα emission line of H II regions also falls within this band).

The bright diffuse regions in the spiral arms on the periphery of the galaxy, which are sites of star formation, are bluest in NGC 4136. For them, $R - I = 0.0^m$, which corresponds to an extremely young stellar population (for more details, see Subsect. 3.4).

3.3. Two-Color Diagrams

Figures 6a–6d show two-color $(B - V)_0^i$–$(V - R)_0^i$ and $(B - V)_0^i$–$(V - I)_0^i$ diagrams for various regions of NGC 4136. The numbers in Figs. 6a and 6c denote the following galactic regions: *1*, the nucleus color of NGC 4136 within $2.7''$ of its center; *2*, the bulge color within the range $3''$ to $5.5''$ from its center; *3*, the color of the spiral arms in NGC 4136; *4*, the color of the galactic disk; and *5*–*7*, the bar colors at galactocentric distances of 0.26, 0.40, and 0.51 kpc ($7''$, $11''$, and $14''$), respectively.

In general, the scatter of points in the two-color diagrams for various components of NGC 4136 is small (Figs 6a, 6c). The color indices suggest that there are no powerful starbursts. The galactic center,

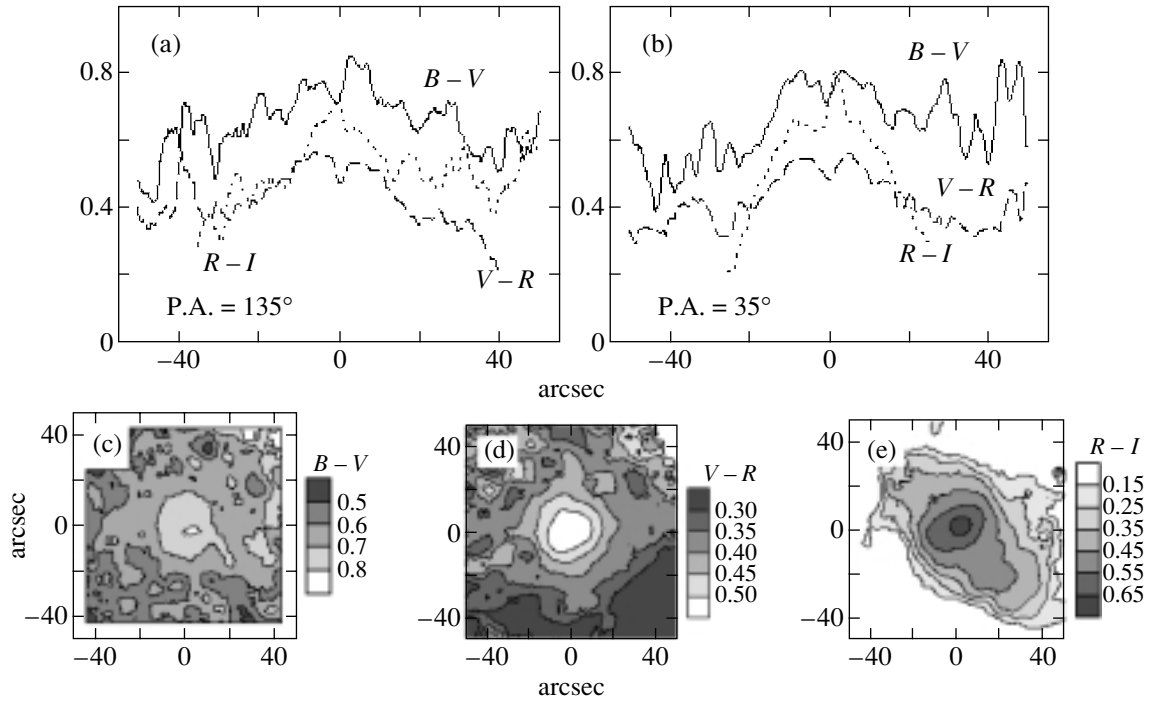

Fig. 5. The $B-V$ (solid lines), $V-R$ (dashed lines), and $R-I$ (dots) color indices (a) along the major axis of NGC 4136 and (b) along the major axis of the galactic bar and (c) $B-V$, (d) $V-R$, and (e) $R-I$ color maps of the galaxy.

the circumnuclear region, and the inner bar (points *1*, *2*, and *5*, respectively) have almost the same colors and are located in the two-color diagrams near the normal color sequence (NCS) for galaxies in the region occupied by stellar systems with predominantly old stellar populations and moderate color excesses related to intrinsic extinction. The outer bar and the spiral arms of NGC 4136 (points *6*, *7*, and *3*, respectively) have a normal stellar population for galaxies, with the fraction of young stars increasing to the periphery of the galaxy. Curiously, the disk of NGC 4136 between the main spiral arms proved to be no less bluer in $V-R$ and $V-I$ than the galactic spiral arms. Star-forming regions in this galaxy are scattered over the entire disk, being encountered both in and between the spiral arms.

Thus, NGC 4136 is a nearby low-luminosity spiral galaxy with a moderate star-formation rate in which blue stars in the inner disk weakly concentrate toward the spiral arms and the contribution of young stars toward the total radiation increases toward the periphery.

3.4. Sites of Star Formation in the Galaxy

We distinguished the eleven brightest small blue regions, which are sites of star formation, in the spiral arms of NGC 4136. Figures 6b and 6d show their positions in the two-color $(B-V)^i_0$–$(V-R)^i_0$ and $(B-V)^i_0$–$(V-I)^i_0$ diagrams. To estimate the color indices of these blue regions, we determined their brightness in each band by subtracting the brightness of the adjacent disk regions. The positions of the sites of star formation in the two-color diagrams allow their ages to be estimated by using the evolutionary tracks of aging stellar systems for $Z = 0.008$, 0.02, and 0.05 obtained by means of the PEGASE2 program (Fioc and Rocca-Volmerange 1997). The differences between the assumed metallicities Z give a scatter that we took into account when estimating the errors in the ages. The age-estimation procedure was described in more detail by Gusev (2002). Table 3 gives the derived parameters of the objects: the coordinates from the galactic center in arcsecs (column 2); the $(B-V)^i_0$, $(V-R)^i_0$, and $(V-I)^i_0$ color indices (columns 3–5); the diameters of the regions in parsecs (column 6); and the effective ages (column 7).

The sizes of the sites of star formation in NGC 4136 under consideration lie within the range from 100 to 170 pc. There are no large young stellar complexes in the galaxy. The sizes of the observed star-forming regions are in good agreement with those of large stellar associations (according to the hierarchical star formation scale of Efremov (1989)).

Seven of the star-forming regions under consideration (*2–5*, *7–9*) are located at deprojected distances of 1.6–1.9 kpc from the galactic center,

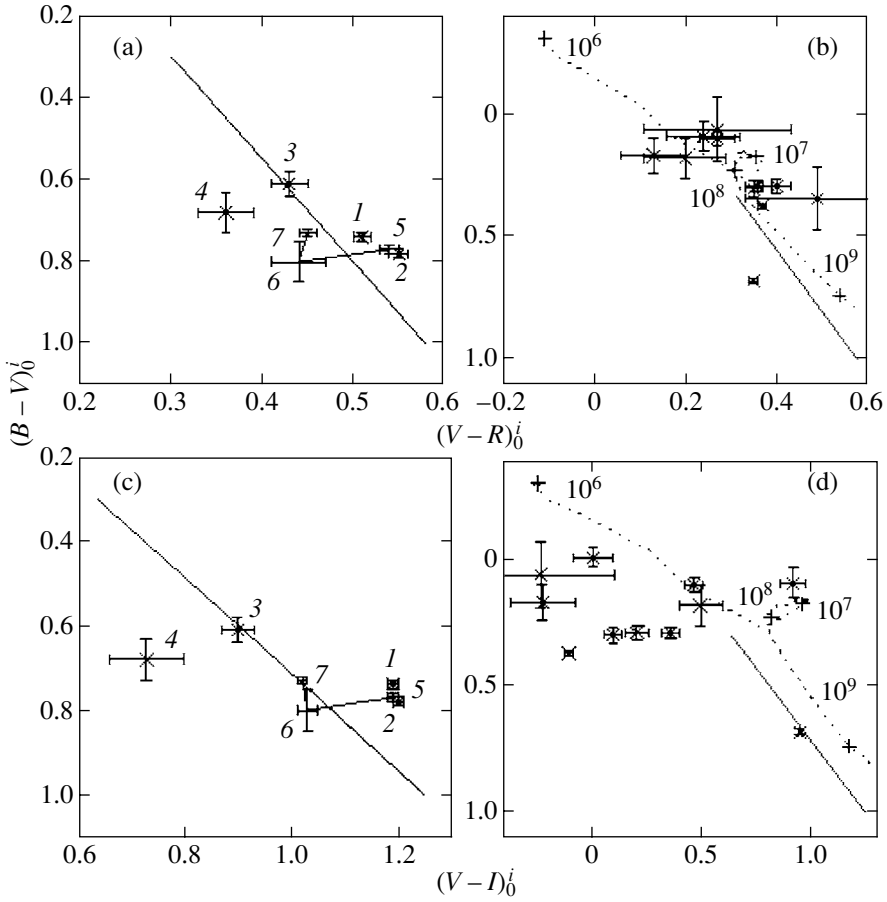

Fig. 6. Two-color $(B-V)_0$–$(V-R)_0$ (a, b) and $(B-V)_0$–$(V-I)_0$ (c, d) diagrams for NGC 4136 (a, c) and sites of star formation in the galaxy (b, d). The straight lines represent the normal color sequences (NCS) for galaxies (Buta and Williams 1995). The broken solid lines in Figs. 6a and 6c indicate the color variations along the major axis of the bar in NGC 4136. The dotted lines in Figs. 6b and 6d represent the evolutionary tracks of the stellar system without star formation (the system age in years is shown). The measurement errors are shown. For the remaining notation, see the text.

at the outer ring boundary of NGC 4136. According to Elmegreen (1994), favorable conditions for the formation of young stellar complexes in late-type galaxies are produced in the inner Lindblad resonance (ILR) region. On the other hand, the short bars in late-type galaxies can stretch to distances that are limited by the ILR radius (B. Elmegreen and D. Elmegreen 1985). Thus, based on the bar and ring sizes, we can assume that the ILR radius in NGC 4136 is 1.7 ± 0.15 kpc.

The ages of most of the star-forming regions in NGC 4136 under consideration do not exceed 10^7 yr (Table 3), although the age of one of the regions under study (6) can reach 3.5×10^8 yr.

3.5. The Mass Distribution in the Galaxy

The rotation curve of the galaxy was first measured by Allsopp (1979) in the H I line. This author found the rotational velocity to slowly increase up to approximately $30\sin^{-1}i$ at $200''$. However, the derived shape of the rotation curve cannot be considered to be reliably determined, because the beam size of the radio telescope was larger than the galaxy size. Fridman *et al.* (2003) has recently obtained an optical rotation curve of the galaxy from Hα observations with a Fabry–Perot interferometer. The shape of the $V(r)$ curve for the inner galactic region $r < 70''$, where it was determined most reliably, is shown in Fig. 7 for the assumed $i = 18°$ (from Fridman *et al.* 2003). Below, however, we show that this value of i is probably underestimated. The isolated point at $r \approx 7.6$ kpc corresponds to the maximum rotational velocity of the galaxy: approximately 100 km s^{-1} at $r = 206''$, as measured by Allsopp (1979).

However, the uncertainty in i is still large and can lead to an error in the estimated rotational velocity by a factor of the order of 2. The decrease in velocity at $r \approx 40''$ cannot be explained for any of the acceptable mass distributions and, clearly, this feature in the rotation curve is associated with local noncircular

Table 3. Parameters of the sites of star formation

№	Coordinates, arcsec	$(B-V)_0^i$	$(V-R)_0^i$	$(V-I)_0^i$	d, pc	$\tau, 10^6$ yr
1	2	3	4	5	6	7
1	58.8 N, 0.6 W	0.30	0.35	0.10	140	2.7 ± 1.3
2	42.3 N, 28.0 W	0.29	0.40	0.21	120	4.0 ± 1.6
3	38.3 N, 25.8 W	0.17	0.13	−0.22	175	4.4 ± 2.6
4	32.8 N, 33.9 W	0.29	0.36	0.36	115	5.2 ± 0.4
5	24.3 N, 43.1 W	−0.01	–	0.01	100	4.6 ± 0.8
6	0.5 N, 23.6 W	0.34	0.49	–	160	<350
7	11.2 S, 33.2 W	0.10	0.27	0.47	150	6.4 ± 0.8
8	31.4 S, 6.4 W	0.18	0.20	0.50	120	6.4 ± 1.0
9	12.6 N, 28.0 E	0.09	0.24	0.92	145	16 ± 10
10	24.7 N, 39.0 E	0.06	0.27	−0.23	95	3.4 ± 2.1
11	5.6 N, 67.2 E	0.37	0.37	−0.10	110	2.7 ± 0.8

gas motions (note that the brightest H II regions are observed at this distance).

The thin lines in Fig. 7 indicate the contribution from the galactic disk with the photometrically determined radial scale length and the dark halo. The bulge mass is too low to be reliably estimated from available data. The absence of a massive bulge and the fixing of a radial disk scale length, to a large extent, alleviate the problem of the nonuniqueness of the solution when separating the rotation curve into components.

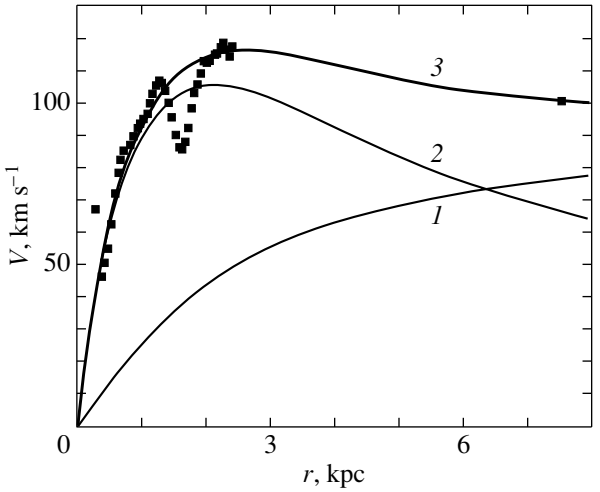

Fig. 7. The rotation curve of NGC 4136 (squares), as constructed by Fridman (2003). The isolated point is the rotational velocity, as derived by Allsopp (1979). Lines *1* and *2* represent the components of the rotation curves associated with the disk and the halo, respectively, and line *3* represents a model rotation curve of the galaxy.

As we see from the model rotation curves, the disk is self-gravitating almost over its entire length: the dark-halo mass begins to dominate only on the far periphery of the galaxy (the optical disk is traceable up to approximately 4 kpc). Within four radial scale lengths, the disk mass is almost twice the halo mass, while for spiral galaxies the halo mass within this radius generally dominates (Bottema 1993; Khoperskov *et al.* 2001). The total disk mass M_d is $6.7 \times 10^9\ M_\odot$. For the assumed disk luminosity (see above), the total mass-to-light ratio for the disk is $M_\mathrm{d}/L_\mathrm{d} \approx 4$. The derived value is at least twice as high as the value that follows from evolutionary models of stellar systems with the color indices observed for NGC 4136 ($B-R = 0.8^m$–1.2^m) and a Salpeter initial mass function (IMF) (see Fig. 2 in Bell and de Jong (2001)). This indicates that either the contribution from low-mass stars to the total disk mass was underestimated in comparison with the Salpeter IMF or, what is much more likely, the mass of all of the galactic components was overestimated because of the underestimated angle i. If we assume that $i = 35°$, which corresponds to the isophotal flattening in the inner galaxy, then the mass and, accordingly, the $M_\mathrm{d}/L_\mathrm{d}$ ratio will decrease by a factor of 2.2. However, this uncertainty does not affect the estimated component mass ratio and the conclusion that the observed spiral structure of the galaxy is located in the region where the disk mass dominates. A low-mass galaxy may preserve its ordered spiral pattern precisely because its disk is self-gravitating.

4. CONCLUSIONS

We have performed detailed photometry of the galaxy NGC 4136 up to a distance of $\sim 1'$ from its center, within which an ordered galactic structure is located (a bulge, a bar, a ring, and spiral arms). Although the galaxy orientation does not allow the disk position angle and inclination to be reliably estimated, it is favorable for investigating the brightness and color distributions over the disk of NGC 4136. We also estimated the photometric parameters and total luminosity of the galactic bulge and disk. The galaxy (including its bar) becomes bluer with increasing distance from its center, but its spiral arms differ in color from the interarm segments only slightly. We estimated the color indices and ages of the brightest star-forming regions. The ages of most of them do not exceed 10^7 yr. Analysis of the available rotation curve indicates that, within the optical boundaries of the galaxy, the disk dominates in mass over the spherical components, which makes NGC 4136 atypical of the low-luminosity galaxies characterized by a large contribution from the dark halo to the total mass (see, e.g., Persic and Salucci 1996).

ACKNOWLEDGMENTS

We wish to thank D.V. Bizyaev (Sternberg Astronomical Institute) for help with the data reduction. We are grateful to O.K. Sil'chenko (Sternberg Astronomical Institute) for several valuable remarks. This study was supported by the Russian Foundation for Basic Research, project nos. 01-02-16800 and 01-02-17597.

REFERENCES

1. N. J. Allsopp, Mon. Not. R. Astron. Soc. **188**, 371 (1979).
2. W. E. Baggett, S. M. Baggett, and K. S. J. Anderson, Astron. J. **116**, 1626 (1998).
3. E. F. Bell and R. S. de Jong, Astrophys. J. **550**, 212 (2001).
4. S. van den Bergh, Astron. J. **110**, 613 (1995).
5. R. Bottema, Astron. Astrophys. **275**, 16 (1993).
6. R. Buta and K. L. Williams, Astron. J. **109**, 543 (1995).
7. S. Chapelon, T. Contini, and E. Davoust, Astron. Astrophys. **345**, 81 (1999).
8. C. J. Conselice, Publ. Astron. Soc. Pac. **109**, 1251 (1997).
9. Yu. N. Efremov, *Sites of Star Formation in Galaxies* (Nauka, Moscow, 1989).
10. B. G. Elmegreen, Astrophys. J. Lett. **425**, L73 (1994).
11. B. G. Elmegreen and D. M. Elmegreen, Astrophys. J. **288**, 438 (1985).
12. M. Fioc and B. Rocca-Volmerange, Astron. Astrophys. **326**, 950 (1997).
13. A. M. Fridman, L. V. Afanasiev, S. N. Dodonov, *et al.*, Astron. Astrophys. (2003) (in press).
14. G. Gavazzi, B. Garilli, A. Boselli, and I. Cruz-González, Astron. Astrophys. Suppl. Ser. **104**, 271 (1994).
15. P. J. Grosbol, Astron. Astrophys. Suppl. Ser. **60**, 261 (1985).
16. A. S. Gusev, Astron. Zh. **77**, 654 (2000) [Astron. Rep. **44**, 579 (2000)].
17. A. S. Gusev, IAU Symp. **207**, 450 (2002).
18. A. V. Khoperskov, A. V. Zasov, and N. V. Tyurina, Astron. Zh. **78**, 213 (2001) [Astron. Rep. **45**, 180 (2001)].
19. S. R. Majewski, R. G. Kron, D. C. Koo, and M. A. Bershady, Publ. Astron. Soc. Pac. **106**, 1258 (1994).
20. P. Martin, Astron. J. **109**, 2428 (1995).
21. M. Persic and P. Salucci, Mon. Not. R. Astron. Soc. **281**, 27 (1996).
22. P. Prugniel and P. Heraudeau, Astron. Astrophys. Suppl. Ser. **128**, 299 (1998).
23. L. J. Sage, Astron. Astrophys. Suppl. Ser. **100**, 537 (1993).
24. G. de Vaucouleurs, A. de Vaucouleurs, H. G. Corwin, *et al.*, *Third Reference Catalogue of Bright Galaxies* (Springer-Verlag, New York, 1991).
25. I. I. Zhin'kovskiĭ, S. S. Kaĭsin, A. I. Kopylov *et al.*, Tekh. Otchet Spets. Astrofiz. Obs. Ross. Akad. Sci. **231** (1994).

Translated by V. Astakhov

Astronomy Letters, Vol. 29, No. 6, 2003, pp. 372–373. Translated from Pis'ma v Astronomicheskiĭ Zhurnal, Vol. 29, No. 6, 2003, pp. 424–425.

The Universal Luminosity Function of Binary X-ray Sources in Galaxies

K. A. Postnov*

Sternberg Astronomical Institute, Universitetskii pr. 13, Moscow, 119992 Russia

Received January 8, 2003

Abstract—The empirically found universal power-law form of the X-ray luminosity function for a population of high-mass X-ray binaries in galaxies can be explained by the fundamental mass–luminosity and mass–radius relations for massive stars. © *2003 MAIK "Nauka/Interperiodica".*

Key words: *X-ray and gamma-ray sources.*

The unique capabilities of the modern Chandra and XMM-Newton spaceborne X-ray observatories allow us to observe point sources in nearby galaxies and thereby study the formation and evolution of close binary systems. Recently, Grimm *et al.* (2002, 2003) have found that the differential luminosity function of point X-ray sources in a wide luminosity range ($L_x \sim 10^{34}$–10^{40} erg s^{-1}) has a universal power-law form:

$$\frac{dN}{dL_x} \propto \mathrm{SFR} \times L_x^{-\alpha},$$

where SFR is the star-formation rate in a specific galaxy and $\alpha = 1.61 \pm 0.12$.

Let us show that the empirically found luminosity function is naturally determined by the pattern of mass accretion onto the compact object in a close binary system. In high-mass X-ray binaries, accretion onto the compact object proceeds from the stellar wind of the optical component—an early-type star. In such stars, the radiation pressure plays a crucial role in plasma acceleration. Therefore, the stellar-wind outflow rate is

$$\dot{M}_\mathrm{w} \propto \frac{L_\mathrm{o}}{v_\infty}, \qquad (1)$$

where L_o is the luminosity of the star and v_∞ is the stellar-wind velocity at infinity. With a high accuracy, the latter is proportional to the parabolic velocity v_p near the stellar photosphere, $v_\infty \approx 3v_\mathrm{p}$. Formula (1) qualitatively agrees with the results of observations (De Jager 1980).

It is well known that for stationary main-sequence stars, there are power-law mass–luminosity (M–L) and mass–radius (M–R) relations (see, e.g., Schwarzschild 1958). For massive stars, the M–L relation is specified by the condition of outward diffuse heat transfer from the stellar interiors $L \propto 1/(\kappa\rho)\nabla T^4$ (ρ is the density and κ is the opacity) and by the virial relation $T \propto M/R$ for stationary stars. In such stars, the opacity is mainly determined by Thomson scattering and $L \propto M^3$ (Eddington 1926). The empirically found exponent for early-type stars is close to the theoretically expected value of 3 (De Jager 1980).

The M–R relation can be derived from the balance of the energy release per gram at the stellar center due to thermonuclear reactions $\epsilon \sim \rho T^n$ (ρ is the density at the stellar center) and from the condition of diffuse radiative transfer: $R \propto M^{(n-1)/(n+3)}$. For massive stars (the CNO cycle), $n \approx 10$–27, depending on the central temperature. The empirical mass–radius relation for main-sequence stars, $R \propto M^{0.8}$, in a wide mass range is in good agreement with these concepts. We will use it below.

The rate of mass accretion $\dot{M}_\mathrm{a}$ onto the compact star from the stellar wind is determined by its orbital velocity (v_orb), the binary component mass ratio (M_x and M_o for the compact and optical stars, respectively), and the stellar-wind velocity. In the case of a fast stellar wind ($v_\mathrm{w} > v_\mathrm{orb}$) for Bondi–Hoyle accretion, the following relation holds:

$$\dot{M}_\mathrm{a} \propto \dot{M}_\mathrm{w} \frac{M_x^2}{a^2 v_\mathrm{w}^4},$$

where a is the semimajor axis of the binary system. Substituting in formula (1) for the stellar-wind outflow rate and using the M–L and M–R relations, we obtain the X-ray luminosity in the case of accretion from the stellar wind:

$$L_x \sim \dot{M}_\mathrm{a} \sim \frac{L_\mathrm{o}}{a^2 v_\mathrm{w}^5} \sim \frac{M_\mathrm{o}^{2.5}}{a^2}.$$

The distribution of binary systems in semimajor axes is also known from observations to be flat,

*E-mail: pk@sai.msu.ru

$dN/d\log a = \text{const}$ (Masevich and Tutukov 1988) and, thus, does not depend on the mass of the optical star. Therefore, $M_o \sim L_x^{2/5}$, and $dM_o/dL_x \sim L_x^{-3/5}$.

For the X-ray luminosity distribution function of the sources accreting from the stellar wind,

$$\frac{dN}{dL_x} = \frac{dN}{dM_o}\frac{dM_o}{dL_x},$$

using the power-law mass function of main-sequence stars $dN/dM_o \sim M_o^{-\beta}$, we obtain a power-law dependence:

$$\frac{dN}{dL_x} \sim L_x^{(-2/5)\beta-3/5}. \quad (2)$$

For instance, we can obtain $dN/dL_x \sim L_x^{-1.54}$ for the Salpeter stellar mass function (with a slope $\beta = 2.35$) and $dN/dL_x \sim L_x^{-1.6}$ for the Miller–Scalo fit ($\beta = 2.5$) for stars with masses of the order of $10M_\odot$, which corresponds to the observed law. A high mass-loss rate by early-type stars naturally results in a steeper slope of the observed mass function than the initial distribution. This effect changes the exponent in formula (2) in the desired direction (makes α closer to the observed value).

In the case of a slow stellar wind $v_w < v_{orb}$, the mass accretion is determined mainly by the orbital velocity of the compact star. For high-mass binaries with $M_o/M_x \gg 1$, the latter is related to the mass of the optical star in the same way as the escape velocity from its surface, so the above qualitative result will not change.

Note that although the role of chemical composition is important for the absolute values of the luminosities and radii of main-sequence stars, as well as for the mass-loss rate, it does not affect the functional relations that define the form of the luminosity function used above.

Curiously, a relation similar to the derived law is also formally obtained in the case of accretion with the optical component filling its Roche lobe, because in this case the time scale of the mass loss by the optical star is, with a high accuracy, close to the thermal time scale and the mass transfer rate is $\dot{M}_o \sim M_o/\tau_{KH} \sim L_o/(M_o/R_o)$. However, in actual high-mass X-ray binaries, mass transfer on the thermal time scale leads to supercritical accretion. In this accretion regime, the X-ray luminosity of the source L_x is of the order of the Eddington luminosity and does not depend on the mass of the optical star and can be lower because of absorption in the strong wind outflowing from the accretion disk (SS 433 is an example of such a system). Such sources are few in number and cannot significantly affect the form of the X-ray luminosity function.

ACKNOWLEDGMENTS

I am grateful to R.A. Sunyaev and M.R. Gilfanov for discussions and L.R.Yungelson for remarks. This work was supported in part by the Russian Foundation for Basic Research (project nos. 00-02-17164 and 02-02-16500).

REFERENCES

1. S. A. Eddington, *The Internal Constitution of Stars* (Cambridge Univ. Press, Cambridge, 1926).
2. H.-J. Grimm, M. R. Gilfanov, and R. A. Sunyaev, Astron. Astrophys. **391**, 923 (2002).
3. H.-J. Grimm, M. R. Gilfanov, and R. A. Sunyaev, Mon. Not. R. Astron. Soc. (2003) (in press).
4. K. de Jager, *The Brightest Stars* (Reidel, Dordrecht, 1980; Mir, Moscow, 1984).
5. A. G. Masevich and A. V. Tutukov, *Stellar Evolution: Theory and Observations* (Nauka, Moscow, 1988).
6. M. Schwarzshield, *Structure and Evolution of Stars* (Princeton Univ. Press, Princeton, 1958).

Translated by G. Rudnitskii

Astronomy Letters, Vol. 29, No. 6, 2003, pp. 374–382. Translated from Pis'ma v Astronomicheskiĭ Zhurnal, Vol. 29, No. 6, 2003, pp. 426–435.

The Generation of a Large-Scale Galactic Magnetic Field by Electric Currents of Energetic Particles

A. Z. Dolginov and I. N. Toptygin*

St. Petersburg State Technical University, ul. Politekhnicheskaya 29, St. Petersburg, 195251 Russia

Received January 10, 2003

Abstract—We consider the generation of a magnetic field in the Galaxy by the electric currents excited by cosmic-ray particles in the disk and halo. We assume that the sources of relativistic particles are distributed continuously and uniformly in the Galactic disk, their total power is equal to the observed value, and the particles themselves undergo anisotropic diffusion in a homogeneous medium. We take into account the differential rotation of the Galactic disk but disregard the turbulence gyrotropy (the α effect). The strength of the generated magnetic field in our model is shown to strongly depend on the symmetry of the relativistic proton and thermal electron diffusion tensors, as well as on the relations between the tensor components. In particular, if the diffusion is isotropic, then no magnetic field is generated. For the independent tensor components estimated from observed parameters of the Galactic medium and with a simultaneous allowance made for the turbulent field dissipation processes, the mechanism under consideration can provide an observable magnetic-field strength of the order of several microgauss. This mechanism does not require any seed magnetic field, which leads us to suggest that relativistic particles can give an appreciable and, possibly, determining contribution to the formation of the global Galactic magnetic field. However, a final answer can be obtained only from a nonlinear self-consistent treatment, in which the symmetry and magnitude of the particle diffusion tensor components should be determined together with the calculation of the magnetic field. © *2003 MAIK "Nauka/Interperiodica"*.

Key words: *Galaxy, large-scale magnetic field, Galactic plasma.*

INTRODUCTION

The large set of observational data suggests that there are magnetic fields of various scales in galaxies, both regular fields with scales of the order of the stellar-system size and small-scale stochastic magnetic inhomogeneities. The informative review of Ruzmaikin *et al.* (1988) presents observational data on galactic magnetic fields and existing theories of their origin. Explaining the origin of the large-scale magnetic field has long involved the greatest difficulties and only in the last two or three decades has a dynamo theory been developed. This theory is currently purporting to consistently interpret the basic patterns.

However, the dynamo theory is still far from complete, and it leaves a number of fundamental questions unanswered. Some of these questions have been discussed recently (see, e.g., the review article of Beck *et al.* 1996). In particular, at present, the dynamo theory does not allow the calculation of the Galactic magnetic field to be brought to a number. A major problem is that the existing kinematic dynamo theories are linear, while nonlinear effects can restrict the growth of the large-scale magnetic field at a low level (Gruzinov and Diamond 1994, 1996). The difference between the growth rates of harmonics with different wave numbers by many orders of magnitude (Vainshtein and Rossener 1991; Kalsrud and Anderson 1992) makes the applicability of the commonly used approximation of zero correlation time problematic. The limited accuracy of the observations complicates a detailed comparison between the predictions of the existing theory and the observational data. This is particularly true for the poloidal Galactic field components, which are difficult to observe. Some facts are apparently difficult to explain in terms of the dynamo theory in the first place, for example, the existence of a noticeable large-scale magnetic field in irregular galaxies such as the Magellanic Clouds (Chi and Wolfendale 1993). No noticeable differential rotation needed for dynamo action is observed in them.

All of these circumstances make the investigation of other magnetic-field generation mechanisms in galaxies of current interest. Analysis of the role of the relativistic Galactic-plasma (cosmic-ray) component in producing the large-scale Galactic magnetic field seems highly promising, especially because the cosmic-ray composition and energy spectrum, as

*E-mail: cosmos@it10242.spb.edu

1063-7737/03/2906-0374$24.00

well as the power and distribution of the sources, have been extensively studied in preceding decades. Protons with an energy of $\sim$1 GeV constitute a major fraction of the relativistic particles in the Galaxy. Being accelerated in various objects (probably mainly by shock waves in supernova remnants and in strong stellar winds) located mostly in the disk, they diffuse to great distances up to the boundaries of the Galaxy and leave it in a time of $\sim(1\text{–}3)\times10^8$ yr. The total power of the relativistic particle sources in the Galaxy is estimated to be $Q_E\approx(1\text{–}3)\times10^{40}$ erg s^{-1} (Berezinskiĭ *et al.* 1990). With the mean particle energy being $\sim$1 GeV, the generation power of relativistic particles is $Q_0\approx10^{43}$ particles s^{-1}. Spreading over the Galaxy and interacting with the background plasma, the relativistic and background particles produce a net electric current, which can serve as a source of the large-scale magnetic field. Here, our goal is to calculate this field and to compare it with observational data.

In Section 1, we refine the initial model parameters and formulate the basic equations. The density of the electric current generated by energetic particle sources is calculated in Section 2. The current is produced mainly by relativistic protons and background electrons. In Section 3, we use published data to estimate the diffusion coefficients for relativistic and thermal particles and discuss the structure of the diffusion tensors. The magnetic field generated by energetic particles is calculated in Section 4. In Section 5, we take into account the differential rotation of the Galaxy, which enhances its toroidal field, and discuss our results. Our conclusions are formulated in the final section.

Note that the resonant generation of various plasma waves and their inherent magnetic fields with scales of the order of the Larmor radius of relativistic particles has previously been considered repeatedly by different authors (see, e.g., Völk and McKenzie 1982). As far as we know, the generation of the large-scale Galactic magnetic field by relativistic particles is studied here for the first time.

1. THE INITIAL MODEL AND BASIC EQUATIONS

It is well known (Berezinskii *et al.* 1990) that protons and helium nuclei constitute a major fraction of the relativistic charged particles in the Galaxy, while the fraction of electrons and heavy nuclei is probably close to 1%. Since the number of relativistic particles rapidly decreases with increasing energy (as $\mathcal{E}^{-2.7}$), it will suffice to consider a simple three-component Galactic plasma model to fundamentally elucidate the generation mechanism of the large-scale magnetic field. We take into account relativistic protons (with a mean kinetic energy $E=1$ GeV and density $N\sim10^{-9}$ cm^{-3}) and background particles—protons and electrons with densities $n_0\gg N$. We also take into account neutral hydrogen, which determines the magnetic viscosity in neutral clouds and at the warm phase of the interstellar medium.

Since the distribution of actual discrete relativistic particle sources in the Galaxy is known only approximately, we use a disk-averaged steady-state model distribution with a small number of parameters. We choose the total generation power Q_0 of relativistic particles, the half-thickness h of the distribution of sources in the disk, and its effective radius R as these parameters. The distribution of sources in the disk is assumed to be azimuthally symmetric.

It is convenient to write the density of the relativistic proton sources in Fourier representation as

$$Q_{\mathbf{k}}=\frac{\pi Q_0}{2h}e^{-k_\perp R}\int\limits_0^h\cos\left(\frac{\pi\zeta}{2h}\right)\cos k_\parallel\zeta\,d\zeta, \qquad (1)$$

where $(k_\perp,\phi,k_\parallel)$ are the cylindrical coordinates of the wave vector $\mathbf{k}$. In cylindrical coordinates (r,α,z), the distribution of sources (1) takes the form

$$Q(r,z)=\frac{Q_0}{8}\left(\frac{R}{h}\right)\frac{\Theta(h+z)\Theta(h-z)\cos(\pi z/2h)}{(r^2+R^2)^{3/2}}, \qquad (2)$$

where $\Theta(z)$ is the step function. The sources are located symmetrically in azimuth inside a disk of thickness $2h$ and are absent outside the disk; their density for $r\gg R$ decreases as r^{-3}. The actual decrease is probably more rapid, but this is of little importance when determining the magnetic field inside the Galactic disk. Here, we will not discuss the field distribution in the halo and outside the Galaxy. To compensate for the electric charge of the relativistic protons, we must specify the same source of nonrelativistic electrons:

$$Q_e(r,z)=Q_p(r,z)=Q(r,z). \qquad (3)$$

At distances of the order of the Galaxy size, relativistic and thermal particles undergo anisotropic diffusion attributable to the regular large-scale magnetic field, small-scale turbulent fields, collisions with charged and neutral particles, and random (turbulent) motions of the background plasma. At the appropriate stage of our calculations, we will also take into account the differential rotation of the Galactic disk. Since no reliable data are available, our model does not include the regular motion of the medium, for example, of the type of Galactic wind. We denote the diffusion coefficients that take into account the above factors by $\kappa_{\mu\nu}$ and $D^{p,e}_{\mu\nu}$ for relativistic protons and for thermal protons and electrons, respectively.

The currents produced by protons and electrons can be written as

$$j_\mu^p = -e\kappa_{\mu\nu}\frac{\partial N}{\partial x_\nu} - eD_{\mu\nu}^p\frac{\partial n^p}{\partial x_\nu} + \sigma_{\mu\nu}^p E_\nu, \quad (4)$$

$$j_\mu^e = eD_{\mu\nu}^e\frac{\partial n^e}{\partial x_\nu} + \sigma_{\mu\nu}^e E_\nu, \quad (5)$$

where $\sigma_{\mu\nu}^{p,e}$ are the electrical conductivities produced by background protons and electrons whose densities acquire the nonequilibrium additions n^p and n^e because of the presence of accelerated protons. A macroscopic electric field $\mathbf{E}$ can appear for the same reason. It satisfies the electrostatic equations

$$\mathbf{E} = -\nabla\varphi, \qquad \nabla^2\varphi = -4\pi e(N + n^p - n^e). \quad (6)$$

This field generates electron and proton currents that can be expressed in terms of the corresponding electrical conductivities $\sigma_{\mu\nu}^{e,p}$.

In the steady-state case, the total current $\mathbf{j}^{\rm cr} = \mathbf{j}^e + \mathbf{j}^p$ satisfies the continuity equation $\nabla\cdot\mathbf{j}^{\rm cr} = 0$, while the proton and electron currents individually satisfy the following inhomogeneous equations with sources:

$$\nabla\cdot\mathbf{j}^p = eQ(r,\alpha,z), \qquad \nabla\cdot\mathbf{j}^e = -eQ(r,\alpha,z). \quad (7)$$

Assuming that all of the diffusion coefficients and electrical conductivities are constant, we write the system of equations to determine N, n^p, n^e, φ as

$$-e\kappa_{\mu\nu}\frac{\partial^2 N}{\partial x_\mu\partial x_\nu} = eQ, \quad (8)$$

$$-eD_{\mu\nu}^p\frac{\partial^2 n^p}{\partial x_\mu\partial x_\nu} - \sigma_{\mu\nu}^p\frac{\partial^2\varphi}{\partial x_\mu\partial x_\nu} = 0, \quad (9)$$

$$eD_{\mu\nu}^e\frac{\partial^2 n^e}{\partial x_\mu\partial x_\nu} - \sigma_{\mu\nu}^e\frac{\partial^2\varphi}{\partial x_\mu\partial x_\nu} = -eQ. \quad (10)$$

Equation (6) should be added to Eqs. (8)–(10). In writing Eq. (8), we disregarded the effect of the self-consistent electric field on the motion of relativistic protons, which is a universally accepted approximation in cosmic-ray physics (see Berezinskiĭ *et al.* 1990).

After calculating the particle densities, the electric field, and the total current generated by relativistic protons, we can determine the magnetic field produced by this current in the turbulent Galactic medium. Turbulence plays a crucial role in our problem, because it acts as a major factor that causes the large-scale magnetic field to dissipate. It is also responsible for the diffusion pattern of the particle motion.

When the displacement current is ignored, the magnetic field $\mathbf{H}$, unaveraged over the turbulent motions of the medium, satisfies the equation

$$\nabla\times\mathbf{H} = \frac{4\pi}{c}(\mathbf{j}^{in} + \mathbf{j}^{\rm ext}), \quad (11)$$

where

$$j_\mu^{\rm in} = \tilde\sigma_{\mu\nu}(\mathcal{E} + \frac{1}{c}\mathbf{v}\times\mathbf{H})_\nu \quad (12)$$

is the unaveraged background plasma current that exists in the absence of relativistic particles and $\mathbf{j}^{\rm ext}$ is the extra current generated by cosmic rays. In Eq. (10), $\tilde\sigma_{\mu\nu}$ is the local (microscopic) electrical conductivity, which is different at different phases of the interstellar medium. Averaging the two sides of Eq. (11) over the turbulent motions and phase states yields

$$\nabla\times\mathbf{B} = \frac{4\pi}{c}(\mathbf{j}^{\rm pl} + \mathbf{j}^{\rm cr}), \quad (13)$$

where $\mathbf{B} = \langle\mathbf{H}\rangle$ and the averaged currents now appear on the right-hand side. The cosmic-ray current $j^{\rm cr}$ should be calculated from the above equations (4)–(10). We determine the averaged background plasma current as follows. We write

$$\mathcal{E} = \hat\sigma^{-1}\mathbf{j}^{\rm in} - \frac{1}{c}\mathbf{v}\times\mathbf{H} \quad (14)$$

and average the two sides by assuming that $\sigma_{\mu\nu} =$ const (incompressible motions; the density and temperature do not fluctuate) and $\mathbf{v} = \mathbf{u} + \mathbf{u}'$, $\langle\mathbf{v}\rangle = \mathbf{u}$, $\langle\mathbf{u}'\rangle = 0$, where $\mathbf{u}$ is the regular velocity of the medium and $\mathbf{u}'$ is the fluctuating turbulent addition. The mean $\langle\mathbf{u}'\times\mathbf{H}\rangle$ is given in the reviews of Vainshtein *et al.* (1980) and Ruzmaikin *et al.* (1988) for isotropic turbulence:

$$\langle\mathbf{u}'\times\mathbf{H}\rangle = -\nu_{\rm turb}\nabla\times\mathbf{B}, \quad \nu_{\rm turb} = \frac{1}{3}\langle u'^2\rangle\tau_{\rm c}, \quad (15)$$

where $\tau_{\rm c}$ is the correlation time of the turbulent motions and $\nu_{\rm turb}$ is the turbulent diffusion coefficient of the magnetic field (turbulent magnetic viscosity). Having averaged (14) using (15) and (11), we obtain

$$c\langle\mathcal{E}\rangle = c\mathbf{E} = -c\langle\tilde\sigma^{-1}\mathbf{j}^{\rm ext}\rangle \quad (16)$$
$$+\frac{c^2}{4\pi}\langle\tilde\sigma^{-1}\nabla\times\mathbf{H}\rangle - \mathbf{u}\times\mathbf{B} + \nu_{\rm turb}\nabla\times\mathbf{B}.$$

To estimate the terms being averaged, we substitute the inverse tensor $\tilde\sigma^{-1}$ with the scalar quantity $1/\sigma$ and disregard the correlations:

$$\langle\tilde\sigma^{-1}\mathbf{j}^{\rm ext}\rangle = \frac{1}{\sigma}\mathbf{j}^{\rm cr}, \qquad \langle\tilde\sigma^{-1}\nabla\times\mathbf{H}\rangle = \frac{1}{\sigma}\nabla\times\mathbf{B}. \quad (17)$$

Next, we apply the operation $\nabla\times$ to equality (16) and eliminate $\nabla \times \mathbf{E}$ by using the law of electromagnetic induction. We obtain an equation for the magnetic-field evolution that includes the extraneous current of relativistic particles:

$$\frac{\partial \mathbf{B}}{\partial t} = \nu\nabla^2\mathbf{B} + \nabla \times [\mathbf{u} \times \mathbf{B}] + \frac{4\pi\nu_{\rm m}}{c}\nabla \times \mathbf{j}^{\rm cr}. \quad (18)$$

Here, $\nu_{\rm m} = c^2/4\pi\sigma$ is the local magnetic viscosity and $\nu = \nu_{\rm m} + \nu_{\rm turb}$ is the total magnetic viscosity. Since the turbulent viscosity in the Galaxy exceeds the local magnetic viscosity $\nu_{\rm m}$ by many orders of magnitude, $\nu \approx \nu_{\rm turb}$.

In the static case and in the absence of regular motion, we derive the following equation from (18):

$$\nabla^2\mathbf{B} = -\frac{4\pi}{c}\frac{\nu_{\rm m}}{\nu_{\rm turb}}\nabla \times \mathbf{j}^{\rm cr}. \quad (19)$$

Note the small factor $\nu_{\rm m}/\nu_{\rm turb}$ on the right-hand side of Eq. (19). Its presence reflects the dissipation of the large-scale magnetic field through turbulent diffusion.

2. CALCULATING THE ELECTRIC CURRENT DENSITY

We seek a solution of Eqs. (6)–(10) by assuming that the Galactic medium is homogeneous, i.e., for the case where the diffusion and electrical conductivity tensors do not depend on the coordinates. These tensors for charged particles are related by (Alfvén and Feldhammer 1963)

$$\sigma^{e,p}_{\mu\nu} = \frac{D^{e,p}_{\mu\nu}}{4\pi r_D^2}, \quad (20)$$

where $r_D = \sqrt{T/4\pi n_0 e^2}$ is the Debye radius and n_0 is the equilibrium density of the background electrons and ions.

Applying a Fourier transform in coordinates yields an exact solution to the system of equations (6) and (8)–(10) for the Fourier amplitudes:

$$\varphi_k = \frac{4\pi e}{k^2}(N_k + n^p_k - n^e_k), \quad (21)$$

$$N_k = \frac{Q_k}{\widetilde{\kappa}},$$

$$n^p_k = -\frac{Q_k}{\widetilde{\kappa}}\frac{1}{1+k^2r_D^2} + \frac{Q_k}{\widetilde{D}_e}\frac{1}{2+k^2r_D^2},$$

$$n^e_k = \frac{Q_k}{\widetilde{\kappa}}\frac{1}{1+k^2r_D^2} + \frac{Q_k}{\widetilde{D}_e}\frac{1+k^2r_D^2}{2+k^2r_D^2}.$$

Here, we denote

$$\widetilde{\kappa} = \kappa_{\mu\nu}k_\mu k_\nu, \qquad \widetilde{D}_e = D^e_{\mu\nu}k_\mu k_\nu. \quad (22)$$

The diffusion coefficient for relativistic protons in the Galaxy is much larger than that for thermal electrons and $\widetilde{\kappa} \gg \widetilde{D}_e$. Therefore, the nonequilibrium additions n^p_k and n^e_k to the thermal particle densities are large compared to the relativistic proton number density N_k. Using (21) and formulas (4) and (5), we find the Fourier transform of the total current

$$j^{\rm cr}_{k\mu} = j^e_{k\mu} + j^p_{k\mu} = ieQ_k\left(\frac{D^e_{\mu\nu}k_\nu}{\widetilde{D}_e} - \frac{\kappa_{\mu\nu}k_\nu}{\widetilde{\kappa}}\right). \quad (23)$$

It follows from the latter expression that the electric current is produced by relativistic protons and nonrelativistic electrons of the background plasma. According to Eqs. (18) and (19), the magnetic field in our model is determined by the curl of the current. Note the following important property of the derived current: its curl becomes zero if the diffusion coefficients and the electrical conductivities are isotropic. Calculating $[\mathbf{k} \times \mathbf{j}^{\rm cr}_k]_\alpha = e_{\alpha\beta\mu}k_\beta j^{\rm cr}_{k\mu}$, we obtain the zero combination of the tensors $e_{\alpha\beta\mu}k_\beta k_\mu = 0$ for $\kappa_{\mu\nu} = \kappa\delta_{\mu\nu}$.

Thus, a magnetic field in a homogeneous system can be generated by a current of diffusing energetic particles only if the medium has anisotropic properties. This assertion is valid irrespective of the distribution pattern of the sources. This result can be easily understood from qualitative considerations: in the case of isotropic diffusion, a small source of relativistic particles will produce a spherically symmetric current that does not generate any magnetic field. Therefore, the field strength is very sensitive to the symmetry of the diffusion tensors and to the relationship between their components.

It should be noted, however, that in an inhomogeneous system, which the Galaxy and, in particular, the Galactic disk actually are, the curl of the current of extraneous sources can be nonzero because the diffusion coefficients are nonuniform, i.e., because they depend on coordinates. This possibility, which was not explored in our homogeneous model, is probably of great importance during the initial period of disk existence. There may have been no global large-scale magnetic field at that time, but local fields of presupernovae and supernova remnants, which produced an inhomogeneous medium, arose. An asymmetric electric current of accelerated particles in such a medium could serve as a source of the large-scale magnetic field.

3. THE DIFFUSION COEFFICIENTS

The longest-range particles are relativistic protons, for which the Galaxy-averaged value is $\kappa \approx 5 \times 10^{28}$ cm^2 s^{-1} (Berezinskii *et al.* 1990). Although the local diffusion tensor is sharply anisotropic,

$\kappa_\perp/\kappa_\parallel \approx 10^{-13}$, because of the presence of a large-scale stochastic magnetic field with $\delta B/B_0 \approx 1$ in the Galaxy, global particle transport takes place with a much more isotropic diffusion tensor, for which $\kappa_\parallel$ and $\kappa_\perp$ are of the same order of magnitude (but, of course, they are generally unequal). This question was extensively covered by Bykov and Toptygin (1992). These authors provided equations that allow the longitudinal and transverse diffusion coefficients to be calculated for an arbitrary amplitude of the large-scale stochastic magnetic field. The Hall diffusion tensor components are negligible, because the Larmor proton radius is small compared to the transport mean free path. Thus, in a coordinate system with the polar axis directed along the large-scale magnetic field, the diffusion tensor of relativistic protons is symmetric and has the components $\kappa_\parallel \neq \kappa_\perp$ that are comparable in order of magnitude.

According to observational data (Ruzmaikin *et al.* 1988), the regular magnetic field in the Galactic disk has spiral field lines that lie in the disk plane. However, for generality, we also take into account the possibility of the existence of a small magnetic field component perpendicular to the disk plane. Its presence is by no means ruled out by the available low-accuracy observations. In the presence of all three regular magnetic field components along the cylindrical coordinate axes at all points of space, the symmetric diffusion tensor $\kappa_{\mu\nu}$ will have six different nonzero components, including the cross $(\kappa_{r\alpha}, \kappa_{rz}, \kappa_{\alpha z})$ components, whose role is great in the problem under consideration. This follows from both our results (see the next section) and general considerations. Numerous antidynamo theorems (Cowling, Elsasser, Zeldovich, and others) suggest that a magnetic field can be generated in asymmetric systems. In the problem under consideration, this implies that the axes of symmetry of the diffusion tensor will not coincide with the axes of cylindrical symmetry of the Galaxy.

Denoting the angle between a field line and the cylindrical unit vector $\mathbf{e}_z$ by θ and the angle between the field projection onto the (x, y) plane and the unit vector $\mathbf{e}_r$ by γ, we write the diffusion tensor components in cylindrical (r, α, z) coordinates as

$$\kappa_{\mu\nu} = \begin{pmatrix} (\kappa_\parallel - \kappa_\perp)\sin^2\theta\cos^2\gamma + \kappa_\perp & (\kappa_\parallel - \kappa_\perp)\sin^2\theta\sin\gamma\cos\gamma & (\kappa_\parallel - \kappa_\perp)\sin\theta\cos\theta\cos\gamma \\ (\kappa_\parallel - \kappa_\perp)\sin^2\theta\sin\gamma\cos\gamma & (\kappa_\parallel - \kappa_\perp)\sin^2\theta\sin^2\gamma + \kappa_\perp & (\kappa_\parallel\sin\gamma - \kappa_\perp\cos\gamma)\sin\theta\cos\theta \\ (\kappa_\parallel - \kappa_\perp)\sin\theta\cos\theta\cos\gamma & (\kappa_\parallel\sin\gamma - \kappa_\perp\cos\gamma)\sin\theta\cos\theta & \kappa_\parallel\cos^2\theta + \kappa_\perp\sin^2\theta \end{pmatrix}. \quad (24)$$

If the toroidal (B_α) magnetic field dominates, then the angles θ and γ must be close to $\pi/2$.

Since the general structure of the diffusion tensor $D^e_{\mu\nu}$ for nonrelativistic background electrons is determined by the geometry of the large-scale magnetic field, it also has the form (24). Of course, the components of this tensor are much smaller than those for relativistic protons. However, their absolute values are of little importance, because the electric current, according to (23), depends on the ratio of the different components rather then on their absolute values.

According to Eqs. (18) and (19), the magnetic-field strength also significantly depends on the magnetic viscosities $\nu_{\rm turb}$ and $\nu_{\rm m}$. The turbulent diffusion coefficient $\nu_{\rm turb}$ of the magnetic field is easiest to estimate. Taking a commonly used value of $L \approx 100$ pc for the energy-containing interstellar turbulence scale length and $u' \approx 10$ km s^{-1} for the characteristic turbulent velocity, we obtain an estimate of $\nu_{\rm turb} \approx u'L/3 \approx 10^{26}$ cm^2 s^{-1}. Ruzmaikin *et al.* (1988) estimated $\nu_{\rm m}$ at different phases of the interstellar medium. In cold dense nonionized hydrogen clouds and in a warm phase with a large fraction of nonionized atoms, the magnetic field dissipation is attributable mainly to the ambipolar diffusion of electrons and ions through a neutral gas. The ambipolar diffusion coefficient $\nu_{\rm m}$ at these phases is 3×10^{21} and 3×10^{20} cm^2 s^{-1}, respectively. In hot bubbles, the collisionless wave damping leads to a much lower value of $\nu_{\rm m} \approx 5 \times 10^{17}$ cm^2 s^{-1}. As a result, the value averaged over the Galactic disk is $\nu_{\rm m} \approx 3 \times 10^{20}$ cm^2 s^{-1} and the ratio in Eq. (19) is

$$\frac{\nu_{\rm m}}{\nu} \approx \frac{\nu_{\rm m}}{\nu_{\rm turb}} \approx 3 \times 10^{-6}. \quad (25)$$

Below, we use this value in our numerical estimates.

4. CALCULATING THE MAGNETIC FIELD

In the steady-state formulation, the problem reduces to solving Eq. (18), in which we should set $\mathbf{u} = r\Omega(r)\mathbf{e}_\alpha$ (the differential rotation velocity of the disk) and $\partial\mathbf{B}/\partial t = 0$. In projection onto the coordinate unit vectors, it takes the form

$$\triangle B_r - \frac{B_r}{r^2} = \frac{4\pi\nu_{\rm m}}{c\nu}\frac{\partial j^{\rm cr}_\alpha}{\partial z}, \quad (26)$$

$$\triangle B_\alpha - \frac{B_\alpha}{r^2} = \frac{4\pi\nu_\mathrm{m}}{c\nu}\left(\frac{\partial j_r^\mathrm{cr}}{\partial z} - \frac{\partial j_z^\mathrm{cr}}{\partial r}\right) - \frac{B_r}{\nu}\frac{d\Omega}{dr}r,$$

$$\triangle B_z = \frac{4\pi\nu_\mathrm{m}}{c\nu r}\frac{\partial r j_\alpha^\mathrm{cr}}{\partial r}.$$

As follows from these equations, rotation does not affect the B_r and B_z components. The solution for $B_\alpha = B_\alpha^{(1)} + B_\alpha^{(2)}$ can be represented as the sum of two terms: one corresponds to the current term on the right-hand side and the other owes its presence to the poloidal B_r component and rotation. Therefore, we will first solve Eqs. (26) without rotation.

Going to a Fourier representation in the equivalent equation (19), we express the magnetic field in the form of a three-dimensional integral:

$$\mathbf{B}(r,z) = \frac{4\pi\nu_\mathrm{m}}{c\nu}\int k^{-2}[i\mathbf{k}\times\mathbf{j}_k^\mathrm{cr}]\exp[ik_\perp r \times\cos(\phi-\alpha) + ik_\parallel z]\frac{k_\perp dk_\perp d\phi dk_\parallel}{(2\pi)^3}, \quad (27)$$

where the Fourier transform of the current is given by expression (23). The subsequent passage to the cylindrical unit vectors $\mathbf{e}_r$, $\mathbf{e}_\alpha$, and $\mathbf{e}_z$ in the integrand of (27) allows the cylindrical components of the curl of the current density to be expressed as

$$[i\mathbf{k}\times\mathbf{j}_k^\mathrm{cr}]_r = -eQ_k\{T_{\alpha z}[k_\parallel^2 - k_\perp^2\sin^2(\phi-\alpha)] + T_{r\alpha}k_\parallel k_\perp\cos(\phi-\alpha)\} - eQ_k\{(T_{\alpha\alpha}-T_{zz})k_\parallel k_\perp - T_{rz}k_\perp^2\cos(\phi-\alpha)\sin(\phi-\alpha)\}, \quad (28)$$

$$[i\mathbf{k}\times\mathbf{j}_k^\mathrm{cr}]_\alpha = eQ_k\{T_{rz}[k_\parallel^2 - k_\perp^2\cos^2(\phi-\alpha)] + (T_{rr}-T_{zz})k_\parallel k_\perp\cos(\phi-\alpha)\} + eQ_k\left\{[T_{r\alpha}k_\parallel k_\perp - T_{\alpha z}k_\perp^2\cos(\phi-\alpha)]\sin(\phi-\alpha)\right\},$$

$$[i\mathbf{k}\times\mathbf{j}_k^\mathrm{cr}]_z = eQ_k k_\perp^2\left\{T_{r\alpha}[2\cos^2(\phi-\alpha)-1] + (T_{\alpha\alpha}-T_{rr})\sin(\phi-\alpha)\cos(\phi-\alpha)\right\} + eQ_\mathbf{k}k_\parallel k_\perp\left\{T_{\alpha z}\cos(\phi-\alpha) - T_{rz}\sin(\phi-\alpha)\right\}.$$

Here, we denote

$$T_{\mu\nu} = \frac{\kappa_{\mu\nu}}{\widetilde{\kappa}} - \frac{D_{\mu\nu}^e}{\widetilde{D}_e}, \quad (29)$$

where, according to (22),

$$\widetilde{\kappa} = [\kappa_{\alpha\alpha} + (\kappa_{rr}-\kappa_{\alpha\alpha})\cos^2(\phi-\alpha) + 2\kappa_{r\alpha}\cos(\phi-\alpha)\sin(\phi-\alpha)]k_\perp^2 + 2[\kappa_{rz}\cos(\phi-\alpha) + \kappa_{\alpha z}\sin(\phi-\alpha)]k_\perp k_\parallel + \kappa_{zz}k_\parallel^2. \quad (30)$$

The quantity $\widetilde{D}_e$ can be expressed in a similar way.

The integrand of the three-dimensional integral in (27) with (28)–(30) and (1) is very cumbersome, and reasonable approximations should be used when calculating it. When integrating over ϕ, we use the fact that the denominator of integrand (30) is positive for all values of ϕ. This becomes clear if we write this invariant quantity in a system of axes in which the tensor $\kappa_{\mu\nu}$ is diagonal: $\widetilde{\kappa} = \kappa_\perp k_\perp'^2 + \kappa_\parallel k_\parallel'^2 > 0$. Since the relative change in $\widetilde{\kappa}$ is small in the integration range $0 \le \phi \le 2\pi$, we substitute this quantity in the integrand with its angle-averaged value:

$$\overline{\widetilde{\kappa}} = \frac{1}{2}(\kappa_{\alpha\alpha}+\kappa_{rr})k_\perp^2 + \kappa_{zz}k_\parallel^2 \equiv \kappa_{zz}(k_\parallel^2 + a^2k_\perp^2), \quad (31)$$

$$a = \sqrt{\frac{\kappa_{\alpha\alpha}+\kappa_{rr}}{2\kappa_{zz}}}.$$

We make a similar substitution in the second denominator:

$$\overline{\widetilde{D}_e} = D_{zz}^e(k_\parallel^2 + b^2k_\perp^2), \quad b = \sqrt{\frac{D_{\alpha\alpha}^e + D_{rr}^e}{2D_{zz}^e}}. \quad (32)$$

After this simplification of the integrand, all of the integrals can be calculated without difficulty. The integrals over ϕ can be expressed in terms of the Bessel function $J_0(k_\perp r)$ and its derivatives using the formula $\int_0^{2\pi}\exp(ik_\perp r\cos\varphi)d\varphi = 2\pi J_0(k_\perp r)$. In this case, the integrals containing $\sin(\phi-\alpha)$ in the numerators of expressions (28) become zero. The integration over $k_\parallel$ between infinite limits is performed by going to a complex plane and closing the integration contour by an arc of infinite radius. Finally, the integration over $k_\perp$ between the limits $0 \le k_\perp \le \infty$ is performed by using the formula $\int_0^\infty \exp(-k_\perp R)J_0(k_\perp r)dk_\perp = \sqrt{r^2+R^2}$. After all of the integrations, we determine the magnetic field components, which we give for the Galactic-disk region $z \le h$, i.e., with an allowance made for the terms no higher than the first order in the small parameter $h/R \ll 1$:

$$B_r(r,z) = B_0(r) \times\left\{\left(\frac{\kappa_{\alpha z}}{\kappa_{zz}a(a+1)} - \frac{D_{\alpha z}^e}{D_{zz}^e b(b+1)}\right)\times\left(1-\frac{R}{\sqrt{r^2+R^2}}\right)\frac{R}{r} + \left(\frac{\kappa_{\alpha z}(a-1)}{\kappa_{zz}a(a+1)} - \frac{D_{\alpha z}^e(b-1)}{D_{zz}^e b(b+1)}\right)\frac{r}{\sqrt{r^2+R^2}} - \left(\frac{\kappa_{\alpha z}}{\kappa_{zz}(a+1)} - \frac{D_{\alpha z}^e}{D_{zz}^e(b+1)}\right)\frac{rRf(z)}{(r^2+R^2)^{3/2}} + \left(\frac{\kappa_{r\alpha}}{\kappa_{zz}(a+1)} - \frac{D_{r\alpha}^e}{D_{zz}^e(b+1)}\right)\frac{r^2 z}{(r^2+R^2)^{3/2}}\right\}, \quad (33)$$

$$B_\alpha^{(1)}(r,z) = B_0(r) \quad (34)$$

$$\times\left\{\left(\frac{\kappa_{rz}}{\kappa_{zz}a(a+1)}-\frac{D^e_{rz}}{D^e_{zz}b(b+1)}\right)\times\left(1-\frac{R}{\sqrt{r^2+R^2}}\right)\frac{R}{r}+\left(\frac{\kappa_{rz}}{\kappa_{zz}(a+1)}-\frac{D^e_{rz}}{D^e_{zz}(b+1)}\right)\frac{r}{\sqrt{r^2+R^2}}-\left(\frac{\kappa_{rz}}{\kappa_{zz}}-\frac{D^e_{rz}}{D^e_{zz}}\right)\frac{rRf(z)}{(r^2+R^2)^{3/2}}-\left(\frac{\kappa_{rr}-\kappa_{zz}}{\kappa_{zz}(a+1)}-\frac{D^e_{rr}-D^e_{zz}}{D^e_{zz}(b+1)}\right)\frac{r^2z}{(r^2+R^2)^{3/2}}\right\},$$

$$B_z(r,z)=B_0(r)\times\left\{\left(\frac{\kappa_{r\alpha}}{\kappa_{zz}a(a+1)}-\frac{D^e_{r\alpha}}{D^e_{zz}b(b+1)}\right)\times\left[\left(1-\frac{R}{\sqrt{r^2+R^2}}\right)\frac{2R}{r}-\frac{r}{\sqrt{r^2+R^2}}\right]-\left(\frac{\kappa_{\alpha z}}{\kappa_{zz}(a+1)}-\frac{D^e_{\alpha z}}{D^e_{zz}(b+1)}\right)\frac{r^2z}{(r^2+R^2)^{3/2}}\right\}. \quad (35)$$

Here, $B_0(r)$ is a dimensional factor,

$$B_0(r)=\frac{eQ_0\nu_{\rm m}}{c\nu_{\rm turb}r}, \quad (36)$$

$$f(z)=\begin{cases}|z|, & |z|>h\\ h\left[1-\frac{2}{\pi}\cos\left(\frac{\pi z}{2h}\right)\right], & |z|<h.\end{cases}$$

These magnetic field strengths are established on time scales of the order of the time it takes for the Galaxy to be filled with accelerated particles, i.e., $\approx 10^8$ yr, and are maintained as long as the particle sources work. Expressions (33)–(35) for the field components have a similar structure. Let us estimate the individual factors for the neighborhood of the Solar system ($r=10$ kpc, $z\approx h=0.2$ kpc, $R=16$ kpc, $Q_0=10^{43}$ particles s^{-1}). We take (25) for the ratio of the magnetic viscosities. In this case, the dimensional factor is $B_0(r)\approx 1.5\times10^{-5}$ G. The coordinate-dependent dimensionless factors in curly braces can be divided into two classes. Those of them that do not depend on z are equal to unity in order of magnitude. The z-containing factors are of the order of $|z|/\sqrt{r^2+R^2}\approx 10^{-2}$. All of the large and small terms also have the factors that are the differences between the ratios of the diffusion tensor components for relativistic protons and background electrons, with the principal terms containing the cross tensor components $\kappa_{r\alpha},\kappa_{rz},\kappa_{\alpha z}$. The final estimate of the magnetic field strength depends on these differences of the type, for example,

$$\frac{\kappa_{\alpha z}}{\kappa_{zz}a(a+1)}-\frac{D^e_{\alpha z}}{D^e_{zz}b(b+1)}. \quad (37)$$

According to (24), these differences can be nonzero if the magnetic field has nonzero components along all three cylindrical unit vectors. In this case, each of the terms in (37) is nonzero and a significant smallness of the difference compared to each of the terms would imply that the diffusion coefficients of relativistic protons and thermal electrons are closely correlated. Since there are no physical grounds for such a correlation, it would be natural to estimate the difference of type (37) as a quantity of the order of the first term $\kappa_{\alpha z}/\kappa_{zz}a(a+1)$. In this case, taking $\cos\theta\approx\cos\gamma\approx 0.1$ and assuming that $\kappa_\parallel$ and $\kappa_\perp$ are of the same order of magnitude, we obtain an estimate of 10^{-2} for the differences of type (37) and $B_r\approx B_z\approx 1.5\times10^{-7}$ G for the poloidal field. This yields approximately 0.1 of the observed large-scale magnetic field strength in the disk. The same estimate is also applicable to the part of the toroidal field $B^{(1)}_\alpha$ that is directly produced by the cosmic-ray current and described by formula (34). However, there is also an extra toroidal field $B^{(2)}_\alpha$ attributable to the Galactic rotation.

5. ALLOWANCE FOR THE GALACTIC ROTATION AND DISCUSSION OF THE RESULTS

The differential rotation of the Galaxy causes the B_r poloidal field component to be elongated in the direction of the linear velocity and transform into the toroidal field $B^{(2)}_\alpha$, according to Eq. (18), in which we should set $\mathbf{j}^{\rm cr}=0$:

$$\frac{\partial B^{(2)}_\alpha}{\partial t}=\nu\left(\triangle B^{(2)}_\alpha-\frac{B^{(2)}_\alpha}{r^2}\right)+B_r(r,z)\frac{d\Omega}{dr}r. \quad (38)$$

Here, the component $B_r(r,z)$ is given by expression (33) and is assumed to be a known function of the coordinates.

Bearing in mind the relative youth of our Universe and the small number of turns made by the Galactic disk in its lifetime, we solve Eq. (38) by the method of successive approximations. In the first approximation, we omit the dissipative term from (38) by assuming that dissipation initially plays a minor role. The remaining equation gives the solution

$$B^{(2)}_\alpha(r,z,t)=B_r(r,z)\frac{d\Omega}{dr}rt. \quad (39)$$

The validity range of this solution in time is determined by the requirement that the discarded dissipative term not exceed the remaining term. When substituting solution (39) into (38), we make sure that the main contribution to the omitted term comes from the term in expression (33) that contains $f(z)$

and that was doubly differentiated with respect to z, which is (in order of magnitude)

$$\frac{\nu t}{hr} B_r \frac{d\Omega}{dr} r.$$

Thus, solution (39) can be used on time scales $t < hr/\nu$. Substituting the numerical values of the quantities yields $t < 6 \times 10^{16}$ s $\approx 6 \times 10^9$ yr. Since the derived time interval is apparently close to the lifetime of the Galactic disk, solution (39) faithfully describes the toroidal field at the current epoch. Let us estimate its numerical value at $r \approx 10$ kpc by taking

$$\frac{d\Omega}{dr} r \approx 30 \text{ km s}^{-1} \times \text{ kpc} \approx 10^{-15} \text{ s}^{-1}$$

from Fig. 5.2 of the review by Ruzmaikin *et al.* (1988) and assuming that $t \approx 6 \times 10^9$ yr and $B_r \approx 1.5 \times 10^{-7}$ G. We obtain $B_\alpha \approx 9 \times 10^{-6}$ G, i.e., an enhancement of the initial poloidal field by several tens of times. Given that our estimates are approximate, this field strength is in good agreement with the observed values of $B_{\alpha\text{obs}} \approx (2\text{–}3) \times 10^{-6}$ G (see, e.g., Beck 2001). The overall geometry and magnitudes of the field vector components along the cylindrical unit vectors are consistent (at the estimation level) with the assumptions about the relative values of the diffusion tensor components for relativistic particles made in Section 3. The B_α field component has a value close to the observed value. The poloidal components are an order of magnitude smaller, which is consistent with the available observational data. Their role in the model under consideration reduces to maintaining a sufficient degree of anisotropy of the diffusion tensors.

In the homogeneous model considered above, we primarily wanted to estimate the absolute value of the magnetic field strength in the Galaxy and did not set a goal of investigating the details of its structure, symmetry, etc. To solve these questions requires a more detailed allowance for the distribution of the relativistic particle sources in the Galaxy and, in particular, its nonuniformity.

The energy balance considerations also confirm that the above field estimate is correct. Ruzmaikin *et al.* (1988) estimated the regeneration time of turbulent motions and the magnetic field in the disk due to supernova explosions to be $\sim 10^7$ yr. In this time, supernova remnants ($L = 100$ pc, supernovae explode once every 30 years) fill out the disk, distorting and turbulizing the magnetic field. However, the sources of relativistic particles are continuously working and gain energy of the order of 3×10^{40} erg s^{-1} $\times 10^{14}$ s $= 3 \times 10^{54}$ erg in this time. How much energy is required to restore the regular magnetic field $B = 3 \times 10^{-6}$ G destroyed by supernova explosions? Multiplying the disk volume $V_d \approx 4 \times 10^{66}$ cm^3 by the magnetic energy density $B^2/8\pi$, we obtain 1.6×10^{54} erg. A significant faction of this energy is replenished through the differential rotation of the disk. Therefore, the cosmic-ray energy is quite sufficient to maintain the large-scale magnetic field in the Galaxy at the observed level and provide an approximate equipartition between the magnetic (w_B) and cosmic-ray ($w_{\text{cr}} \approx w_B$) energy densities (Berezinskii *et al.* 1990).

Note that the dynamo model considered above (an enhancement of the toroidal field through the poloidal field during the differential rotation) does not lead to any field decay for $t \to \infty$. This behavior is characteristic of antidynamo theorems (see, e.g., Elsasser 1946; Zel'dovich 1956) if no cosmic-ray sources turn off. On long time scales, Eq. (38) has a steady-state solution that corresponds to a nonzero field. This solution can be written as the Fourier integral

$$B_\alpha^{(2)}(r, z) = \int_{-\infty}^{\infty} \overline{B}_\alpha(r, \lambda) \exp(i\lambda z) \frac{d\lambda}{2\pi},$$

where the Fourier transform in z can be calculated from the steady-state equation (38) and is

$$\overline{B}_\alpha^{(2)}(r, \lambda) = I_1(|\lambda| r) \int_r^\infty K_1(|\lambda| r') \overline{B}_r(r', \lambda) \frac{r'^2}{\nu}$$

$$\times \frac{d\Omega}{dr'} dr' + K_1(|\lambda| r) \int_0^r I_1(|\lambda| r) \overline{B}_r(r', \lambda) \frac{r'^2}{\nu} \frac{d\Omega}{dr'} dr'.$$

Here, $I_1(x)$ and $K_1(x)$ are the modified Bessel functions and $\overline{B}_r(r, \lambda)$ is the Fourier transform of the r field component. Expression (33) can be used to estimate the steady-state field in the disk. This expression yields

$$B_\alpha^{(2)}|_{t\to\infty} \approx B_r \frac{r^2}{\nu} \frac{d\Omega}{dr} r \approx 1.5 \times 10^{-3} \text{G},$$

which is established on time scales $t \gg hr/\nu \approx 6 \times 10^9$ yr.

CONCLUSIONS

Our model for the generation of a large-scale Galactic magnetic field is an example of the self-organization of the highly nonequilibrium Galactic plasma. Discrete sources in the disk (exploding stars) generate relativistic particles, which perturb the ambient plasma and produce an electric current. The current asymmetrically flowing out of the Galaxy generates a global magnetic field whose spatial scale length is much larger than the size of the region

occupied by the current sources. The large-scale magnetic field changes the kinetic coefficients of the background plasma by introducing anisotropy into the system and, thereby, maintaining the asymmetry in the current distribution needed to maintain the magnetic field.

This process begins immediately as the sources of relativistic particles turn on in the Galactic disk. The local magnetic fields required for effective acceleration are probably characteristic of most of the exploding stars, which are the sources of the accelerated particles. In contrast to the (α, Ω)-dynamo mechanism, our mechanism does not require the presence of a weak seed large-scale magnetic field. Initially, in the absence of a large-scale field, the required anisotropy in the current distribution can be produced through system inhomogeneity; i.e., due to the fact that the outflow of relativistic particles from the disk region is predominantly in the direction normal to its plane. Of course, this factor of system inhomogeneity and increase in the particle transport mean free paths outside the disk, which was not properly taken into account in our model, also acts in the subsequent evolutionary phases of the Galactic medium.

The suggested mechanism can produce magnetic fields in galaxies without noticeable rotation and in the absence of turbulence helicity if they contain exploding stars with a sufficient generation power of relativistic particles and a noticeable inhomogeneity of the interstellar medium, which can provide the proper asymmetry of the electric current. This mechanism is apparently possible in irregular galaxies.

In this case, the possible field strength and geometry, of course, require separate treatment.

As applied to our Galaxy, the simple, non-self-consistent model considered here suggests that the observed generation power of relativistic particles, together with the observed differential rotation velocity of the disk, is enough to explain the magnetic field observed in the Galactic disk without invoking the helicity properties of turbulent motion. To refine our conclusions, we should have solved a self-consistent problem in which the magnetic field generated by relativistic particles, gyrotropic turbulence, and differential rotation must be calculated simultaneously with the calculation of the diffusion coefficients for relativistic and background particles, which depend on the global and small-scale fields, and the diffusion coefficients for the magnetic field itself. Since this problem is complex, its solution does not appear to be a matter of the near future.

ACKNOWLEDGMENTS

We are grateful to B.V. Kuteev, V.A. Rozhanskii, and L.D. Tsendin for the discussion of the plasma aspects of the problem under consideration. This study was supported in part by the Russian Foundation for Basic Research, project no. 01-02-16654.

REFERENCES

1. H. Alfvèn and C. Fälthammar, *Cosmical Electrodynamics* (Oxford, 1963; Mir, Moscow, 1967).
2. R. Beck, Space Sci. Rev. **99**, 243 (2001).
3. R. Beck, A. Brandenburg, D. Moss, *et al.*, Ann. Rev. Astron. Astrophys. **34**, 155 (1996).
4. V. S. Berezinskii, S. V. Bulanov, V. L. Ginzburg, *et al.*, *Astrophysics of Cosmic Rays,* Ed. by V. L. Ginzburg (North-Holland, Amsterdam, 1990).
5. A. M. Bykov and I. N. Toptygin, Zh. Éksp. Teor. Fiz. **101**, 866 (1992) [Sov. Phys. JETP **74**, 462 (1992)].
6. X. Chi and A. W. Wolfendale, Nature **362**, 610 (1993).
7. W. M. Elsasser, Phys. Rev. **69**, 106 (1946).
8. A. V. Gruzinov and P. H. Diamond, Phys. Rev. Lett. **72**, 1651 (1994).
9. A. V. Gruzinov and P. H. Diamond, Phys. Plasmas **3**, 1853 (1996).
10. R. M. Kalsrud and S. W. Anderson, Astrophys. J. **396**, 606 (1992).
11. A. A. Ruzmaikin, D. D. Sokolov, and A. M. Shukurov, *Galactic Magnetic Fields* (Nauka, Moscow, 1988) (in Russian).
12. S. I. Vaĭnshtein, Ya. B. Zel'dovich, and A. A. Ruzmaikin, *Vortical Dynamo in Astrophysics* (Nauka, Moscow, 1980) (in Russian).
13. S. I. Vainshtein and R. Rossener, Astrophys. J. **376**, 199 (1991).
14. H. J. Völk and J. M. McKenzie, Astron. Astrophys. **116**, 191 (1982).
15. Ya. B. Zel'dovich, Zh. Éksp. Teor. Fiz. **31**, 154 (1956) [Sov. Phys. JETP **4**, 460 (1957)].

Translated by V. Astakhov

Astronomy Letters, Vol. 29, No. 6, 2003, pp. 383–386. Translated from Pis'ma v Astronomicheskiĭ Zhurnal, Vol. 29, No. 6, 2003, pp. 436–439.

A Weak Outburst of the Millisecond X-ray Pulsar SAX J1808.4−3658 in October 1996 as Detected from RXTE Slew Data

M. G. Revnivtsev*

Max Planck Institut für Astrophysik, Karl Schwarzschild Str. 1, 85740 Garching bei München, Germany
Space Research Institute, Russian Academy of Sciences, Profsoyuznaya ul. 84/32, Moscow, 117810 Russia
Received January 16, 2003

Abstract—Analysis of the RXTE slew data in October 1996 revealed a weak X-ray burst from the millisecond pulsar SAX J1808.4−3658. The 3–20-keV energy spectrum of the source can be described by a power law with an index of 2.0 and a (3- to 20 keV) luminosity of $\sim 1.4 \times 10^{35}$ erg s^{-1} (the distance to the source was taken to be 2.5 kpc). Because of the short exposure time, we failed to detect weak pulsations at a frequency of 401 Hz in the source. The (2σ) upper limit of the pulse fraction is ∼13%. © *2003 MAIK "Nauka/Interperiodica".*

Key words: *RXTE, pulsars, neutron stars and black holes, X-ray binaries, SAX J1808.4−3658.*

INTRODUCTION

As the sensitivity of X-ray astronomical instruments increases, weak outbursts of X-ray binary sources increasingly attract the attention of researchers. The all-sky monitor of the RXTE observatory can detect short (with a duration of several days or weeks) outbursts of Galactic sources with peak luminosities up to 10^{35}–10^{36} erg s^{-1} (see, e.g., Bradt *et al.* 2000). Observations of several neutron stars have shown that they are highly variable in this luminosity range. In particular, such behavior was observed in the transient systems Aql X-1 (Campana *et al.* 1998), 4U 1608−52 (Bradt *et al.* 2000), and SAX J1808.4−3658 (Gilfanov *et al.* 1998; Wijnands *et al.* 2001).

In 2000, the light curve of the millisecond pulsar SAX J1808.4−3658 was studied in detail using more sensitive instruments—the main instruments of the RXTE and BeppoSAX observatories. It was shown that on time scales of several days, the source's X-ray (1–5 keV) flux could change by more than a factor of 1000, with the peak luminosity being $\sim 2.5 \times 10^{35}$ erg s^{-1} (this corresponds to a flux of ∼15 mCrab). Thus, in studying the long-term evolution of X-ray sources, instruments with a threshold sensitivity of the order of or better than 1 mCrab for an exposure time shorter than 1 day acquire great importance. The RXTE slew data almost ideally satisfy this criterion.

Here, we analyze the RXTE slew data and show that on October 29, 1996, a weak X-ray outburst was detected from the millisecond pulsar SAX J1808.4−3658.

ANALYSIS OF THE OBSERVATIONS AND RESULTS

We use observational data from the PCA spectrometer of the RXTE observatory (Bradt *et al.* 1993). The spectrometer is sensitive in the 2–60 keV energy range, its effective area at an energy of ∼7 keV is ∼6400 cm^2, and its energy resolution at this energy is ∼18%. The field of view of the spectrometer—a circle with a radius of ∼1°—is limited by a collimator with a linear dependence of the transmission function on the distance from the center of the field of view.

Having no spatial resolution, the PCA spectrometer can be successfully used to localize X-ray sources. For this purpose, the RXTE observations are carried out in the scanning mode. In the absence of large intrinsic flux variations in the source, the localization accuracy can reach 1′–2′.

We processed the data using the standard LHEASOFT 5.2 software package.

The burst from the millisecond pulsar SAX J1808.4−3658 was detected from the RXTE slew data that began at 0400 UT on October 29, 1996. The observed flux peak was recorded at MJD 50385.167808. In Fig. 1, the dashed line indicates the passage of the center of the PCA field of view and the true position of the source SAX 1808.4−3658. The X-ray flux recorded by the spectrometer at this time is shown in Fig. 2. The relatively high significance of the observed flux

*E-mail: revnivtsev@hea.iki.rssi.ru

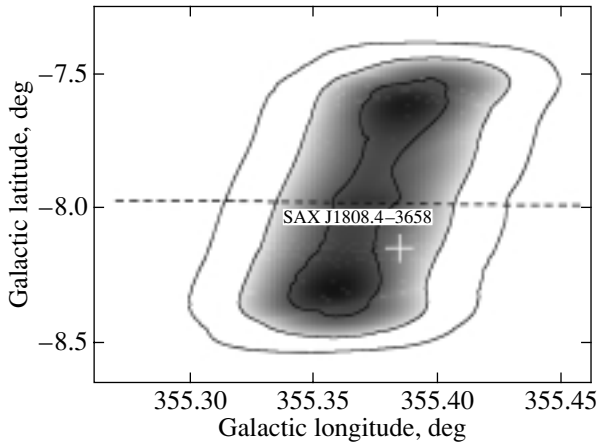

Fig. 1. The (1-, 2-, and 3-σ) localization error contours for the source as constructed from the data used. The white cross marks the position of SAX J1808.4−3658. The dashed line indicates the path of the center of the PCA field of view during repointing.

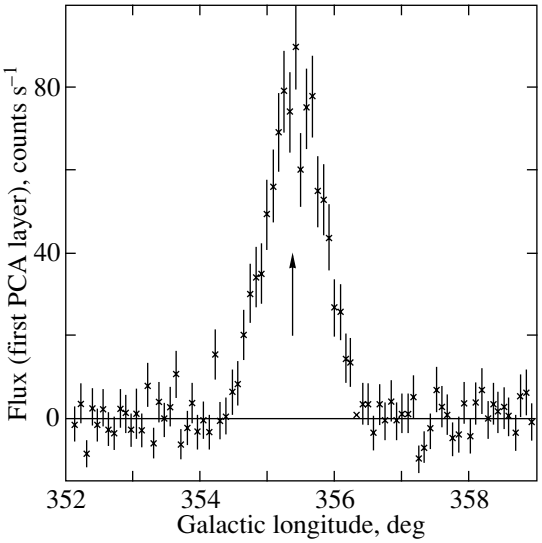

Fig. 2. PCA flux *versus* Galactic longitude of the center of the PCA field of view during the scanning observation used. The arrow indicates the sky position of the millisecond pulsar SAX J1808.4−3658.

allows us to accurately determine the Galactic longitude of the source (the statistical uncertainty is $\sim 1'-2'$). However, since no scanning was made in Galactic latitude, it can only be determined with an accuracy of no higher than $\sim 0.5°$. The 1-, 2-, and 3-σ localization error contours are shown in Fig. 1. The cross marks the exact source position obtained from optical observations (Roche 1998). In view of such a close coincidence of the above position with the position of the millisecond pulsar SAX J1808.4−3658 and as there are no other bright X-ray sources near it, we believe that the observed flux belongs to SAX J1808.4−3658.

The time the source stays within the central 0.5 ° of the PCA field of view (outside which the detector effective area decreases by more than a factor of 2) is only ~ 14 s. This exposure time is too short to record the weak pulsations at a frequency of 401 Hz that were detected in this source during its burst in the spring of 1998. The upper (2σ) limit on the pulse fraction is $\sim 13\%$.

The energy spectrum of the source obtained during the detected outburst of October 29, 1996, is shown in Fig. 3. For comparison, this figure shows the typical energy spectrum that SAX J1808.4−3658 exhibited during the brighter outburst in the spring of 1998. We see that the overall shape of the spectra is almost identical. However, because of the low statistical significance of the October 29, 1996, data, the weak spectral features, such as the fluorescence iron line at energy $\sim 6-7$ keV, observed during the outburst in the spring of 1998 (see Gilfanov *et al.* 1998; Heindl and Smith 1998), cannot be studied. The flux from SAX J1808.4−3658 recorded on October 29, 1996, in the 3- to 20-keV energy range is $F \sim 2 \times 10^{-10}$ erg s^{-1} cm^{-2}, which corresponds to a luminosity $L \sim 1.4 \times 10^{35}$ erg s^{-1} (we assumed the distance to the source to be 2.5 kpc; in't Zand *et al.* 1998, 2001). Note that the observations of the millisecond pulsar SAX J1808.4−3658 performed at approximately the same time with the WFC coded-mask telescope of the BeppoSAX observatory (in't Zand *et al.* 2001) failed to detect a statistically significant flux from the source, because the sensitivity of this telescope is lower than that of the PCA/RXTE spectrometer.

Using the PCA scanning data alone, we cannot rule out the possibility that the peak luminosity in the observed outburst was much higher than that recorded on October 29, 1996. However, the combined PCA and ASM data (Fig. 4) suggest that the peak luminosity was most likely $L \lesssim 2-3 \times 10^{35}$ erg s^{-1}.

Interestingly, the previous flux measurement of SAX J1808.4−3658 as obtained from the RXTE slew data on October 3, 1996 ($\sim$TJD 10360), yields only an upper limit of ~ 2 mCrab (Fig. 4); assuming a power-law spectrum with an index of 2.0, this corresponds to an X-ray luminosity of $< 10^{34}$ erg s^{-1} (3–20 keV, a distance of 2.5 kpc). Thus, the outburst observed on October 29, 1996, is not a continuation of the bright outburst that began in September of that year (in't Zand *et al.* 1998).

We analyzed all of the RXTE slew data for the period April 1996–November 1997. During this period, the millisecond pulsar SAX J1808.4−3658 fell within the PCA field of view 19 times. The scan dates

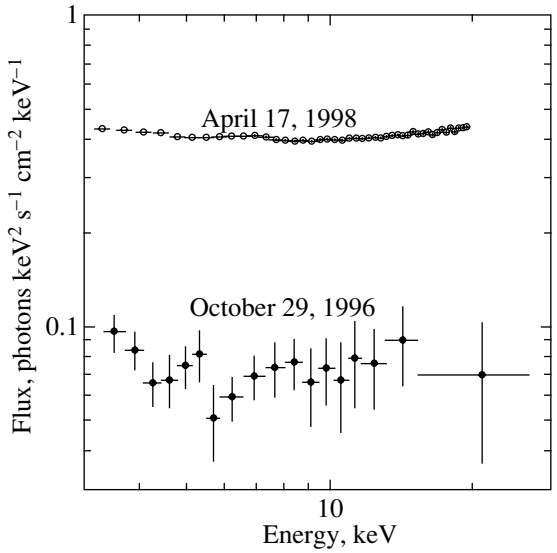

Fig. 3. The energy spectrum of SAX J1808.4−3658 on October 29, 1996 (open circles). For comparison, the filled circles indicate the energy spectrum of SAX J1808.4−3658 during its brighter outburst in the spring of 1998.

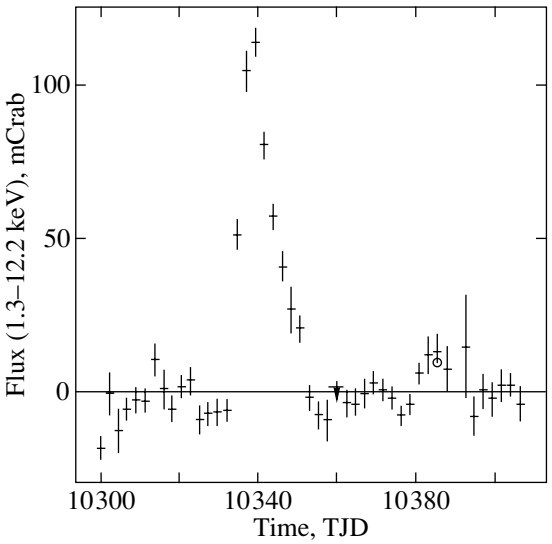

Fig. 4. The light curve of SAX J1808.4−3658 as constructed from the ASM/RXTE data. The open circle indicates the source flux as determined from the PCA data used in this paper (∼TJD 10385). The previous flux measurement of SAX J1808.4−3658 using PCA scanning data yields only an upper limit of ∼2 mCrab, which is indicated by the arrow (∼TJD 10360).

(MJD) are 50194.86, 50216.47, 50255.28, 50255.35, 50255.42, 50255.48, 50257.28, 50257.48, 50289.66, 50291.66, 50306.59, 50360.27, 50385.17, 50399.45, 50403.04, 50504.32, 50552.8, 50734.3, and 50769.5. The typical upper limits on the flux are approximately 3–5 mCrab.

DISCUSSION

In the last several years, binary systems with neutron stars (e.g., Aql X-1 and SAX J1808.4−3658) have been used as an example to show that at luminosities of $\sim 10^{35}$ erg s^{-1}, these systems often exhibit large variability (flux variations by a factor of 1000) on time scales of several days (Campana *et al.* 1998; Gilfanov *et al.* 1998; Wijnands *et al.* 2001). It seems unlikely that such large and rapid luminosity variations resulted from the development of any instabilities in the accretion disk, because the flux increase or decrease, which is assumed to be caused by such instabilities, is generally much smoother (see, e.g., Chen *et al.* 1997).

One of the plausible explanations for the observed behavior of these binary systems can be the switching of the accretion flow between two distinct states caused by small changes in the accretion rate. For rapidly rotating neutron stars (the rotation periods of the neutron stars in Aql X-1 and SAX J1808.4−3658 are 1.8 ms and 2.5 ms, respectively; Zhang *et al.* 1998; Wijnands and van der Klis 1998), two distinct states of the accretion flow can result from its interaction with the neutron-star magnetic field (Illarionov and Sunyaev 1975). As the accretion rate decreases, the size of the neutron-star magnetosphere increases and can reach the corotation radius, causing the accretion to stop due to centrifugal forces. If we assume that the threshold luminosity for the centrifugal barrier in SAX J1808.4−3658 is $L \sim 10^{35}$ erg s^{-1}, then we can estimate the surface magnetic field strength of the neutron star. A simple estimate was given, for example, by Gilfanov *et al* (1998):

$$B \sim 3 \times 10^7 M_{1.4}^{1/3} R_6^{-8/3} P_{2.5}^{7/6} \times \left(\frac{L_x}{10^{35}\ \mathrm{erg\ s^{-1}}}\right)^{1/2} \mathrm{G}. \quad (1)$$

ACKNOWLEDGMENTS

In this work, we used data from the electronic archives of the Goddard Space Flight Center. This work was supported by the Russian Foundation for Basic Research (project no. 01-02-17295) and the Nonstationary Astronomical Phenomena Program of the Russian Academy of Sciences.

REFERENCES

1. H. Bradt, A. Levine, R. Remillard, *et al.*, astro-ph/0003438 (2002).
2. H. Bradt, R. Rothschild, and J. Swank, Astron. Astrophys. Suppl. Ser. **97**, 355 (1993).
3. S. Campana, L. Stella, S. Mereghetti, *et al.*, Astrophys. J. **499**, L65 (1998).

4. W. Chen, C. Shrader, and M. Livio, Astrophys. J. **491**, 312 (1997).
5. M. Gilfanov, M. Revnivtsev, R. Sunyaev, *et al.*, Astron. Astrophys. **338**, L83 (1998).
6. W. Heindl and D. Smith, Astrophys. J. **506**, L35 (1998).
7. A. Illarionov and R. Sunyaev, Astron. Astrophys. **39**, 185 (1975).
8. P. Roche, IAU Coll. 6885 (1999).
9. R. Wijnands and M. van der Klis, Nature **394**, 344 (1998).
10. J. in't Zand, J. Heise, J. Muller, *et al.*, Astron. Astrophys. **331**, L25 (1998).
11. J. in't Zand, R. Cornelisse, and E. Kuulkers, Astron. Astrophys. **372**, 916 (2001).
12. W. Zhang, K. Jahoda, R. L. Kelley, *et al.*, Astrophys. J. **495**, L9 (1998).

Translated by G. Rudnitskii

Astronomy Letters, Vol. 29, No. 6, 2003, pp. 387–393. Translated from Pis'ma v Astronomicheskiĭ Zhurnal, Vol. 29, No. 6, 2003, pp. 440–447.

Peculiarities of Giant Pulses from the Crab Pulsar at Frequencies of 594 and 2228 MHz

S. V. Kostyuk[1], V. I. Kondratiev[1]*, A. D. Kuzmin[2], M. V. Popov[1], and V. A. Soglasnov[1]

[1] *Astro-Space Center, Lebedev Institute of Physics, Russian Academy of Sciences, Profsoyuznaya ul. 84/32, Moscow, 117997 Russia*

[2] *Pushchino Radio Astronomy Observatory, Astrospace Center, Lebedev Institute of Physics, Russian Academy of Sciences, Pushchino, Moscow oblast, 142292 Russia*

Received January 17, 2003

Abstract—We present the results of our simultaneous observations of giant pulses from the Crab pulsar B0531+21 at frequencies of 594 and 2228 MHz with a high (62.5 ns) time resolution. The pulse broadening by scattering was found to be 25 and 0.4 μs at 594 and 2228 MHz, respectively. We obtained the original giant-pulse profiles compensated for interstellar scattering. The measured profile widths at the two frequencies are approximately equal, $\approx$0.5 μs; i.e., the giant pulses are narrower than the integrated profile by a factor of about 1000. We detected an extremely high brightness temperature of radio emission, $T_b \geq 10^{36}$ K radio emission, which is higher than the previous estimates of this parameter by five orders of magnitude. The decorrelation bandwidth of the radio-spectrum diffraction distortions has been determined for this pulsar for the first time: 10 kHz at 594 MHz and 300 kHz at 2228 MHz. © *2003 MAIK "Nauka/Interperiodica".*

Key words: *pulsars, giant pulses, scattering.*

INTRODUCTION

Giant pulses (GPs)—sudden increases in intensity—are a rare phenomenon that has been detected only in four pulsars: the Crab pulsar B0531+21 (Staelin and Reifenstein 1968; Argyle and Gower 1972; Friedman and Boriakoff 1992; Lundgren *et al.* 1995), the millisecond pulsars B1937+21 (Sallmen and Backer 1995) and B1821–24 (Romani and Johnston 2001), and the pulsar B1112+50 (Ershov and Kuzmin 2003). This phenomenon is most pronounced in the first two pulsars; the intensity of their individual pulses exceeds the intensity of the integrated pulse by hundreds or thousands of times. GPs from the pulsar B0531+21 were first detected by Staelin and Reifenstein (1968). The pulse intensity for the Crab pulsar has a two-component distribution: a lognormal one for most pulses and a power-law one for GPs with intensities above a certain level that corresponds to approximately a 30-fold intensity of the integrated pulsar profile (Lundgren *et al.* 1995).

GPs are observed in both the main pulse and the interpulse. The distribution of time intervals between neighboring GPs corresponds to a Poisson process (Lundgren 1994), suggesting that each GP is emitted independently of other GPs (Lundgren *et al.* 1995; Sallmen *et al.* 1999).

Sallmen *et al.* (1999) carried out simultaneous observations of GPs at frequencies 600 and 1400 MHz. About 70% of the pulses were detected at the two frequencies simultaneously, implying an emission mechanism with a bandwidth larger than 800 MHz. It was also established that the GP shape has a complex structure. At 1400 MHz, most of the observed pulses consisted of several closely spaced components.

Simultaneous observations of the Crab pulsar at several frequencies were also carried out by other authors (Moffett and Hankins 1996; Hankins 2000). GPs can occur everywhere within the integrated profile but are never observed at the precursor phase. Moffett (1997) observed GPs at frequencies of 1.4 and 4.8 GHz, suggesting an emission band wider than 3 GHz. However, if the fine GP structure is considered, then the emission band proves to be comparatively narrow. Eilek *et al.* (2002) argue that the GP substructure is well correlated only at close frequencies: 1.4–1.7, 4.5–5.0, and 8.4–8.5 GHz. The correlation between GPs in the broader range 1.4–4.8 GHz is much weaker. These observational data are in good agreement with the model of Weatherall (1998).

* E-mail: vlad@asc.rssi.ru

1063-7737/03/2906-0387$24.00 © 2003 MAIK "Nauka/Interperiodica"

However, the basic parameters of the Crab pulsar GPs themselves—their durations, flux densities, and brightness temperatures of radio emission—have been studied inadequately. The GP duration is known to be much shorter than the duration of the integrated profile. Heiles *et al.* (1970) determined the GP width $W_{50}^{GP} < 100$ μs at 430 MHz. Given this estimate, the observed GP peak flux densities correspond to a brightness temperature $T_b > 10^{31}$K. Kuzmin *et al.* (2002) found the GP scattering time at a close frequency (406 MHz) to be 180 ± 80 μs. Given the measurement errors, this value corresponds to the GP widths measured by Heiles *et al.* (1970). The possibility of measuring shorter pulses is limited by the pulse broadening by interstellar scattering.

Isaacman and Rankin (1977) observed the Crab pulsar for five years at frequencies from 73.8 to 430 MHz. These authors studied the integrated pulsar profiles, for which they determined the scattering time scale by means of modeling. The model of a scattering medium in which the bulk of the scattering matter is contained in a very limited region proved to correspond best to the observed integrated-profile shapes. The Crab Nebula, in which there are areas with a matter density much higher than the interstellar density, may well be this region. This explanation was first offered by Matveenko and Lotova (1970). Kuzmin *et al.* (2002) measured the frequency dependence of the broadening time of GPs from the Crab pulsar in the range from 40 to 2228 MHz. The form of the frequency dependence corresponds to the normal distribution of interstellar irregularities.

To reduce the effect of the interstellar medium on the pulsar radio emission, observations should be carried out at high frequencies, at which the scattering effect is smaller. However, even at frequencies of 600 and 1400 MHz, at which the GPs from this pulsar were studied by Sallmen *et al.* (1999), the GP width measurements are limited by the pulse broadening by scattering. According to the authors, this broadening is 95 μs at 600 MHz and 2.5 μs at 1400 MHz.

We observed GPs from the pulsar B0531+21 at frequencies of 594 and 2228 MHz and determined their durations, flux densities, and brightness temperatures. To restore the true pulsar GP profile, we compensated the GPs for the pulse broadening by scattering (Kuzmin and Izvekova 1993). The decorrelation bandwidth of the radio-spectrum diffraction distortions for this pulsar has been determined for the first time.

OBSERVATIONS AND DATA PROCESSING

We observed the pulsar B0531+21 on May 19 and 20, 2000, with the 64-m radio telescope at the Kalyazin Radio Astronomy Observatory (Astrospace Center, Lebedev Institute of Physics, Russian Academy of Sciences) at frequencies of 594 and 2228 MHz simultaneously. Radio emission with left-hand circular polarization was received at each frequency. We used the S2 data recording system designed for VLBI observations (Cannon *et al.* 1997; Wietfeldt *et al.* 1998). The signal in a 16-MHz frequency band was continuously recorded on magnetic tapes. The signal was digitized by a two-bit binary code with four quantization levels at the Nyquist frequency. The time resolution of the recording system was 62.5 ns at 2228 MHz and 125 ns at 594 MHz. Next, information from the magnetic tapes was read into the computer memory using the S2-TCI system (Kempner *et al.* 1997; Popov *et al.* 2002a; Popov *et al.* 2002b). The received data, presented in the internal S2-TCI format, were decoded and the original video signal was written on computer hard disk.

Subsequently, the signal was corrected for dispersion by the predetection dispersion method (Hankins 1971, 1974). The dispersion measure DM = 56.754 pc cm^{-3} was used to restore the signal. This value was taken from the ephemeris of the dispersion measure for the Crab pulsar for May 15, 2000 (the date closest to the time of our observations), which are computed at the Jodrell Bank Observatory (England) for the middle of each month (Jodrell Bank Crab Pulsar Monthly Ephemeris). During the data processing, we refined this dispersion measure (see below in this section).

The correction for the receiver band-pass amplitude irregularities was made by the method suggested by Semenkov *et al.* (2003). The idea is to construct an average power spectrum of the record at a noise window, which is the amplitude–frequency characteristic (AFC) of the receiver band-pass. For this AFC, we chose an appropriate "ideal band" and then calculated the correcting function.

We searched for GPs over the entire length of the record. Only for performing the searching procedure did we average the detected signal corrected for dispersion smearing and the receiver band-pass amplitude irregularities with a time constant of 28 μs for the record at 594 MHz and 312.5 ns for the record at 2228 MHz. In our subsequent data processing, unless otherwise specified, we used records with an original time resolution of 62.5 ns at 2228 MHz and 125 ns at 594 MHz. Then, we searched for GPs. We analyzed the record portions in which the signal level exceeded a threshold value; the remaining part of the records was not processed. The threshold was 5σ (310 Jy) at 594 MHz and 10σ (2700 Jy) at 2228 MHz. The flux-density calibration procedure is described in more detail in the subsection entitled "GP Flux Densities and Brightness Temperatures."

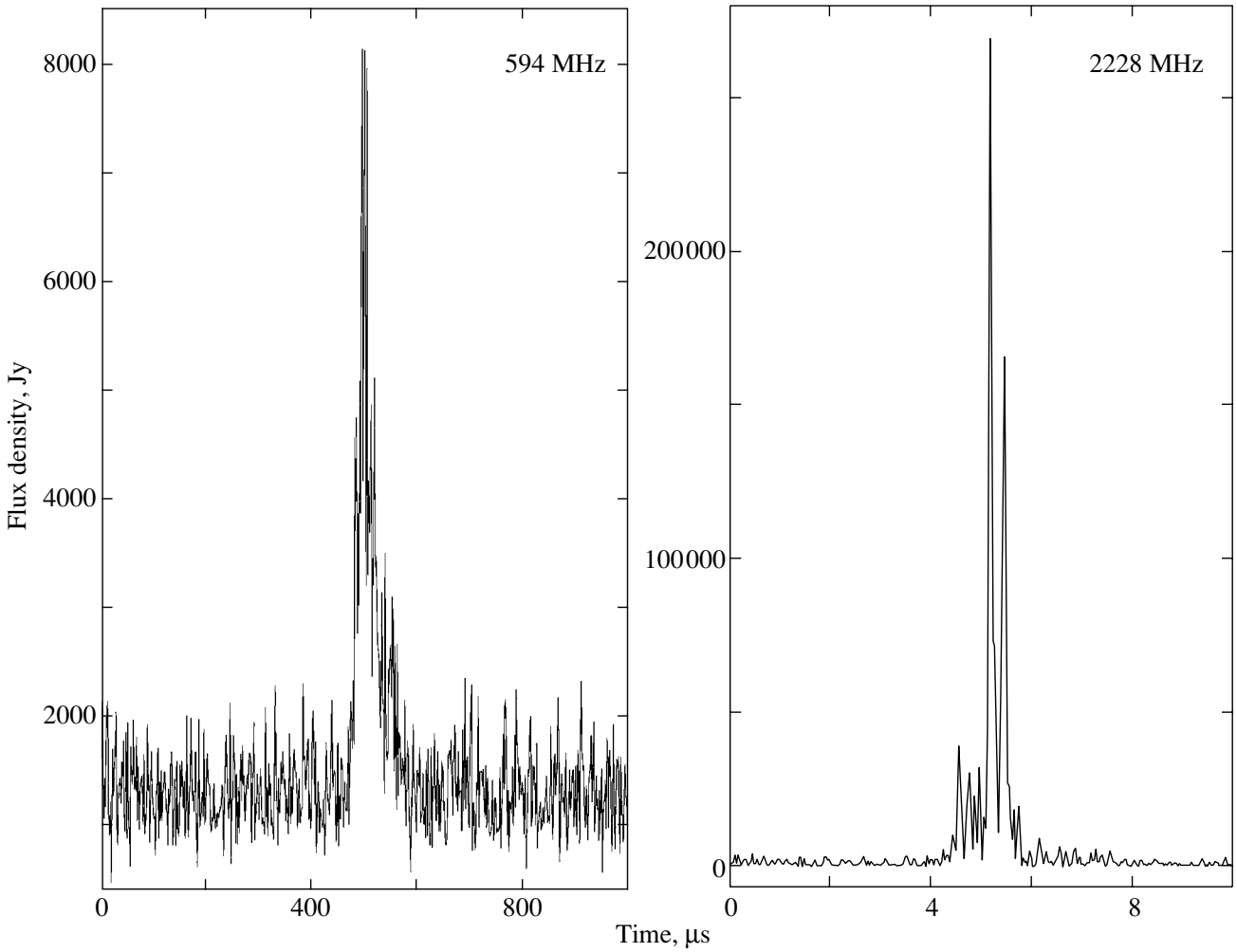

Fig. 1. The giant pulse detected simultaneously at the two frequencies. The pulse at 2228 MHz is shown with an original time resolution of 62.5 ns. The pulse at 594 MHz was averaged with a time constant of 1.5625 μs.

The selected data were checked for the presence of GPs. The following two criteria were used for GP selection: (i) an excess over a specified threshold at the phase of the integrated profile and (ii) the characteristic GP scattering profile. The noise spikes were excluded from the data processing.

The duration of an observing session was 6 h. By now, we have processed the data which contain 36 364 pulsar period in a 20-min-long record. At 594 MHz, we detected 349 GPs: 300 (about 86%) and 49 (14%) were observed at the phases of the main pulse and the interpulse, respectively. At 2228 MHz, we found 65 pulses: 56 (86%) and 9 (14%) at the phases of the main pulse and the interpulse, respectively. One GP with an intensity higher than the above threshold occurred, on average, in 100 pulsar periods at 594 MHz and in 560 periods at 2228 MHz; 22 of these pulses were observed simultaneously at the two frequencies (one such pulse is shown in Fig. 1). Based on the dispersion delay of the pulses simultaneously observed at the two frequencies, we refined the dispersion measure, DM $= 56.764 \pm 0.001$ pc cm^{-3}.

ANALYSIS AND RESULTS

Pulse Broadening by Scattering

Averaging the GPs aligned by the peak flux density, we obtained the integrated GP profile. Note that averaging the GPs by the peak flux density leads to a certain narrowing of the derived integrated profiles. In our case, however, this narrowing may be ignored, because the width of the scattered profile is much larger than the sampling interval. Subsequently, we determined the broadening of the derived integrated GP profiles by modeling the scattering effect. To this end, we folded the template that represented the original pulsar GP profile with the truncated exponential function

$$g(t) = \begin{cases} \exp(-t/\tau_{sc}) & \text{for} \quad t \geq 0 \\ 0 & \text{for} \quad t < 0, \end{cases} \qquad (1)$$

Parameters of GPs from the pulsar B0531 + 21

Frequency, MHz	N	τ_{sc}, μs	S_{max}^{obs}, kJy	W_{50}^{obs}, μs	S_{max}^{GP}, kJy	W_{50}^{GP}, μs
594	300	25	2.5	30	150	0.5
2228	56	0.4	9	1	18	0.5

Note: N is the number of observed GPs (at the phase of the main pulse); τ_{sc} is the time of pulse broadening by scattering; S_{max}^{obs} is the N-averaged GP peak flux density; W_{50}^{obs} is the mean width of the observed GP at half maximum; S_{max}^{GP} is the mean peak flux density of the GPs compensated for scattering; and W_{50}^{GP} is the measured width of the GP profiles compensated for scattering at half maximum. All of the measured parameters in this table were obtained by analyzing the GPs that were observed only at the phase of the main pulse.

that represented the scattering by a thin screen. The observed integrated profile was fitted (by the least squares method) with the modeled profile. A Gaussian profile was specified as the template. The broadening by scattering τ_{sc}, the template profile width, and the time delay of the scattered model profile were the sought-for parameters. The integrated GP profile at 594 MHz was averaged over ten data counts (312.5 ns). The measured pulse broadening by scattering is $\tau_{sc} = 25$ and 0.4 μs at 594 and 2228 MHz, respectively (see the table).

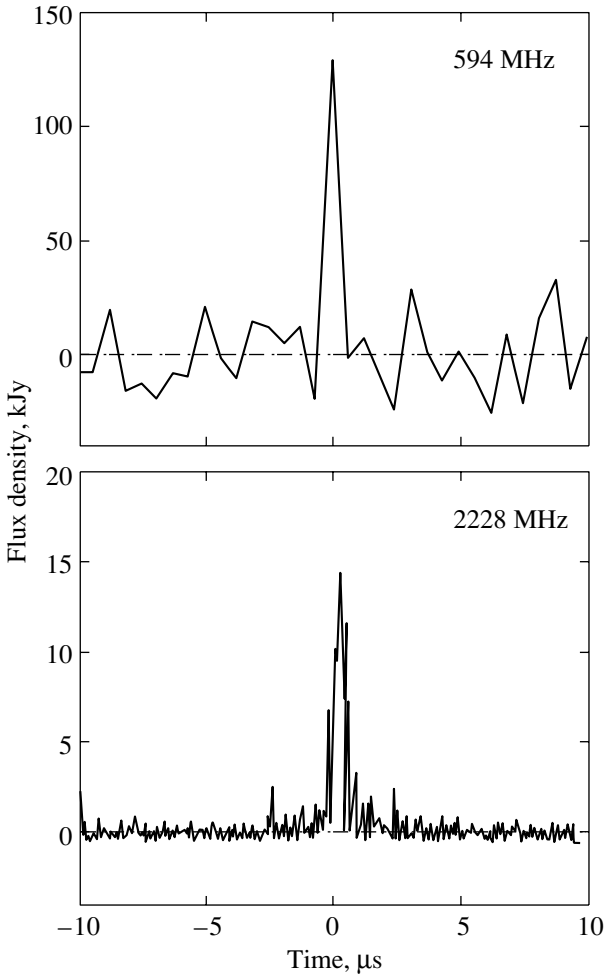

Fig. 2. The scattering-compensated integrated GP profiles at frequencies of 594 and 2228 MHz.

The difference between the durations of the observed pulsar pulses does not correspond to the actual difference between the original pulsar pulses. The observed pulsar GPs are distorted by interstellar scattering, which limits the possibility of measuring pulses shorter than the broadening by scattering. Using our scattering data, we restored the original GP profile by the method of Kuzmin and Izvekova (1993). This method is based on the classical solution of the relationship between the pulse parameters at the input and output of some element (medium) with the transfer function $g(t)$ through which the pulse passes; that is known in the theory of transient processes. The frequency spectra of the original, $x(t)$, and observed, $y(t)$, pulses are related by $X(f) = Y(f)/G(f)$, where $G(f)$ is the frequency response of the scattering medium,

$$G(f) = \frac{1}{2\pi}\int g(t)\exp(-j2\pi tf)dt.$$

The frequency spectrum of the observed pulse is determined by the Fourier transform

$$Y(f) = \frac{1}{2\pi}\int y(t)\exp(-j2\pi tf)dt.$$

The scattering-compensated pulse is determined by the inverse Fourier transform of its spectrum

$$x(t) = \frac{1}{2\pi}\int X(f)\exp(j2\pi tf)df.$$

In our case, the transfer element is the interstellar medium whose transfer function $g(t)$ is given by formula (1).

The scattering-compensated integrated GP profiles are shown in Fig. 2. The widths of the restored GP profiles are approximately equal at the two frequencies, $W_{50}^{GP} \approx 0.5$ μs = 0.015 mP (see the table), which is a thousand times smaller than the width of the integrated pulsar profile.

The Decorrelation Band

To determine the decorrelation bandwidth $\Delta\nu_s$, we constructed the autocorrelation function (ACF) of the scintillation frequency structure. For this purpose, we constructed the ACFs of the power spectra for each GP on a record portion with a length of 512 μs at

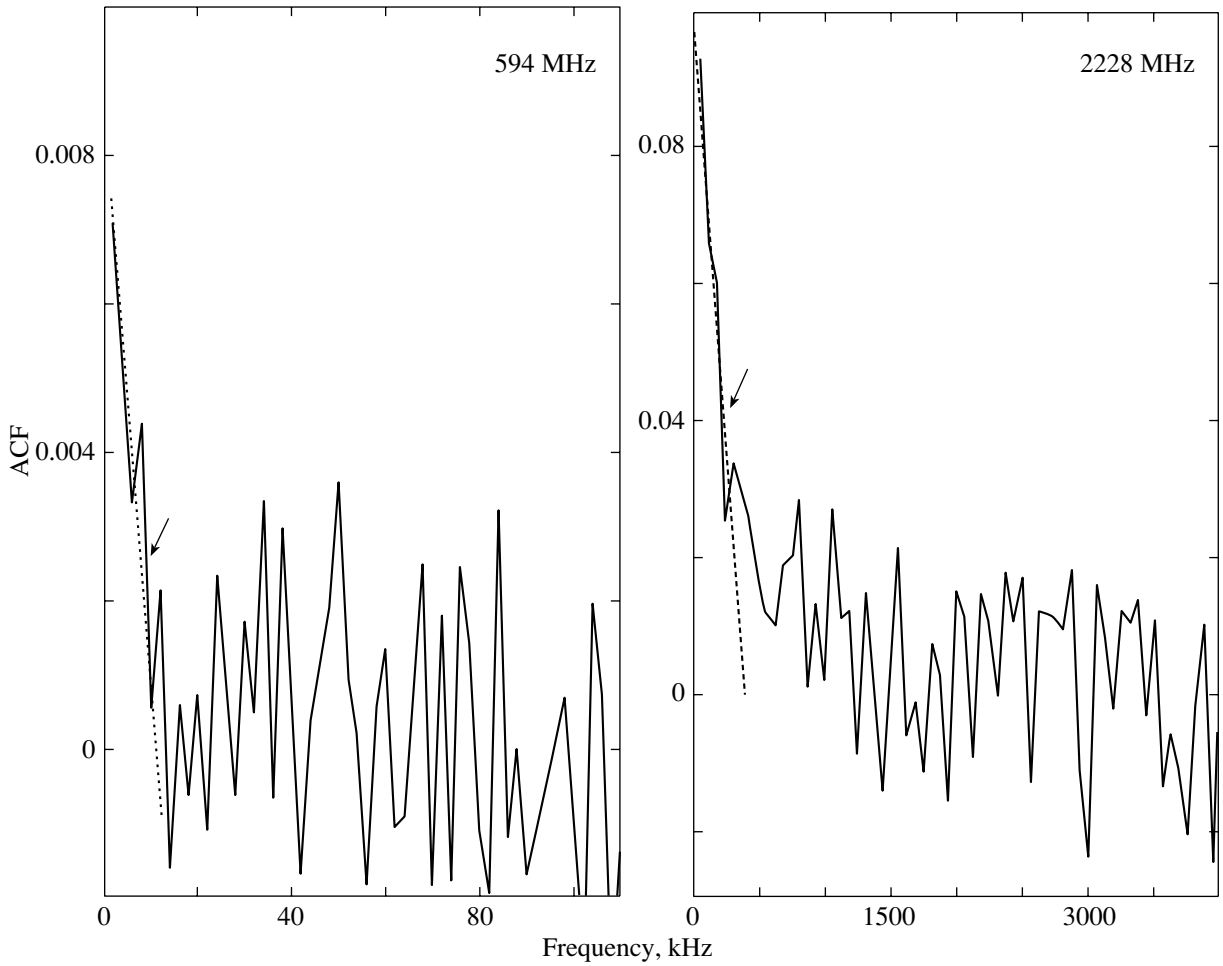

Fig. 3. The autocorrelation functions of the scintillation frequency structure at 594 and 2228 MHz. The arrows indicate the characteristic $\Delta\nu_s$ scales: 10 and 300 kHz at 594 and 2228 MHz, respectively. The sampling intervals at 594 and 2228 MHz are 2 and 62.5 kHz, respectively.

594 MHz and 16 μs at 2228 MHz, which provided a frequency resolution of 2 and 62.5 kHz, respectively. The derived ACFs were then averaged between themselves. The frequency ACF on the noise record portion was constructed in a similar way and then subtracted from the ACF for the GP. The decorrelation bandwidth was determined from the characteristic scale of the derived ACF (see Fig. 3): 10 kHz at 594 MHz and 300 kHz at 2228 MHz.

GP Flux Densities and Brightness Temperatures

The calibration was made as follows. The system equivalent flux density (SEFD) of the radio telescope σ_s was 170 Jy at 594 MHz and 160 Jy at 2228 MHz. In our case, however, σ_s was determined mainly by the contribution from the radio emission of the Crab Nebula. At 594 and 2228 MHz, the beam width is 27′ and 7′, respectively, which is larger than the angular size of the Crab Nebula. Therefore, σ_s was determined by the total contribution from the background of the entire Crab Nebula at the observation frequencies and the noise of the antenna–feeder system. The flux densities of the Crab Nebula at 594 and 2228 MHz are 1100 and 710 Jy, respectively. These flux densities were obtained by interpolating the data published by Ivanov *et al.* (1994) and Velusamy *et al.* (1992). The final SEFD of the radio telescope σ_s is 1300 and 800 Jy at 594 and 2228 MHz, respectively.

We calculated the fluctuation rms outside the pulse window. The GP flux density S_{GP} was defined by the expression

$$S_{GP} = \sigma_s \times (S/N),$$

where (S/N) is the signal-to-noise ratio.

The peak flux density averaged over 300 observed pulses at 594 MHz was 2500 Jy. The peak flux density averaged over 56 observed pulses at 2228 MHz was 9000 Jy.

The measured flux density at the maximum of the observed pulse $S_{\max}^{\rm obs}$ was recalculated with the conservation of the pulse energy to the scattering-compensated GP maximum as $S_{\max}^{\rm GP} = S_{\max}^{\rm obs} \times (W_{50}^{\rm obs}/W_{50}^{\rm GP})$, where $W_{50}^{\rm obs}$ is the width of the observed GP and $W_{50}^{\rm GP}$ is the scattering-compensated GP width.

The mean peak flux densities of the scattering-compensated GPs at 594 and 2228 MHz are 150 and 18 kJy, respectively, which exceed the flux density at the maximum of the integrated profile by factors of 60 000 and 500 000, respectively.

Our results are presented in the table.

The brightness temperature is $T_{\rm b} = S_{\max}^{\rm GP}\lambda^2/2k\Omega$, where λ is the wavelength of the received radio emission; k is the Boltzmann constant; and Ω is the solid angle of the radio-emitting region, $\Omega \cong \theta^2 = (l/d)^2$. Assuming that the distance to the pulsar is $d = 2$ kpc (Taylor *et al.* 1995) and that the size of the radio-emitting region is $l \le cW_{50}^{\rm GP}$, where $W_{50}^{\rm GP} = 0.5$ μs is the GP width, we obtain $T_{\rm b} \ge 2 \times 10^{36}$ and $T_{\rm b} \ge 1.6 \times 10^{34}$ K at 594 and 2228 MHz, respectively.

The GP Emission Frequency Band

We observed 22 pulses simultaneously at the two frequencies, 594 and 2228 MHz, suggesting an emission mechanism.

DISCUSSION

The widths of the scattering-compensated GP profiles at 594 and 2228 MHz are approximately equal, suggesting that the derived profile is similar to the original pulsar GP profile.

The (period-averaged) flux densities of the integrated pulsar pulse at 594 and 2228 MHz were found by extrapolating the data from the catalog of Taylor *et al.* (1995) to be 220 and 3.2 mJy, respectively; they are equal to 2400 and 35 mJy at the pulse maximum. Thus, in the observed GPs, the flux densities averaged over 300 and 56 strong GPs at 594 and 2228 MHz are 150 and 18 kJy, respectively, which exceed the mean level by factors of 60 000 and 500 000.

The GP brightness temperature is $T_{\rm b} \ge 10^{36}$ K, a value that is five orders of magnitude higher than the previous estimates of this parameter. The brightness temperature estimated by Soglasnov *et al.* (2003) for the millisecond pulsar B1937+21, which also exhibits GPs, are $>10^{38}$ K, while Kuzmin and Losovsky (2002) gave $\approx 10^{35}$ K, which is equal in order of magnitude to the value obtained for the Crab pulsar.

An independent measurement of the decorrelation band and the pulse broadening by scattering at the same frequency and for a common sample of pulses made it possible to experimentally determine the relation between these parameters, $2\pi\tau_{\rm sc}\Delta\nu_{\rm s} = K$. Our measured $\tau_{\rm sc} = 25$ μs and $\Delta\nu_{\rm s} = 10$ kHz at 594 MHz and $\tau_{\rm sc} = 0.4$ μs and $\Delta\nu_{\rm s} = 300$ kHz at 2228 MHz correspond to the recalculation coefficients $K = 1.57$ and 0.75, respectively. The coefficient K depends on the spectrum of the interstellar plasma irregularities in the line of sight. For a Gaussian irregularity spectrum, $K = 1$, although, as was shown by Rickett (1977), the same is also roughly valid for a power-law spectrum. The K range for the two frequencies used here contains the theoretical value for this coefficient. This coefficient was also measured by other authors. Slee *et al.* (1980) obtained $K = 1.0 \pm 0.1$ for the pulsar B0833–45.

CONCLUSIONS

We observed giant pulses from the Crab pulsar B0531+21 at frequencies of 594 and 2228 MHz.

We obtained the GP profiles of this pulsar that were compensated for interstellar scattering. The profile width is $W_{50}^{\rm GP} \approx 0.5$ μs.

The GP peak flux densities at 594 and 2228 MHz are 150 and 18 kJy, respectively, which exceed the flux density at the maximum of the integrated profile by factors of 60 000 and 500 000, respectively.

We detected an extremely high GP brightness temperature, $T_{\rm b} \ge 10^{36}$ K, which is five orders of magnitude higher that the previous estimates of this parameter.

The frequency bandwidth of the GP radio emission is not less than 1.5 GHz.

We carried out the first direct measurements of the decorrelation band for this pulsar. The decorrelation bandwidth $\Delta\nu_{\rm s}$ is 10 kHz at 594 MHz and 300 kHz at 2228 MHz.

ACKNOWLEDGMENTS

The Kalyazin observations were carried out with the pulsar instrumentation operated by the Department of Pulsar Astrometry at the Pushchino Radio Astronomy Observatory, Astrospace Center, Lebedev Institute of Physics, Russian Academy of Sciences. We wish to thank Yu.P. Ilyasov and V.V. Oreshko for help with the data acquisition system. We are also grateful to S.F. Likhachev and A.V. Chibisov for operating the S2-TCI system and V.A. Samodurov for updating the program for determining the time of broadening by scattering. This study was supported in part by the Russian Foundation for Basic Research (project nos. 01-02-16326 and 01-02-16871) and the "Nonstationary Processes in Astronomy" Program of the Presidium of the Russian Academy of Sciences.

REFERENCES

1. E. Argyle and J. F. R. Gower, Astrophys. J. Lett. **175**, L89 (1972).
2. W. H. Cannon, D. Baer, G. Feil, *et al.*, Vistas Astron. **41**, 297 (1997).
3. J. A. Eilek, P. N. Arendt, Jr., T. H. Hankins, and J. C. Weatheroll, *Proc. of the 270 WE-Heraeus Seminar on Neutron Stars, Pulsars, and Supernova Remnants. MPE Report*, Ed. by W. Becker *et al.* (Max-Plank-Institut für Extraterrestrische Physic, Garching bei München, 2002), p. 249.
4. A. A. Ershov and A. D. Kuzmin, Pis'ma Astron. Zh. **29**, 111 (2003) [Astron. Lett. **29**, 91 (2003)].
5. J. F. Friedman and V. Boriakoff, *The Magnetospheric Structure and Emission Mechanisms of Radio Pulsars, Proc. of IAU Colloq. 128*, Ed. by T. H. Hankins, J. M. Rankin, and J. A. Gil (Pedagogical Univ. Press, Zielona Gora, 1992), p. 347.
6. T. H. Hankins, Astron. Soc. Pac. Conf. Ser. **202**, 165 (2000).
7. T. H. Hankins, Astrophys. J. **169**, 487 (1971).
8. T. H. Hankins, Astron. Astrophys. Suppl. Ser. **15**, 363 (1974).
9. C. Heiles, D. B. Campbell, and J. M. Rankin, Nature **226**, 529 (1970).
10. R. Isaacman and J. M. Rankin, Astrophys. J. **214**, 214 (1977).
11. V. P. Ivanov, K. S. Stankevich, and S. P. Stolyarov, Astron. Zh. **71**, 737 (1994) [Astron. Rep. **38**, 654 (1994)].
12. Jodrell Bank Crab Pulsar Monthly Ephemeris, http://www.jb.man.ac.uk/pulsar/crab.html
13. J. C. Kempner, D. R. Stinebring, M. Bailes, *et al.*, Abstracts of Papers, Am. Astron. Soc. Meeting No. 191 (1997), p. 111.19.
14. A. D. Kuz'min and V. A. Izvekova, Mon. Not. R. Astron. Soc. **260**, 724 (1993).
15. A. D. Kuzmin and B. Ya. Losovsky, Pis'ma Astron. Zh. **28**, 25 (2002) [Astron. Lett. **28**, 21 (2002)].
16. A. D. Kuzmin, V. I. Kondrat'ev, S. V. Kostyuk, *et al.*, Pis'ma Astron. Zh. **28**, 292 (2002) [Astron. Lett. **28**, 251 (2002)].
17. S. C. Lundgren, A Multi-Wavelength Study of Rotation-Driven Pulsars, Ph.D. Thesis (Cornell University, Ithaca, New York, 1994).
18. S. C. Lundgren, J. M. Cordes, M. Ulmer, *et al.*, Astrophys. J. **453**, 433 (1995).
19. L. I. Matveenko and N. A. Lotova, Astron. Zh. **47**, 483 (1970) [Sov. Astron. **14**, 388 (1970)].
20. D. A. Moffett, Ph.D. Thesis (New Mexico Inst. Mining and Technology, New Mexico, 1997).
21. D. A. Moffett and T. H. Hankins, Astrophys. J. **468**, 779 (1996).
22. M. V. Popov, N. Bartel, W. H. Cannon, *et al.*, Astron. Astrophys. **396**, 171 (2002a).
23. M. V. Popov, N. Bartel, W. H. Cannon, *et al.*, Astron. Zh. **79**, 229 (2002) [Astron. Rep. **46**, 206 (2002b)].
24. J. M. Rankin, J. M. Comella, H. D. Craft, Jr., *et al.*, Astrophys. J. **162**, 707 (1970).
25. B. J. Rickett, Ann. Rev. Astron. Astrophys. **15**, 479 (1977).
26. R. W. Romani and S. Johnston, Astrophys. J. Lett. **557**, L93 (2001).
27. S. Sallmen and D. C. Backer, Astron. Soc. Pac. Conf. Ser. **72**, 340 (1995).
28. S. Sallmen, D. C. Backer, T. H. Hankins, *et al.*, Astrophys. J. **517**, 460 (1999).
29. K. V. Semenkov, M. V. Popov, V. A. Soglasnov, and Kh. Hirabayashi, Pis'ma Astron. Zh. **29**, 116 (2003) [Astron. Lett. **29**, 96 (2003)].
30. O. B. Slee, G. A. Dulk, and R. E. Otrupcek, Proc. Astron. Soc. Aust. **4**, 100 (1980).
31. V. A. Soglasnov, M. V. Popov, N. Bartel, *et al.*, Astron. Astrophys. (2003, in preparation).
32. D. H. Staelin and E. C. Reifenstein III, Science **162**, 1481 (1968).
33. J. H. Taylor, R. N. Manchester, A. G. Lyne, and F. Camilo, Catalog of 706 Pulsars (1995, unpublished); http://pulsar.princeton.edu/pulsar/catalog.shtml.
34. T. Velusamy, D. Roshi, and V. R. Venugopal, Mon. Not. R. Astron. Soc. **255**, 210 (1992).
35. J. C. Weatherall, Astrophys. J. **506**, 341 (1998).
36. R. D. Wietfeldt, W. Van Straten, D. Del Rizzo, *et al.*, Astron. Astrophys. Suppl. Ser. **131**, 549 (1998).

Translated by V. Astakhov

Astronomy Letters, Vol. 29, No. 6, 2003, pp. 394–399. Translated from Pis'ma v Astronomicheskiĭ Zhurnal, Vol. 29, No. 6, 2003, pp. 448–454.

A Dissipative Model of Interacting Winds for WR 140: A Comparison with Observations

S. A. Zhekov[1] and A. V. Myasnikov[2*]

[1] *Space Research Institute, Bulgarian Academy of Sciences, Sofia, Bulgaria*

[2] *Institute for Problems of Mechanics, Russian Academy of Sciences, pr. Vernadskogo 101, Moscow, 117526 Russia*

Received December 5, 2002

Abstract—A comparison between the stellar-wind interaction model with electron heat conduction and the ASCA X-ray observations of the (WR+O) binary system WR 140 has been made for the first time. This comparison shows that good agreement with observations can be achieved by varying the physical stellar-wind parameters within the ranges allowed by the accuracy of their determination. The self-consistent two-temperature model with heat conduction is an outgrowth of the model of interacting winds in such systems, which is required to properly interpret future detailed X-ray observations on the Chandra and Newton-XMM satellites. © *2003 MAIK "Nauka/Interperiodica".*

Key words: *hydrodynamics, stellar-wind interaction, X-ray sources, WR 140.*

INTRODUCTION

Because of substantial progress in sensitivity and spectral resolution, X-ray spectroscopy has become one of the most powerful tools for studying the properties of stellar winds and interstellar environments of Wolf–Rayet (WR) stars. X-ray spectra provide detailed information on the temperature distribution behind the shock waves generated in strong winds from these stars. In the long run, they are capable of providing reliable information on the wind chemical composition, which is used to test evolutionary models. Most of the studies are focused on WR+O binary systems, because the X-ray brightness of the interaction region of the stellar winds from their components can significantly exceed the brightness of single WR and O stars (Pollock 1987). Of particular interest are the X-ray spectra of the binaries WR 140 (WC7 + O4-5V) and γ^2 Vel (WC8 + O9I) that have recently been obtained on the ASCA (Advanced Satellite for Cosmology and Astrophysics) spacecraft. These spectra have a high signal-to-noise ratio and, hence, are suitable for a detailed comparison with theoretical models. A comparison between the ASCA spectra of γ^2 Vel obtained at different orbital phases and the spectra computed in the model of radiative interacting winds (Stevens *et al.* 1992) was made by Stevens *et al.* (1996). Unfortunately, as Myasnikov *et al.* (1998) showed, the numerical models of radiative interacting winds cannot yet be considered acceptable not only for a quantitative analysis but also for a qualitative analysis of the processes in close binary systems, where the effect of radiative energy losses in the interaction region plays a significant role.

In contrast to γ^2 Vel, the separation between the components in WR 140 is so large (Williams *et al.* 1990) that the radiative effects may be disregarded (Stevens *et al.* 1992; Myasnikov and Zhekov 1993). A detailed comparison of the spectra for WR 140 with the synthetic spectrum generated by gas-dynamical models was made by Zhekov and Skinner (2000). The main goal of their comparison was to study the question of whether the adiabatic model of interacting winds (Lebedev and Myasnikov 1988, 1990) is suitable for a detailed reproduction of the observed spectra. Although the adiabatic model was found to be capable of accurately reproducing the spectra of WR 140 at various orbital phases, allowing for the difference between the electron and ion temperatures in the interaction region leads to a better reproduction of the observational data.

At the same time, the effect of electron heat conduction on the structure of the stellar-wind interaction region in WR 140 can also be significant. Recently, Myasnikov and Zhekov (1998) suggested an interaction model of stellar winds in binary systems, in which the effect of electron heat conduction on the flow pattern was considered in the single-temperature approximation. The authors showed that electron heat conduction could significantly change the flow parameters. As a result, the X-ray spectrum

[*] E-mail: myas@ipmnet.ru

becomes softer and the luminosity increases in comparison with the purely adiabatic case.

Here, we investigate the effects of electron heat conduction on the X-ray parameters of the stellar-wind interaction region in the binary system WR 140.

THE MODEL

We took the stellar-wind outflow parameters, the binary orbital parameters, and the distance to the object from Williams *et al.* (1990) as the basic data for using the gas-dynamical model in our computations. The outflow parameters are: $\dot{M}(\mathrm{WR}) = 5.7 \times 10^{-5}\ \mathrm{M}_\odot\ \mathrm{yr}^{-1}$, $v_\infty(\mathrm{WR}) = 2860\ \mathrm{km\ s}^{-1}$, $\dot{M}(\mathrm{O}) = 1.8 \times 10^{-6}\ \mathrm{M}_\odot\ \mathrm{yr}^{-1}$, and $v_\infty(\mathrm{O}) = 3200\ \mathrm{km\ s}^{-1}$. The binary orbit has the semimajor axis $a = 14.7$ AU, the eccentricity $e = 0.84 \pm 0.04$, the orbital inclination $i = 60^\circ$, the period $P = 2900\ (\pm 10)$ days $= 7.94$ yr, and the time of periastron passage $T_0(1985.26) =$ JD2446160 (± 29). The distance to the object was assumed to be 1.3 kpc.

Since the binary system is wide and the parameter $\Lambda = \dfrac{\dot{M}_{\mathrm{WR}} V_{\mathrm{WR}}}{\dot{M}_{\mathrm{O}} V_{\mathrm{O}}}$ is equal to 28.3, the shock-wave structure is located far enough from the two stars to assume that the velocities of the two winds reach their terminal values long before the shock waves (Lebedev and Myasnikov 1990). In addition, the orbital velocities around the common center of mass in wide binary systems are low compared to the terminal wind velocities, so we may disregard the spatial effects of the orbital motion and consider the structure of the interaction region in the axisymmetric approximation. In this case, the solution of the gas-dynamical problem is completely determined by the stellar-wind outflow parameters and the separation between the components. The density in the interaction region is known to decrease with increasing separation between the components at a fixed parameter Λ, causing the effect of radiative energy losses on the structure of the interaction region to weaken (Stevens *et al.* 1992; Myasnikov and Zhekov 1993). The separation between the components in WR 140 is so large that we may completely disregard the radiative energy losses in the interaction region. At the same time, the possible effect of electron heat conduction is enhanced as the separation between the components increases, causing (at a fixed Λ) the density in the interaction region and ahead of the shock fronts to decrease (Myasnikov and Zhekov 1998). Therefore, we used the model with electron heat conduction that was suggested and developed previously (Myasnikov and Zhekov 1998) in our computations of the structure of the stellar-wind interaction region in WR 140. In this model, the flow structure is described by the system of equations in dimensionless form

Table 1. Basic parameters of the gas-dynamical models of interacting winds in WR 140

Parameter	Model A	Model B
$\dot{M}(\mathrm{WR})$, $\mathrm{M}_\odot\ \mathrm{yr}^{-1}$	2.90×10^{-5}	3.23×10^{-5}
$V(\mathrm{WR})$, $\mathrm{km\ s}^{-1}$	2860	2430
$\dot{M}(\mathrm{O})$, $\mathrm{M}_\odot\ \mathrm{yr}^{-1}$	9.20×10^{-7}	1.02×10^{-6}
$V(\mathrm{O})$, $\mathrm{km\ s}^{-1}$	3200	2720
$a \sin i$, AU	23.1	30.3
i, deg	60	60

$$\frac{\partial \rho}{\partial t} + \boldsymbol{\nabla} \cdot (\rho \mathbf{v}) = 0,$$

$$\frac{\partial \rho \mathbf{v}}{\partial t} + \boldsymbol{\nabla} \cdot (\rho \mathbf{v} \otimes \mathbf{v} + p\mathbf{I}) = 0, \qquad (1)$$

$$\frac{\partial e}{\partial t} + \boldsymbol{\nabla} \cdot ((e + p)\,\mathbf{v}) = -\Gamma_{\mathrm{thc}} \boldsymbol{\nabla} \cdot \mathbf{W},$$

where ρ, p, $\mathbf{v}$, and e denote the density, pressure, velocity, and total energy density, respectively; $\otimes$ is the tensor product; $\mathbf{I}$ is a unit matrix; and $\mathbf{W}$ is the isotropic heat flux defined by the relation $\mathbf{W} = -T^{5/2} \boldsymbol{\nabla} T$ (Braginskii 1957), $T = p/\rho$. At a fixed adiabatic index, $\gamma = 5/3$, the flow structure in the hypersonic approximation is described by the dimensionless parameters

$$\Lambda = \frac{\dot{M}_{\mathrm{WR}} V_{\mathrm{WR}}}{\dot{M}_{\mathrm{O}} V_{\mathrm{O}}}, \quad \chi = \frac{V_{\mathrm{WR}}}{V_{\mathrm{O}}},$$

$$\Gamma_{\mathrm{thc}} = 0.0742 \frac{\varepsilon(Z)}{Z} \mu^{3.5} V_{\mathrm{O}(8)}^5 D_{12} \dot{M}_{\mathrm{O}\,(6)}^{-1}$$

where μ is the mean particle atomic weight, Z is the mean ion charge, $\varepsilon(Z)$ is a function with the asymptotic values $\varepsilon(1) = 3.1616$ and $\varepsilon(\infty) = 12.47$ (Braginskii 1957), $D_{(12)} = D/10^{12}$ cm ($2D = a$), $V_{\mathrm{O}(8)} = V_{\mathrm{O}}/10^8\ \mathrm{cm\ s}^{-1}$, and $\dot{M}_{\mathrm{O}(6)} = \dot{M}_{\mathrm{O}}/10^{-6} M_\odot\ \mathrm{yr}^{-1}$.

In contrast to the adiabatic model (Myasnikov and Zhekov 1993), we disregarded the different chemical compositions of the stellar winds in our gas-dynamical computations with an allowance made for heat conduction. Since the X-ray parameters of the interaction region are determined mainly by the wind radiation from a WR star (Myasnikov and Zhekov 1993), the chemical composition in our gas-dynamical computations was assumed to be a helium one: $\mu = 4/3$, $Z = 2$, and $\varepsilon(Z) = 4.89$.

Table 2. Comparison of our computations with observations[a]

Model	Parameter	93A[b]	93B[b]	97A[b]	97B[b]
A	χ^2_{red}	1.09	0.71	1.18	1.33
	K[c]	238	200	178	178
	N_H[d]	3.01 [2.93–3.09]	1.08 [1.03–1.13]	0.32 [0.30–0.33]	0.32 [0.30–0.33]
	Norm[e]	1.00 [0.98–1.03]	1.00 [0.97–1.03]	0.96 [0.93–0.98]	0.98 [0.95–1.00]
	F_X[f]	3.42	3.23	2.38	2.50
B	χ^2_{red}	1.01	0.69	0.91	1.05
	K[c]	238	200	178	178
	N_H[d]	3.32 [3.24–3.40]	1.24 [1.19–1.29]	0.37 [0.35–0.39]	0.37 [0.36–0.39]
	Norm[e]	1.00 [0.98–1.03]	0.97 [0.94–1.01]	0.90 [0.88–0.92]	0.92 [0.89–0.94]
	F_X[f]	3.32	3.10	2.26	2.38

[a] The comparison was made by using XSPEC based on the gas-dynamical model with electron heat conduction. The 90% confidence interval is given in square brackets. The distance to WR 140 was assumed to be 1.3 kpc.

[b] The dates of observations are denoted as follows: 93A for June 10, 1993; 93B for October 26, 1993; 97A for May 14, 1997; and 97B for November 21, 1997.

[c] The degrees of freedom in the χ^2 fit.

[d] The column density (10^{22} cm^{-2}) of the extra X-ray absorption (interstellar and circumstellar). The absorption by the stellar wind was also taken into account in our computations of the X-ray emission.

[e] A dimensionless quantity that gives the observed-to-theoretical flux ratio. Norm = 1.0 corresponds to a perfect match between the quantities being compared.

[f] The observed X-ray (0.5–10 keV) fluxes in 10^{-11} erg cm^{-2} s^{-1}.

Because of the large eccentricity, the separation between the components significantly varies with orbital phase. This variation is taken into account in our steady-state model by the dependence of Γ_{thc} on the orbital parameter $D_{(12)}$. This approximation is valid for WR 140, because its orbital period is much longer than the gas-dynamical time scale of the problem ($P \gg \tau_d = D/V_O$).

To take into account the effect of the entire plasma capable of emitting in the X-ray range, we performed our computations of the interaction region up to distances of 7.5 a from the axis of symmetry, where the temperature of the emitting plasma was $T \geq 5 \times 10^5$ K.

The X-ray emission from the interaction region was determined from the model of an optically thin plasma by using the approximation of Raymond and Smith (1977). In computing the X-ray parameters, we used the chemical composition characteristic of a WC star, as in Zhekov and Skinner (2000). The absorption in the winds was determined by integrating the absorption coefficient over the line of sight for each element (Balucinska-Church and McCammon 1992) with an allowance made for the wind chemical composition. Although the solution of the gas-dynamical problem is two-dimensional, three-dimensional integration should be performed to determine the absorption at various orbital phases.

RESULTS

As was noted above, X-ray observations are the best method for testing the models of interacting stellar winds in binary systems. Therefore, we compared the computed X-ray spectrum of the interaction region with the ASCA spectra taken during 1993–1997. A description of these observations and their reduction can be found in Zhekov and Skinner (2000). Here, we only note that the spectra were obtained on June 10, 1993 (93A); October 26, 1993 (93B); May 14, 1997 (97A); and November 21, 1997 (97B). The quality of the X-ray spectra is high: each has more than 10 000 photons in the energy range (0.5–10) keV, which allows a detailed comparison with theoretical models. To this end, we used the XSPEC X-ray spectrum processing package (version 11.0; Arnaud 1996).

First, we computed spectra with the parameters of the two adiabatic models by Zhekov and Skinner (2000) (see Table 2 in this paper) that provide the best fit to the observations. Recall that these models

differ by the stellar-wind velocities. More specifically, the stellar-wind velocities in one of them are 15% lower than the standard values from Williams *et al.* (1990), which is within the limits of the errors in the wind velocities of hot stars (Prinja *et al.* 1990). The corresponding shapes of the theoretical spectra also turned out to be acceptable in the heat-conducting case. However, the X-ray flux in the two models increased by 40–50% compared to the adiabatic case, which corresponds to our general predictions (Myasnikov and Zhekov 1998).

To achieve the best agreement between the theoretical and observed spectra, we varied the mass-loss rates of the stars and the separations between the components in each of the models. In this case, the ratio of dynamic wind pressures Λ was constant.

Table 1 gives the parameters of the two models that provide the best fit to the observational data. Figure 1 shows the temperature distributions in the stellar-wind interaction region in WR 140 obtained for model A by computing a two-dimensional axisymmetric flow with electron heat conduction at orbital phases near periastron and apastron (Figs. 1a, 1b). For comparison, Fig. 1c also shows the temperature distributions computed for model A in the adiabatic approximation (at $\Gamma_{\rm thc} = 0$). The theoretical and observed spectra are compared in Table 2 and Fig. 2. This comparison shows that the interacting-wind models with heat conduction are in good agreement with the observations if the orbital semimajor axis of WR 140 lies within the range $a \sin i =$ 20–30 AU. These values slightly exceed those obtained by Zhekov and Skinner (2000) for the adiabatic case. However, they are consistent with the observations, because the orbital inclination of WR 140 is known with a low accuracy. For example, the analysis by Williams *et al.* (1990) indicated that any values in the range $i = 30°$–$90°$ were possible, while in our analysis we took the standard value of $i = 60°$. In addition, as in the adiabatic case (Zhekov and Skinner 2000), the mass loss rates of the two winds proved to be lower than those of Williams *et al.* (1990), but they remained within the range of the characteristic accuracy of these parameters.

It should be noted that, in addition to the models whose parameters are given in Table 1, other solutions that provide acceptable agreement with the observations are also possible. For example, the gas-dynamical solution has such a structure that any combination of the physical parameters of the binary system (the stellar mass loss rates, the wind velocities, and the separation between the components) that yield the same values of Λ and χ and small changes in $\Gamma_{\rm thc}$ ($\leq$30%) as in models A and B, while preserving the $\dot{M}_{\rm WR}^2/D$ ratio, will reproduce the X-ray spectra of WR 140 with an acceptable accuracy.

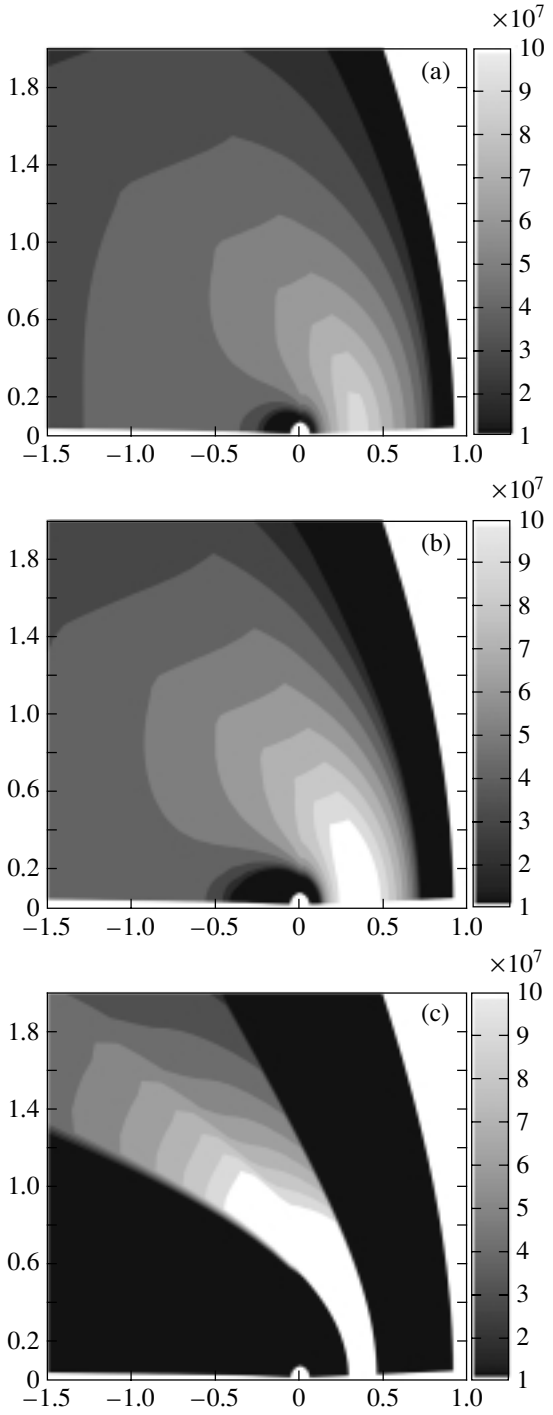

Fig. 1. The temperature distributions in the range 1×10^7–1×10^8 K near the axis of symmetry of the stellar-wind interaction region in WR 140. The distributions were obtained for model A (see Table 1) by computing a two-dimensional axisymmetric flow with electron heat conduction at orbital phases near (a) apastron and (b) periastron. The temperature distributions computed for model A in the adiabatic approximation (c) are also shown for comparison. The linear sizes refer to half the separation between the components, $D = 3.54 \times 10^{14}$ cm in case (a) and $D = 1.24 \times 10^{14}$ cm in cases (b) and (c).

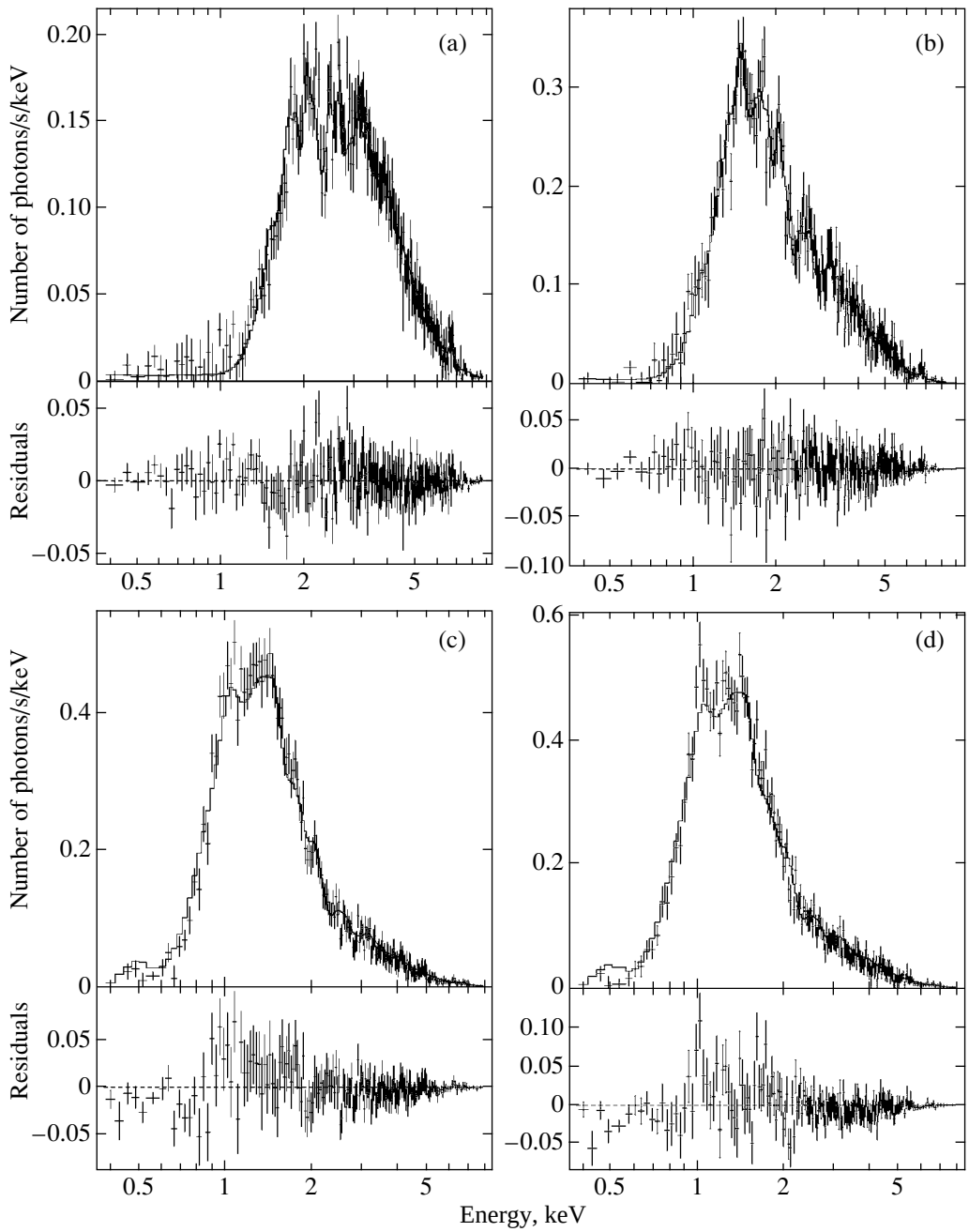

Fig. 2. The ASCA spectra of WR 140 obtained on (a) June 10, 1993; (b) October 26, 1993; (c) May 14, 1997; and (d) November 21, 1997. The heavy solid lines indicate the theoretical spectra in the heat-conducting model B with X-ray absorption by the stellar winds and the interstellar medium. The model parameters and the results of our comparison are given in Tables 1 and 2. The lower panels of each figure show the differences between the observed and model spectra (residuals).

Our analysis of the X-ray spectra for WR 140 based on a numerical interacting-wind model with heat conduction confirmed the conclusion drawn from the adiabatic model. More specifically, the X-ray absorption toward the object at orbital phases near apastron (97A and 97B) is mainly determined by the interstellar medium (based on $E(B-V) = 0.79$ from Williams *et al.* (1990), we found the expected column density of the interstellar medium to be $N_{\rm H} = 5.4 \times 10^{21}$ cm^{-2}). Extra X-ray absorption higher than the interstellar one is observed near periastron (93A and 93B) (Table 2; we took into account the absorption in the stellar winds when computing the X-ray emission). As was discussed by Zhekov and Skinner (2000), the origin of this excess

X-ray absorption is not yet known and we hope that Chandra observations will be useful in this respect.

Summarizing the results of our analysis of the X-ray spectrum for WR 140, we can say that the adiabatic and dissipative models of interacting winds indicate that the parameters giving softer emission are in better agreement with the observational data (cf. $\chi^2_{\rm red}$ for models A and B from Table 3 in Zhekov and Skinner (2000) and Table 2 in this paper). Softer X-ray emission can be obtained if (1) we decrease the stellar-wind velocities (model B in comparison with model A); (2) abandon the hypothesis that the electron and ion temperatures become equal at the shock fronts; and (3) the electron heat conduction significantly affects the structure of the interaction region. Note that in the case of WR 140, allowing for the effect of electron heat conduction causes the luminosity to increase, while the relaxation of the electron temperature causes it to decrease compared to the adiabatic model (see Table 2 in Zhekov and Skinner (2000)) an admissible change in the orbital parameter $a \sin i$. A self-consistent allowance for the combined action of these effects can be useful in interpreting more detailed observations of this object.

Finally, it should be noted that WR 140 is a well-known source of nonthermal radio emission among the WR+O binaries (Abbott *et al.* 1986), which is produced by the accelerated motion of relativistic particles in a magnetic field. The latter, in turn, significantly reduces the thermal conductivity in the direction perpendicular to the magnetic field lines (Braginskii 1957). The following question naturally arises: How much will the interaction of a magnetic field with the heat conduction in wide binary systems change the results of our analysis of the X-ray emission from WR 140. The solution of the gas-dynamical problem with anisotropic heat conduction is technically difficult to obtain and requires a three-dimensional approach. However, one might expect that the results obtained above will not change qualitatively, because the magnetic field in the binary cannot be parallel to the shock fronts everywhere.

CONCLUSIONS

A comparison between the stellar-wind interaction model with electron heat conduction and the X-ray observations of the WR+O binary system WR 140 has been made for the first time. Comparison with ASCA spectra shows that good agreement with observations can be achieved by varying physical stellar-wind parameters within the ranges allowed by the accuracy of their determination. This confirms that electron heat conduction plays a significant role in the physics of interacting stellar winds in wide binary systems. The self-consistent two-temperature model with heat conduction that we are currently developing is an outgrowth of the model of interacting winds in such binary systems, which is required to properly interpret detailed X-ray observations.

REFERENCES

1. D. C. Abbott, J. H. Bieging, E. Churchwell, and A. V. Torres, Astrophys. J. **303**, 239 (1986).
2. K. A. Arnaud, *Astronomical Data Analysis Software and Systems V*, Ed. by G. Jacoby and J. Barnes (ASP, San Francisco, 1996), p. 17.
3. M. Balucinska-Church and D. McCammon, Astrophys. J. **400**, 699 (1992).
4. S. I. Braginskiĭ, Zh. Éksp. Teor. Fiz. **33**, 459 (1957) [Sov. Phys. JETP **6**, 595 (1958)].
5. M. G. Lebedev and A. V. Myasnikov, *Computational Methods in Aerodynamics*, Ed. by V. M. Paskonov and G. S. Roslyakov (Izd. Mos. Gos. Univ., Moscow, 1988), p. 3.
6. M. G. Lebedev and A. V. Myasnikov, Izv. Akad. Nauk SSSR, Mekh. Zhidk. Gaza **4**, 159 (1990).
7. A. V. Myasnikov and S. A. Zhekov, Mon. Not. R. Astron. Soc. **260**, 221 (1993).
8. A. V. Myasnikov and S. A. Zhekov, Mon. Not. R. Astron. Soc. **300**, 686 (1998).
9. A. V. Myasnikov, S. A. Zhekov, and N. A. Belov, Mon. Not. R. Astron. Soc. **298**, 1021 (1998).
10. A. M. T. Pollock, Astrophys. J. **320**, 283 (1987).
11. R. K. Prinja, M. J. Barlow, and I. D. Howarth, Astrophys. J. **361**, 607 (1990).
12. J. C. Raymond and B. W. Smith, Astrophys. J. Suppl. Ser. **35**, 419 (1977).
13. I. R. Stevens, J. Blondin, and A. M. T. Pollock, Astrophys. J. **386**, 265 (1992).
14. I. R. Stevens, M. F. Corcoran, A. J. Willis, *et al.*, Mon. Not. R. Astron. Soc. **283**, 589 (1996).
15. P. M. Williams, K. A. van der Hucht, A. M. T. Pollock, *et al.*, Mon. Not. R. Astron. Soc. **243**, 662 (1990).
16. S. A. Zhekov and S. L. Skinner, Astrophys. J. **538**, 808 (2000).

Translated by V. Astakhov

Astronomy Letters, Vol. 29, No. 6, 2003, pp. 400–404. Translated from Pis'ma v Astronomicheskiĭ Zhurnal, Vol. 29, No. 6, 2003, pp. 455–460.

Eight New Magnetic Stars with Large Continuum Depressions

V. G. El'kin, D. O. Kudryavtsev*, and I. I. Romanyuk

Special Astrophysical Observatory, Russian Academy of Sciences, Nizhnii Arkhyz, 357147 Karachai-Cherkessian Republic, Russia

Received November 30, 2002

Abstract—Observations with the 6-m telescope revealed eight new magnetic, chemically peculiar stars: HD 29925, HD 40711, HD 115606, HD 168796, HD 178892, HD 196691, HD 209051, and BD + 32°2827. Zeeman observations of all these objects have been carried out for the first time. We selected candidates by analyzing the depression profile at a wavelength of λ5200 Å. This technique for selecting candidate magnetic stars was shown to be efficient: we found magnetic fields in 14 of the 15 objects that we selected for our observations with a Zeeman analyzer. A maximum longitudinal field strength B_e exceeding 8 kG was found in HD 178892; in HD 209051 and HD 196691, B_e reaches 3.3 and 2.2 kG, respectively. For the remaining stars, we obtained lower limits of the longitudinal field (more than several hundred G).

Key words: *stars—variable and peculiar.*

INTRODUCTION

In this paper, we continue to publish the results of our searches for new magnetic stars based on the observations performed in 2000–2002 with the 6-m Special Astrophysical Observatory (SAO) telescope. The formulation of the problem, the observing technique, and the first measurements that revealed six new magnetic stars were presented previously (El'kin *et al.* 2002). Here, we consider the technique for selecting candidate magnetic stars in more detail.

Although the first magnetic star was discovered by Babcock back in 1947, only a little more than 200 of them are known to date (Romanyuk 2000), which is not enough to carry out statistical studies. High-resolution Zeeman spectra, which can be obtained only with large telescopes whose observing time is highly deficient, are needed for direct magnetic-field measurements. The direct result of Zeeman-spectrum measurements is only the longitudinal magnetic-field component B_e, which depends on the rotation phase. Hence, it is necessary to measure at least three or four spectra of each star at different rotation phases to get an idea of its field strength. Therefore, seeking for effective criteria for selecting real candidate magnetic stars is of considerable importance.

Our suggested technique for selecting candidates is based on the analysis of the depression profile at a wavelength of λ5150 Å. We selected 15 CP stars with the most prominent feature at λ5150 Å. Previously (El'kin *et al.* 2002), we reported the discovery of six new magnetic stars; in this paper, we present the results of our new measurements that revealed magnetic fields in eight more CP stars. The last star from this list, HD 161321, was found to be an SB2 binary Am star. The results of our measurements of Zeeman spectra for this object will be published separately.

OBSERVATIONS

Since the essence of our star-selection technique for observations with the 6-m telescope equipped with a Zeeman analyzer has not been described previously in sufficient detail (El'kin *et al.* 2002), let us fill in the gap. The technique is as follows.

(1) Objects with large photometric indices characteristic of CP stars (e.g., the index Δa (Maitzen 1976) or the z parameter of the Geneva photometric system (Cramer and Maeder 1980)) are selected from the literature; the comments on individual stars made by analyzing objective-prism (Bidelman 1981, 1985) and other surveys are taken into account. We selected more than 500 objects as preliminary candidates for our subsequent observations.

(2) The stars selected by the method described above are observed using the UAGS spectrograph with a low spectral resolution attached to the 1-m SAO telescope in the region of the well-known depression at a wavelength of λ5200 Å. Such observations are not very time-consuming; the necessary data for more than 30 objects can be obtained on a successful night. When reducing these (low-resolution)

*E-mail: dkudr@sao.ru

1063-7737/03/2906-0400$24.00

Table 1. General parameters of the sample CP stars

Star HD/HDE	Alternative name	Coordinates (2000.0)		V magnitude	Spectral type
		α	δ		
HD 29925	BD+00°830	$04^h\,43^m\,00\overset{s}{.}4$	+01° 06′ 28″	8.3	B9 Si
HD 40711	BD+10°973	06 01 01.3	+10 24 05	8.6	A0 SrCrEu
HD 115606	BD+13°2653	13 18 02.5	+13 00 00	8.6	A2 Sr
	BD+32°2827	16 59 23.5	+32 27 08	9.9	Ap SrEuCr
HD 168796	BD+13°3612	18 21 02.6	+13 49 00	7.9	A0 SiCrSr
HD 178892	BD+14°3811	19 09 54.7	+14 57 58	8.9	B9 SrCrEu
HD 196691	BD−06°5545	20 39 10.6	−06 09 27	8.6	A0 Si
HD 209051	BD−07°5683	22 00 40.2	−06 25 57	8.8	A0 SrCrEu

spectra, we detected a characteristic feature within the depression at a wavelength of λ5150 Å. Its intensity well correlates with the field strength of the known magnetic stars that we took as standards for various calibrations. Moreover, we found that the presence of this feature in the profile of the broad and shallow depression in the spectrum is an effective indicator of the presence of a magnetic field in a star. We compiled a list that currently contains about 100 CP stars with a distinct feature at λ5150 Å, which we consider to be real candidate magnetic CP stars. Only special observations with a Zeeman analyzer can give the ultimate answer to the question of whether there is a magnetic field in the stellar atmosphere.

Magnetic observations of our selected CP stars with strong depressions were carried out in 2000–2002 using the Main Stellar Spectrograph (MSS) of the 6-m telescope equipped with a Zeeman analyzer (Naidenov and Chuntonov 1976; Chuntonov 1997). The detector was a 1160 × 1040 pixel CCD array. The current status of the MSS and its technical characteristics were presented by Panchuk (2001), our technique for measuring stellar magnetic fields was detailed by Romanyuk *et al.* (1998), and the data reduction procedures were described by Kudryavtsev (2000).

Table 1 presents data on the eight CP stars that we observed. It gives the HD or HDE star numbers, alternative names, equatorial coordinates α and δ for 2000, visual V magnitudes, spectral types, and types of chemical anomalies.

All of the observations were carried out in the spectral range 4450–4620 Å. The spectral resolution (two CCD pixels) was 0.3 Å, or 20 km s^{-1}. For five of the eight stars, the value of $v \sin i$ was below this limit; in these cases, we give only the upper limits for the projected rotational velocity $v \sin i \leq 20$ km s^{-1}.

RESULTS OF OUR MEASUREMENTS

Since we found no published information on the photometric and spectroscopic variability for any of the eight stars, our magnetic-field measurements were performed at random rotation phases.

The results of our measurements are presented in Table 2. As an illustration, the figure shows portions of the spectra for the three stars with the strongest magnetic fields. The solid and dashed lines indicate the spectra in right- and left-hand circular polarizations, respectively. The observed shift (in Å) and the corresponding effective magnetic field B_e are shown. The Zeeman shift in the star HD 178892 with a strong magnetic field can be seen by eye. The effect is not so pronounced for stars with weaker fields. The figure shows only short parts of the spectra; actually, however, we measured the magnetic field by using a large number of spectral lines (about 50), which allows it to be measured with a sufficient accuracy (see Table 2).

For all of our program stars, we determined the projected rotational velocities $v \sin i$ by comparing their synthetic and observed spectra. To eliminate the effect of magnetic line broadening, whose contribution can be significant, preference should be given to a comparison of the observed and computed profiles for lines with a low sensitivity to a magnetic field. In our spectral range, it is most convenient to work with the Fe II λ4508 Å line, whose effective Lande factor is $z = 0.5$. We used the VALD database (Kupka *et al.* 1999) for line identifications. As was noted above, because of the insufficient spectral resolution, we were able to derive accurate values of $v \sin i$ only for three of the eight stars; for the remaining stars, we give the upper limit $v \sin i \leq 20$ km s^{-1}.

Below, we present the results of our measurements and comments for each of our program stars.

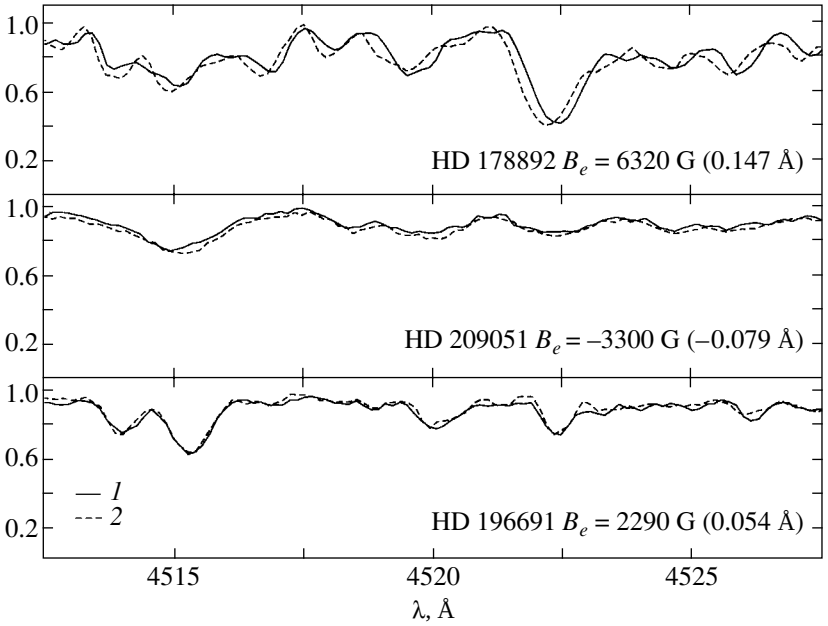

Zeeman shifts for the three stars with the strongest magnetic fields: the spectra in right-hand circular polarization (*1*) and left-hand circular polarization (*2*). The Zeeman shifts averaged over all lines (in Å) and the corresponding effective magnetic fields B_e are shown.

1. HD 29925. HD 29925 was first classified as a peculiar Si star by Bidelman and MacConnell (1973). Maitzen and Vogt (1983) found Δa for this star to be large, 0.48; for this reason, it was included in the list of objects for observations with the 1-m telescope. The λ5150 Å feature is prominent; the predicted maximum field strength B_e can be 3–4 kG.

The Zeeman spectra taken with the 6-m telescope show that the star has narrow and sharp lines. All of the four field measurements made over a year yielded B_e of negative polarity. Since our data are too scarce to plot the curve of longitudinal-field variations, it is difficult to predict B_e at maximum. There is no information on the photometric and spectroscopic variability. We determined the projected rotational velocity from the profile of the Fe II λ4508 Å line, $v \sin i = 23$ km s^{-1}.

2. HD 40711. This is an A0-type SrCrEu star. It was first classified as a peculiar star by Bidelman and MacConnell (1973). Maitzen and Vogt (1983) found $\Delta a = 0.43$, which was a strong reason for including the star in the list of candidates for observations.

The four Zeeman spectra that we obtained with the 6-m telescope indicate a longitudinal magnetic field of variable polarity. The spectrum contains many narrow and sharp lines, which makes it possible to perform highly accurate observations. Unfortunately, the observational data are too scarce to determine the rotation period. The low rotational velocity derived from the Fe II λ4508 Å, $v \sin i \leq 20$ km s^{-1}, only suggests that the star's rotation period is most likely longer than a week.

3. HD 115606. In the catalog of Renson *et al.* (1991), it is listed as an A2-type Sr star. However, previously, it was studied photoelectrically several times (see, e.g., Oja 1985) and showed no variability, and it is used as a photometric standard with the parameters $V = 8\overset{m}{.}547$, $B - V = 0\overset{m}{.}313$, and $U - B = 0\overset{m}{.}108$. In his list of effective temperatures, Glagolevskij (1994) gives $T_e = 10\,000$ for this star. Temperature calibrations based on Strömgren photometry give $T_e \sim 8200$.

The spectrum taken with the 1-m telescope shows that the λ5150 Å feature is strong, suggesting that a magnetic field with a longitudinal component of 3–4 kG at maximum can exist. For this reason, we included the star in our program of Zeeman observations with the 6-m telescope.

The star has numerous narrow and sharp lines. It has $v \sin i \leq 20$ km s^{-1}. Our Zeeman spectra taken at random rotation phases confirm that the star has a magnetic field. The B_e curve is alternating.

4. BD + 32°2827. It was first classified as a peculiar star by Bidelman (1985). Our low-resolution observations with the 1-m SAO telescope revealed a distinct feature, which suggests the existence of a magnetic field with a strength of 4–5 kG. The star's spectrum is rich in narrow and sharp lines,

and $v \sin i \leq 20$ km s^{-1}. Two of the three measured spectra suggest the existence of a magnetic field.

5. HD 168796. It was cataloged as a peculiar SiCrSr star by Bertaud (1965). Hauck and North (1982) found a large depression at λ5200 Å in this star from its measurements in the Geneva system. Therefore, we included this star in our program of observations with the 1-m telescope. Low-resolution spectroscopy revealed a feature in the depression profile indicative of a field with a strength of $\sim$5 kG.

We took four Zeeman spectra with the 6-m telescope; the presence of a magnetic field is beyond question. The lines in the star's spectrum are narrow and sharp and the projected rotational velocity is $v \sin i \leq 20$ km s^{-1}. The period of the B_e variations exceeds 4 days.

6. HD 178892. Bond (1970) found the star to be peculiar during objective-prism observations. In the SIMBAD database, it is listed as a star in a binary system.

Our observations with the 1-m telescope revealed a prominent feature at a wavelength near λ5150 Å. We were able to obtain four Zeeman spectra for this star. It possesses a strong magnetic field, whose longitudinal component is not less than 8 kG. At present, we know only one star (HD 215441) whose longitudinal component B_e exceeds this value and one star (HD 175362) with a comparable longitudinal component (see the catalog of Romanyuk (2000)). HD 215441 is a hot silicon star ($T_e = 16\,000$ K), while HD 175362 is a star with anomalous helium lines ($T_e = 17\,000$ K) (Glagolevskij 1994). Among the numerous and cooler (with T_e of the order of 8000 K) SrCrEu stars, HD 178892 can be a record holder with its magnetic field strength. Undoubtedly, its observations with the Zeeman analyzer attached to the 6-m telescope will be continued.

The star has numerous lines in its spectra. The projected rotational velocity is $v \sin i \leq 20$ km s^{-1}.

7. HD 196691. Bidelman (1981) found it to be a peculiar Si star during an objective-prism survey. Our observations with the 1-m telescope suggest the existence of a magnetic field with a strength of $\sim$4 kG.

All of the four measurements made over a year yielded a field of positive polarity; the star is probably nonreversible, although the period can be of the order of a week. The projected rotational velocity is $v \sin i = 20$–22 km s^{-1}.

8. HD 209051. Bidelman (1981) found the star to be peculiar. It has SrCrEu anomalies. Our observations with the 1-m telescope suggest that a magnetic field with a strength of about 4 kG can exist.

Our four Zeeman spectra taken over a year revealed a strong magnetic field of negative polarity. The

Table 2. The measured longitudinal magnetic-field components

JD 2450000+	t, min	S/N	$[n]$	$B_e \pm \sigma$, G
HD 29925 = BD + 00°830				
1807.508	30	100	60	-1100 ± 190
2129.543	30	80	40	-200 ± 360
2153.521	50	80	41	-810 ± 250
2189.458	40	180	46	-890 ± 150
HD 40711 = BD + 10°973				
1807.554	25	130	65	-230 ± 60
1892.538	15	60	68	330 ± 110
2130.553	15	50	50	-630 ± 310
2153.557	50	90	56	-650 ± 90
HD 115606 = BD + 13°2653				
1952.438	25	60	55	-210 ± 130
2333.454	30	100	62	680 ± 120
2333.479	30	100	65	640 ± 110
2417.254	30	90	63	-760 ± 150
BD + 32°2827				
2191.208	40	70	56	-770 ± 180
2417.341	60	100	45	-470 ± 150
2457.417	40	100	49	$+60 \pm 130$
HDE 168796 = BD + 13°3612				
2129.291	20	160	60	-610 ± 110
2130.291	20	190	60	-290 ± 110
2190.225	20	130	65	-870 ± 90
2458.396	20	90	59	510 ± 110
HD 178892 = BD + 14°3811				
2459.450	30	80	60	6320 ± 480
2459.473	30	70	58	6260 ± 530
2625.140	45	130	82	8150 ± 390
2626.139	30	110	92	8490 ± 380
HD 196691 = BD − 06°5545				
2130.304	30	140	45	1940 ± 240
2417.500	40	60	43	2290 ± 360
2454.473	30	70	47	1920 ± 240
2457.419	30	70	47	630 ± 250
HD 209051 = BD − 07°5683				
2130.456	30	140	25	-3300 ± 580
2191.258	30	120	31	-2580 ± 460
2454.498	30	70	26	-2980 ± 730
2458.420	40	50	18	-1040 ± 700

lines in the star's spectrum are significantly broadened by rotation ($v \sin i = 75$ km s^{-1}). Therefore, the field model in which the star is seen mainly from its negative pole and the rotation period is several days seems plausible.

CONCLUSIONS

We have completed the first stage of our search for new magnetic stars among the stars with large continuum depressions at λ5200 Å. We found phenomenological evidence suggesting the possible presence of a magnetic field: the unidentified feature at a wavelength of about λ5150 Å in the profile of this depression that is discernible in low-resolution spectra. Of the 15 preselected candidates with the most prominent feature, 14 were found to be real magnetic CP stars; the fifteenth star, HD 161321, is an SB2 Am star with both components represented in its spectrum, which needs a detailed study whose prime objective is to separate the binary components. The results of our Zeeman-spectrum reduction for this star will be published separately. Thus, we can assert that our criterion, the presence of a distinct feature at λ5150 Å in the continuum depression profile, is effective in searching for magnetic stars, at least among cool CP stars.

We intend to continue our searches for new magnetic stars based on our list of candidates. Particular attention will be given to observations of objects in clusters and groups of different ages. This is necessary for the observational test of various theories for the origin and evolution of stellar magnetism.

ACKNOWLEDGMENTS

We are grateful to G.A. Chuntonov for help in preparing for the observations and for taking part in them. We wish to thank the Large Telescope Committee of the Russian Academy of Sciences and the SAO administration for their continuous support of stellar magnetic-field studies with the 6-m telescope. This study was supported in part by the Russian Foundation for Basic Research, project nos. 00-02-16460 and 00-02-06138. We used the VALD and SIMBAD databases.

REFERENCES

1. C. Bertaud, J. Obs. **48**, 211 (1965).
2. W. P. Bidelman, Astron. J. **86**, 553 (1981).
3. W. P. Bidelman, Astron. J. **90**, 341 (1985).
4. W. P. Bidelman and D. J. MacConnell, Astron. J. **78**, 687 (1973).
5. H. E. Bond, Publ. Astron. Soc. Pac. **82**, 321 (1970).
6. G. A. Chountonov, *Stellar Magnetic Fields*, Ed. by Yu. V. Glagolevskij and I. I. Romanyuk (Moscow, 1997), p. 239.
7. N. Cramer and A. Maeder, Astron. Astrophys. Suppl. Ser. **41**, 111 (1980).
8. V. G. El'kin, D. O. Kudryavtsev, and I. I. Romanyuk, Pis'ma Astron. Zh. **28**, 171 (2002) [Astron. Lett. **28**, 169 (2002)]
9. Yu. V. Glagolevskij, Bull. Spets. Astrofiz. Obs. **38**, 152 (1994).
10. B. Hauck and P. North, Astron. Astrophys. **114**, 23 (1982).
11. D. O. Kudryavtsev, Balt. Astron. **9**, 649 (2000).
12. F. Kupka, N. Piskunov, T. A. Ryabchikova, *et al.*, Astron. Astrophys. Suppl. Ser. **138**, 119 (1999).
13. H. M. Maitzen, Astron. Astrophys. **51**, 223 (1976).
14. H. M. Maitzen and N. Vogt, Astron. Astrophys. **123**, 48 (1983).
15. I. D. Naĭdenov and G. A. Chuntov, Soobshch. Spets. Astrofiz. Obs. **16**, 63 (1976).
16. T. Oja, Astron. Astrophys. Suppl. Ser. **61**, 331 (1985).
17. V. E. Panchuk, Preprint SAO No. 154 (Special Astrophysical Observatory, Nizhnii Arkhyz, 2001).
18. P. Renson, R. Farragiana, and F. Catalano, Astron. Astrophys. Suppl. Ser. **89**, 429 (1991).
19. I. I. Romanyuk, *Magnetic Fields of CP and Related Stars*, Ed. by Yu. V. Gladolevskij and I. I. Romanyuk (Moscow, 2000), p. 18.
20. I. I. Romanyuk, V. G. Elkin, D. O. Kudryavtsev, and J. D. Landstreet, Bull. Spets. Astrofiz. Obs. **45**, 93 (1998).

Translated by N. Samus'

Astronomy Letters, Vol. 29, No. 6, 2003, pp. 405–408. Translated from Pis'ma v Astronomicheskiĭ Zhurnal, Vol. 29, No. 6, 2003, pp. 461–464.

Detection of Lithium in the Spectrum of the Symbiotic Mira Star V407 Cygni

A. A. Tatarnikova[1], P. M. Marrese[2], U. Munari[2], T. Tomov[3], and B. F. Yudin[1]*

[1] *Sternberg Astronomical Institute, Universitetskii pr. 13, Moscow, 119992 Russia*

[2] *Padua Astronomical Observatory, via dell'Osservatorio, Asiago (Vicenza), I-36012 Italy*

[3] *Astro-Space Center, Copernicus University, ul. Gagarina 11, Torun, 87-100 Poland*

Received December 11, 2002

Abstract—We detected the resonance lithium doublet, ^{7}LiI λ6708, in the spectra of the symbiotic Mira V407 Cyg ($P \approx 763^d$) obtained with a resolution $R = \lambda/\Delta\lambda \approx 18\,500$. The line equivalent width is $\sim$0.34 Å. The presence of lithium in the atmosphere of the Mira, which, judging by its period, appreciably ascended the asymptotic giant branch (AGB), can be explained by the penetration of its convective envelope into the hot-bottom-burning (HBB) hydrogen-shell source. At the same time, the spectrum of V407 Cyg does not reveal the ZrO λ5551, 6474 absorption bands, which are used to classify S-type stars from low-resolution spectra. We found only weak ZrO λ5718, 6412 bands, which are, however, invisible in low-resolution spectra. Thus, the Mira star V407 Cyg should be classified as being of the spectral type M. In general, the spectrum of V407 Cyg is similar to the spectrum of the red giant in the symbiotic star CH Cyg, but the latter exhibits no lithium lines. The switch-on of the HBB process without any significant enrichment of the atmosphere of an AGB star with *s*-process elements implies that the third dredge-up is not efficient for some of these stars. © *2003 MAIK "Nauka/Interperiodica"*.

Key words: *symbiotic stars, spectroscopic studies, lithium.*

INTRODUCTION

Lithium is one of the key elements related stellar evolution and nucleosynthesis. An unusually intense ^{7}Li I λ6708 Å line (the resonance doublet) was first detected in the spectrum of the carbon star WZ Cas (McKellar 1940). The red asymptotic-giant-branch (AGB) stars, to which WZ Cas belongs, are currently believed to be among the major suppliers of lithium in the Galaxy (Travaglio *et al.* (2001) and references therein). An additional amount of ^{7}Li appears in the atmosphere of a red giant when the bottom of its convective envelope reaches the hydrogen burning shell and penetrates it (hot bottom burning or HBB for short) as it evolves along the AGB.

Since the nuclear reactions proceed already at the bottom of the convective envelope, the nucleosynthesis products can be dredged up into the outer, cooler atmospheric layers in a short time. These products include ^{7}Be produced in the ^{3}He(^{4}He, γ)^{7}Be reaction at a temperature exceeding $\sim 2 \times 10^7$ K. In the outer layers, ^{7}Be captures a free electron to form ^{7}Li. The latter can avoid the subsequent rapid destruction in a reaction with a proton because of the low temperature ($< 3 \times 10^6$ K). This mechanism of lithium formation in the atmospheres of AGB stars was suggested by Cameron and Fowler (1971).

Detailed computations of the stellar evolution show that stars with initial masses of 4–6 $M_\odot$ pass through the HBB stage. Their absolute bolometric magnitudes during the formation of lithium range from $M_{bol} \approx -6$ to $M_{bol} \approx -7$. A high lithium abundance is maintained for 10^4–10^5 years. Its maximum value can reach $\log \varepsilon(^7\mathrm{Li}) \approx 4.5$ (Sackmann and Boothroyd 1992). The current cosmic lithium abundance, in particular, in meteorites, is $\log \varepsilon(^7\mathrm{Li}) \approx 3.3$.

Four superlithium AGB stars whose atmospheric lithium abundances appreciably exceed the cosmic value are known in the Galaxy to date: WZ Cas, WX Cyg, IY Hya, and T Sgr (Abia *et al.* 1991; Abia and Isern 2000). The first three of them are carbon stars, while T Sgr is classified as an S-type star. Thirty-five red giants with a lithium line in their spectra ($\log \varepsilon(^7\mathrm{Li}) = 1$–$4$) were detected in the LMC and the SMC. Twenty-six and six of them belong to S-type and carbon stars, respectively (Smith *et al.* 1995). The intensity of the lithium line decreases as one passes to later spectral types for normal giants (Merchant 1967), and it virtually disappears

*E-mail: yudin@sai.msu.ru

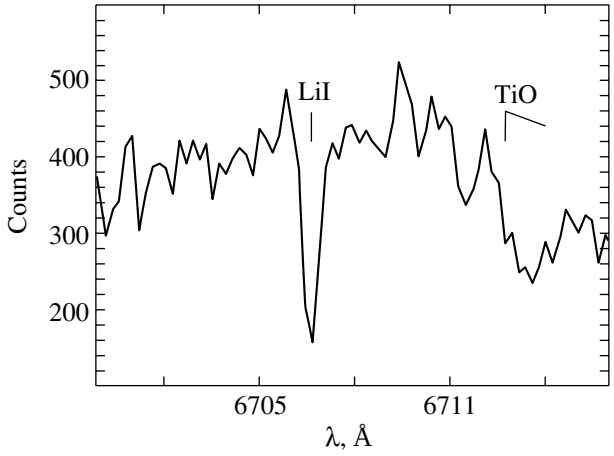

Fig. 1. A portion of the spectrum for V407 Cyg near the Li I λ6708 line. This spectrum was taken on July 30, 1997.

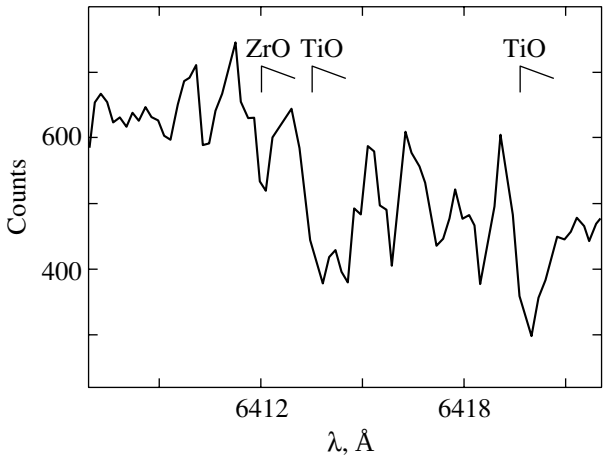

Fig. 2. A portion of the spectrum for V407 Cyg near the ZrO absorption band. This spectrum was taken on July 30, 1997.

for late M-type red giants. The observations of Boesgaard (1970) revealed no "lithium" stars among the MS-type red giants. Thus, the stellar atmosphere seemed to be enriched with lithium when it was significantly enriched with *s*-process elements during the third dredge-up. However, having detected the lithium line in the spectra of several red giants with a photometric variability characteristic of Mira stars, Garcia-Lario *et al.* 1999) found neither the ZrO λ6470 band nor the lines of *s*-process elements in the spectral range 7400–7600 Å.

In this paper, we report on the detection of the ^{7}Li I λ6707 doublet in the spectrum of the symbiotic Mira V407 Cyg. Among the known symbiotic Mira stars, V407 Cyg has the longest pulsation period of its cool component (Mira), $P \approx 763^{\rm d}$. This means that the red giant of the symbiotic binary V407 Cyg has appreciably advanced along the AGB. The pulsation amplitude in the K and B spectral bands is $\sim 0\overset{m}{.}9$ and at least $3\overset{m}{.}5$, respectively. In addition to periodic variations, the Mira's brightness undergoes noticeable irregular variations. The Mira is classified by the intensity of the TiO λ7055 band as M6–M7. Its spectrum also exhibits VO bands. Thus, the cool component of V407 Cyg belongs to the group of oxygen Mira stars (Kolotilov *et al.* 1998).

THE DETECTION OF Li I

The high-resolution ($R = \lambda/\Delta\lambda \approx 18\,500$) spectra of V407 Cyg in which we detected the resonance Li I λ6707.76, 6707.91 doublet were obtained with an echelle spectrograph mounted at the Cassegrain focus of the 1.82-m telescope at the Padua and Asiago astronomical observatories (Asiago, Italy). The spectral range of the spectrograph is 4500–9000 Å. However, the observations of V407 Cyg were often carried out in a narrower spectral range that did not include the lithium line. Figure 1 shows a portion of the spectrum near the lithium line. This spectrum was taken on July 30, 1997, when the hot component was in the "off" state. The equivalent width of the Hα line was only ~3 Å. The star was classified by the intensity of the TiO λ5448, 7125 bands as M6–M7. Thus, we can say that at least in this spectral range, the cool component dominated the radiation from V407 Cyg. On other dates, the hot component was in an active state, which was reflected in a decrease of the lithium-line equivalent width. However, we cannot completely rule out the intrinsic variability of this line in the Mira's atmosphere, say, with its brightness phase.

Among the late-type red giants, R CMi, SU Mon, R Cyg, and HR 8714 exhibit approximately the same equivalent widths of the lithium line (Boesgaard 1970). They are all S-type stars. At the same time, the ratio of the equivalent widths of the lithium line and the Ca I λ6573 line for V407 Cyg is slightly higher than that for the above stars. This may be indicative of a higher lithium abundance in the atmosphere of V407 Cyg. The equivalent widths of the lithium and calcium lines in the spectrum of V407 Cyg are ~0.34 and ~0.17 Å, respectively. In the LMC, for example, the S-type star HV 5584 exhibits such an equivalent width of the lithium line. Its effective temperature is ~3200 K; i.e., it roughly corresponds to the spectral type M6, and the lithium abundance in its atmosphere is $\log \varepsilon(^7\mathrm{Li}) \approx 2.8$ (Smith *et al.* 1995). We found no ZrO molecular bands at wavelengths of 6474 and 5751 Å. These bands are used to classify S-type stars from low-

resolution spectra (Keenan 1954). Their absence implies that the Mira V407 Cyg is not an S-type star. Note that, in the absence of the ZrO λ6474 band, the nearby TiO λ6479 band appears intense, so it is clearly seen in low-resolution spectra. It is this band rather than the ZrO band that we observe in these spectra. Based on low-resolution spectra alone, we cannot determine which molecule is responsible for this absorption, because the wavelength difference between these two bands is small.

Jurdana-Sepic and Kotnik-Karuza (2002) found weak ZrO λ5718, 6412 bands in the absence of the ZrO λ5551, 6474 bands in the high-resolution spectrum of the symbiotic star CH Cyg, whose red giant is classified as M7. The spectrum of V407 Cyg also exhibits shallow absorption features at wavelengths of 5718 and 6412 Å (Fig. 2), which, following the example of the above authors, we can attribute to the ZrO molecular bands. In the green part of the spectrum for CH Cyg, Jurdana-Sepic and Kotnic-Karuza (2002) detected lines of rare-earth elements, in particular, the Ba II λ4334 and La II λ4827 lines. These lines are also present in the spectrum of V407 Cyg. In other words, there is a close similarity between the spectra for the cool components of the symbiotic stars V407 Cyg and CH Cyg, which also belong to the same spectral type. However, the spectrum of CH Cyg exhibits no lithium lines; i.e., its red giant has not yet reached the HBB stage. We estimated its maximum bolometric magnitude (the giant shows appreciable brightness variations) to be $M_{\rm bol} \approx -4.8$. It falls outside the range in which the HBB stage begins in simulations. The distance to CH Cyg was determined from its parallax estimate. Such an estimate is not available for V407 Cyg. In addition, if the Mira is at the HBB stage, then its luminosity can no longer be estimated from the period–luminosity (P, L) relation.

In their lithium stars, Garcia-Lario *et al.* (1999) found neither the ZrO λ6474 band nor lines of s-process elements in the spectral range 7400–7600 Å, which is free from TiO molecular bands. Such lines, in particular, Zr I λ7440 and Nd II λ7514, are present in the spectrum of V407 Cyg in this spectral range. Only one star in the list of lithium stars by Garcia-Lario *et al.* (1999) has a period longer than 700 days (its name is not given), although they attempted to study 14 such long-period giants. However, 13 of them could not be detected because of the presence of thick dust envelopes around these stars, which greatly reduce their brightness. The dust envelope of V407 Cyg is optically thin (Kolotilov *et al.* 1998), probably because of the influence of the hot component.

Thus, we found the first symbiotic Mira star whose cool component exhibits a strong (for late-type red giants) Li I λ6708 line in its spectrum. The Mira star V407 Cyg is the second discovered long-period ($P > 700^{\rm d}$) red giant with the lithium line. Judging by the equivalent width of this line in the spectrum of V407 Cyg, the lithium abundance in the atmosphere of this Mira may be considered to be moderate. The preferred mechanism of lithium formation is the HBB process. According to simulations, this process switches on only in sufficiently massive stars during their formation ($M = 4$–$6M_\odot$), whose bolometric magnitudes on the AGB ranges from $M_{\rm bol} \approx -6$ to $M_{\rm bol} \approx -7$ (Sackmann and Boothroyd 1992). The exact lower limit of the mass depends on the metallicity in the stellar atmosphere. At the same time, if the star passes through the HBB stage, the maximum lithium abundance in its atmosphere ($\log \varepsilon(^7{\rm Li}) \approx 4$) does not depend on its initial mass and metallicity (Travaglio *et al.* 2001). Superlithium stars, for which the lithium-line equivalent width is several Å (Abia *et al.* 1991; Abia and Isern 2000), i.e., an order of magnitude larger than the equivalent width of the lithium line in the spectrum of V407 Cyg, exhibit such a lithium abundance. Therefore, either the HBB process in V407 Cyg has just begun or it has already finished, and lithium is destroyed in a reaction with a proton. In the latter case, however, the Mira probably should have been an S-type red giant, which it is not.

If, as is customary, the red giant is classified from low-resolution spectra, then the Mira V407 Cyg should be attributed to M-type stars, because its ZrO bands are invisible in these spectra. At the same time, several weak ZrO molecular bands can still be detected in its high-resolution spectra. The spectrum for the Mira star V407 Cyg is similar to the spectrum for the red giant of the symbiotic star CH Cyg, which, however, is not a lithium star. Thus, the HBB can switch on when the red giant's atmosphere has not yet been significantly enriched with s-process elements, which appear in the star during the third dredge-up. For some reasons, the third dredge-up is inefficient in some stars like the Mira V407 Cyg.

ACKNOWLEDGMENTS

This study was supported by the Russian Foundation for Basic Research (project no. 02-02-16235) and the KBN grant no. 5 P03D 003 20 (Polish Research Committee).

REFERENCES

1. C. Abia and J. Isern, Astrophys. J. **536**, 438 (2000).
2. C. Abia, H. M. Boffin, J. Isern, and R. Rebolo, Astron. Astrophys. **245**, L1 (1991).
3. A. M. Boesgaard, Astrophys. J. **161**, 1003 (1970).
4. A. G. B. Cameron and W. A. Fowler, Astrophys. J. **164**, 111 (1971).

5. C. A. Frost, R. C. Cannon, J. C. Lattanzio, *et al.*, Astron. Astrophys. **332**, L17 (1998).
6. P. Garcia-Lario, F. D'Antona, J. Lub, *et al.*, *Proceedings of 191th Symp. of the IAU: Asymptotic Giant Branch Stars,* Ed. by T. Le Bertre, A. Lebre, and C. Waelkens (Chelsea, 1999), p. 91.
7. R. Jurdana-Sepic and D. Kotnik-Karuza, private communication (2002).
8. P. C. Keenan, Astrophys. J. **120**, 484 (1954).
9. A. McKellar, Publ. Astron. Soc. Pacific **52**, 407 (1940).
10. A. E. Merchant, Astrophys. J. **147**, 587 (1967).
11. I. J. Sackmann and A. I. Boothroyd, Astrophys. J. **392**, L71 (1992).
12. V. V. Smith, B. Plez, and D. L. Lambert, Astrophys. J. **441**, 735 (1995).
13. C. Travaglio, S. Randich, G. Daniele, *et al.*, Astrophys. J. **559**, 909 (2001).

Translated by N. Samus'

Astronomy Letters, Vol. 29, No. 6, 2003, pp. 409–415. Translated from Pis'ma v Astronomicheskiĭ Zhurnal, Vol. 29, No. 6, 2003, pp. 465–472.

The Role of Collisions in the Particle Acceleration in Solar-Flare Magnetic Traps

V. A. Kovalev[1]* and B. V. Somov[2]

[1]*Institute of Terrestrial Magnetism, Ionosphere, and Radiowave Propagation, Russian Academy of Sciences, Troitsk, Moscow oblast, 142190 Russia*

[2]*Sternberg Astronomical Institute, Universitetskii pr. 13, Moscow, 119992 Russia*

Received November 15, 2002

Abstract—We investigate the particle acceleration in a magnetic trap with converging mirrors, which is a constituent part of the magnetic reconnection mechanism in solar flares. We take into account the effect of Coulomb collisions on the formation of the accelerated-electron distribution function. The solution of the kinetic equation shows that the Coulomb scattering of anisotropic accelerated electrons leads to their isotropization. As a result, the fraction of trapped particles increases and the acceleration efficiency significantly rises. © *2003 MAIK "Nauka/Interperiodica".*

Key words: *solar flares, magnetic fields, particle acceleration, Coulomb collisions.*

INTRODUCTION

Collapsing magnetic traps are an integral part of the mechanism of three-dimensional collisionless magnetic reconnection in the solar corona (Somov and Kosugi 1997; McKenzie and Hudson 1999). Hard X-ray observations of solar flares with high spatial and temporal resolutions using the X-ray telescopes onboard the Yohkoh and RHESSI satellites suggest that reconnecting high-temperature turbulent current sheets are the primary sources of flare energy (Somov *et al.* 1999, 2002). Here, magnetic energy rapidly transforms into other forms: plasma heating to anomalously high temperatures ($T_{(e)} \gtrsim 100$ MK), plasma acceleration to super-Alfvén velocities, and electron and ion acceleration by an electric field.

Reconnected field lines, together with heated plasma, flow out of the current sheet at a super-Alfvén velocity and produce traps with rapidly decreasing lengths in the corona above the photospheric magnetic-field sources. If the conservation conditions for the longitudinal adiabatic invariant, which were considered for solar flares by Somov and Kosugi (1997) and Somov (2000), are satisfied, then the longitudinal (parallel to the magnetic field) particle momentum and, hence, energy rapidly increase. Thus, dynamic magnetic traps with converging mirrors can be among the sources of high-energy particles in solar flares. As Somov and Kosugi (1997) and Bogachev and Somov (1999) showed, the efficiency of this acceleration process in the collisionless approximation is high in solar flares. This is because the process under consideration is basically the first-order acceleration mechanism of Fermi (1954).

A comparative analysis of the various acceleration mechanisms in solar flares based on currently available observations and theoretical concepts can be found, for example, in the monograph of Aschwanden (2002). The acceleration in collapsing magnetic traps can successfully perform the role of the second stage in two-stage particle acceleration to high energies (Somov and Kosugi 1997). In this case, however, it is important to strictly determine the validity range of the model by taking into account the many effects that affect the actual particle acceleration efficiency in flares.

Previously (Kovalev and Somov 2002), we calculated the acceleration by taking into account the electric potential that arises between the plasma in a trap and the magnetic mirrors because of the difference in the behaviors of electrons and ions. We showed that, for a positive electric potential (the result of faster electron escape), the confinement and acceleration efficiencies increase for electrons and decrease for ions. This effect is sensitive to anisotropy in the initial particle distribution (Kovalev and Somov 2003). Coulomb collisions, even rare ones, can also significantly affect the particle acceleration efficiency in magnetic traps. An analysis of this phenomenon is the subject of our work.

The role of Coulomb collisions in the so-called open traps with stationary magnetic mirrors under

*E-mail: vkovalev@izmiran.troitsk.ru

laboratory conditions was first considered by Budker (1958). Such magnetic traps are known to have a high allowable ratio of the plasma pressure to the magnetic pressure (β) and to be stable against rough hydrodynamic perturbations. As applied to solar flares, this implies that a large number of electrons and ions can be accelerated without fearing that the collapsing traps will be destroyed even at the initial acceleration stage. In this case, the classical escape of particles from a magnetic trap caused by Coulomb scattering into the loss cone can actually be of fundamental importance. In contrast to the anomalous escape attributable to the particle–wave interaction, the classical escape is always present and, thus, determines the minimum level of possible plasma losses from the trap (Pastukhov 1984). In addition, Coulomb collisions tend to bring the particle distribution function to an equilibrium state, which generally restricts the class of possible kinetic instabilities. The effect of the nonuniformity of the magnetic field of a trap on the kinetics of energetic electrons was studied by Kovalev and Korolev (1981).

In general, allowing for Coulomb collisions is a complex mathematical problem that reduces to numerically solving a system of equations for various plasma components. Here, apart from the general formulation, we consider some of the particular aspects of this problem related to elucidating the effect of Coulomb scattering on the electron acceleration. Simplifying the problem, we use the perturbation method, with the solution of the problem without Coulomb collisions in the adiabatic approximation being taken as the initial approximation. The perturbation method suggests that the sought-for correction is small. In other words, Coulomb collisions must be sufficiently rare: the time between successive collisions must be much longer than the time of flight of particles between the magnetic mirrors in the trap.

CHARGED PARTICLES IN A MAGNETIC TRAP

In the simplest model of a magnetic mirror trap (the so-called long trap with short mirrors), the magnetic field, being uniform in the largest part of it, sharply increases from B_1 to B_2 in the magnetic mirrors. The quantity B_2/B_1 is called the mirror ratio. If a super-Alfvén flow of heated plasma with a frozen-in magnetic field generates a shock wave near a reconnecting current sheet (Somov and Kosugi 1997), then the mirror ratio strongly depends on the cooling regime of the postshock compressed plasma (Bogachev *et al.* 1998). In the case of slow reconnection without a shock, the mirror ratio is determined by the geometry of the magnetic field or, to be more precise, by the increase in magnetic-field strength as its photospheric sources are approached.

Let the length L of a collapsing magnetic trap with mirrors moving at velocity v_m vary as

$$l(t) = L(t)/L_\mathrm{o} = 1 - t/t_\mathrm{o}. \quad (1)$$

Here, L_o is the initial trap length at $t = 0$ and t_o is the collapse time, which is defined as the time at which the top of the trap passes through the shock front (for more detail, see Somov and Kosugi 1997; Somov 2000):

$$t_\mathrm{o} = \frac{L_\mathrm{o}}{2v_m}. \quad (2)$$

In formula (1), we assumed the mirror velocity to be constant.

In the absence of Coulomb collisions and at a sufficiently high particle velocity, the first or transverse adiabatic invariant takes place:

$$v_\perp^2/B = \mathrm{const}.$$

As a result, when a particle moves into the region of a stronger field, i.e., into the magnetic mirror, the velocity component transverse to the magnetic-field direction increases. In the long-trap approximation, the transverse velocity can be assumed to be conserved everywhere inside the trap except, of course, the mirrors themselves:

$$v_\perp = \mathrm{const}.$$

The longitudinal velocity $v_{||}$ increases during each particle reflection from the magnetic mirrors that move at velocity v_m:

$$\frac{dv_{||}}{dt} = 2v_m\frac{d\mathcal{N}}{dt} \simeq 2v_m\frac{v_{||}}{L}$$

or

$$v_{||} = v_{||\mathrm{o}} + 2v_m\mathcal{N},$$

where $\mathcal{N}$ is the number of successive particle reflections from the magnetic mirrors. If this number is large and if the longitudinal particle velocity is high compared to the mirror velocity, then the second or longitudinal adiabatic invariant is conserved. In the long-trap approximation, this invariant can be written as

$$v_{||}l = \mathrm{const}. \quad (3)$$

In a collapsing magnetic trap, the so-called transit particles escape from the trap as the longitudinal velocity increases. The velocities of these particles satisfy the particle-charge-independent relation

$$v_{||} + v_m \geq v_{\perp\mathrm{o}}R, \quad (4)$$

where we introduced the dimensionless parameter

$$R = (B_2/B_1 - 1)^{1/2}.$$

In the presence of Coulomb collisions, the adiabatic invariants are not conserved. If, however, the collisions are sufficiently rare, then their effect is determined by a small correction to the collisionless solution. In the opposite case of frequent collisions, heating rather than acceleration takes place in a collapsing magnetic trap.

As was noted in the Introduction, the criterion of allowance for Coulomb collisions is determined by the ratio of the time of flight of a chosen particle (in our case, an electron), which is commonly called a test particle, in the trap between the mirrors $\tau = L/v_{||}$ to the time scale of its collisions with other (field) plasma particles (electrons and ions) τ_s inside the trap:

$$\tau_s = \frac{\sqrt{m_e}\,T^{3/2}}{\sqrt{2}\pi n e^4 \Lambda}. \quad (5)$$

The effect of collisions may be ignored if $\tau \ll \tau_s$ or

$$v_{o||} \gg L_o l^2/\tau_s. \quad (6)$$

Let us obtain the corresponding estimates for a completely ionized plasma inside a magnetic trap with a particle density $n \approx 2 \times 10^9$ cm^{-3} and temperature 10^8 K. The Coulomb logarithm

$$\Lambda = \ln\left(10^4 \frac{T^{2/3}}{n^{1/3}}\right) \quad (7)$$

is $\simeq 15$. The Coulomb collision time scale is then $\tau_s \simeq 8$ s. The time of flight of the thermal electrons in a magnetic trap with a length $L_o \approx 2 \times 10^9$ cm is 0.4 s. The plasma with a temperature $T_e \gtrsim 30$–40 MK in solar flares is commonly called *superhot*. It is observed with telescopes in hard X-rays and, in general, is located above the cooler and denser loops observed in soft X-rays, as shown in the figure.

The above estimates indicate that, to a first approximation, the superhot plasma injected from a high-temperature turbulent current sheet (for more detail, see Somov and Kosugi 1997) can be considered to be collisionless with respect to the acceleration in a collapsing magnetic trap. However, the collisions cannot be completely ignored, because condition (6) is satisfied without a comfortable margin.

As regards the ions, they are known to be scattered a factor of approximately $\sqrt{m_i/m_e}$ more slowly than electrons with the same energy. To remain quasi-neutral on the large scale L, the superhot plasma inside the trap acquires a positive potential relative to the ends (magnetic mirrors). In this case, the region of adiabatic electron confinement in velocity space has the shape of a two-sheet hyperboloid (Kovalev and Somov 2003):

$$v_{o||}^2 \le l^2\left(v_{o\perp}^2 R^2 + 2e\varphi/m_e\right),$$

where φ is the electric potential.

An electric field selectively acts on particles with different electric charges. It hampers the escape of electrons from the trap. The slowest electrons whose energy is too low to overcome the potential barrier remain trapped. For traps with stationary mirrors, this phenomenon was considered for solar flares by Spicer and Emslie (1988). To consider the effect of Coulomb collisions in pure form, below we disregard the electric field. Moreover, below we take into account the effect of Coulomb collisions only on the accelerated electrons.

A KINETIC DESCRIPTION

The Collisionless Solution

We use the collisionless solution obtained by Bogachev and Somov (1999) for the initial Maxwellian distribution of a superhot plasma:

$$f(\mathbf{v}, l) = A(l)\Theta\left(Rv_\perp - v_{||}\right)\exp\left(-\frac{v_{||}^2 l^2}{V_T^2} - \frac{v_\perp^2}{V_T^2}\right), \quad (8)$$

where

$$A(l) = \frac{\sqrt{1 + R^2 l^2}}{\pi^{3/2} V_T^3 R}.$$

We rewrite this solution as

$$f(x, \mu, l) = A(l)\Theta\left(\mu_{cr} - \mu\right) e^{-x^2} e^{x^2\mu^2(1-l^2)}, \quad (9)$$

where

$$\mu = \cos\theta, \quad \mu_{cr} = \left(1 - \frac{B_1}{B_2}\right)^{1/2},$$

$$x = \frac{v}{V_T}, \quad V_T = \sqrt{\frac{2k_B T}{m_e}},$$

θ is the pitch angle, Θ is the step function:

$$\Theta(x) = \begin{cases} 1, x > 0 \\ 0, x < 0. \end{cases}$$

When the following condition is satisfied:

$$x^2\mu^2\left(1 - l^2\right) \ll 1,$$

which is valid at the initial trap compression stage, solution (9) can be represented as the sum of a quasi-isotropic Maxwellian function and an anisotropic addition:

$$f(x, \mu, l) = A(l)e^{-x^2}[1 + x^2\left(1 - l^2\right)\mu^2]\Theta(\mu_{cr} - \mu). \quad (10)$$

Naturally, the solution of the collisional problem in the limiting case $\tau_s^{-1} = 0$ must transform into (10).

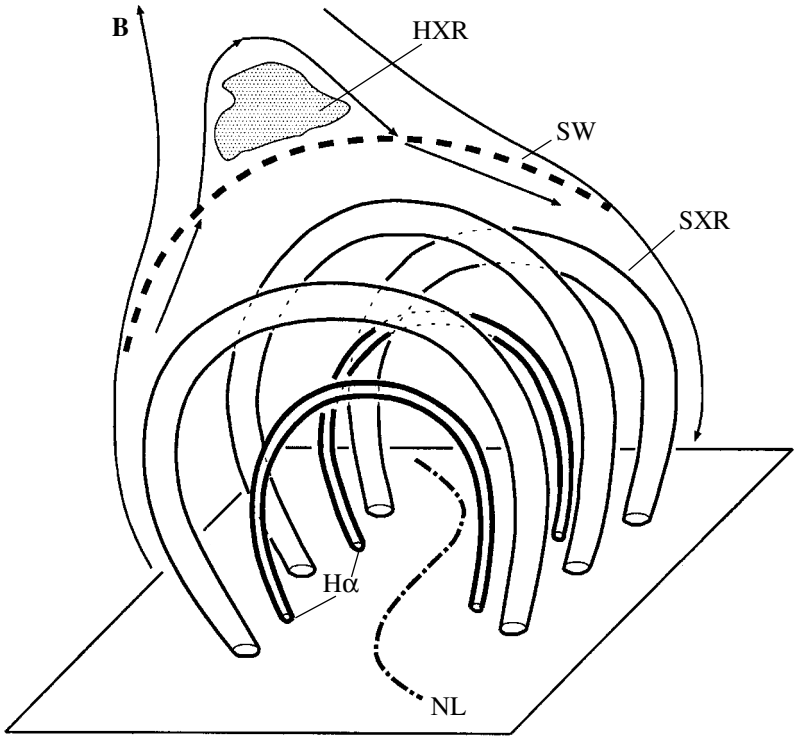

The two-level structure of coronal loops in a flare (Somov 2000): Hα is the loops observed in the Hα line with ground-based optical telescopes; SXR is the arcade of loops observed in soft X-rays onboard satellites; SW is the presumed location of the shock front; HXR is the coronal hard X-ray source also observed with satellite telescopes; NL is the line of magnetic-field polarity reversal in the photosphere (neutral line); and **B** is coronal magnetic field lines.

The Collision Integral

We will use the collision operator $St[f_\alpha]$ in the form (Rosenbluthe *et al.* 1957; Trubnikov 1958)

$$St[f_\alpha] = 2\pi \sum_\beta \Lambda^{\alpha/\beta} \frac{e^4}{m_\alpha^2} \frac{\partial}{\partial v_j} \times \left(\frac{\partial^2 g_\beta}{\partial v_j \partial v_k} \frac{\partial f_\alpha}{\partial v_k} - 2\frac{m_\alpha}{m_\beta} f_\alpha \frac{\partial h_\beta}{\partial v_j} \right). \quad (11)$$

Here, the indices α and β refer to the types of test and field particles, respectively. The indices j and k take on values of 1, 2, and 3. The first and second terms on the right-hand side of (11) describe the diffusion and dynamic friction in velocity space, respectively.

The functions

$$g_\beta = \int |v - v'| f_\beta(v') dv', \quad h_\beta = \int \frac{f_\beta(v')}{|v - v'|} dv',$$

which are related by

$$\Delta_v g_\beta = 2h_\beta, \quad \Delta_v h_\beta = -4\pi f_\beta,$$

where Δ_v is the Laplacian in velocity space, are called the Rosenbluthe–Trubnikov potentials.

The problem on the evolution of the distribution function in six-dimensional phase space in the rare-collision approximation generally reduces to the problem about the evolution of the distribution function f in the space of two variables, $v_\perp$ and $v_{||}$. In the presence of Coulomb collisions, the small-angle scattering dominates and the evolution of f is diffusion spreading (Trubnikov 1963).

The Kinetic Equation for Electrons

During collisions with ions, electrons change their direction but conserve their energy. In contrast, collisions with electrons result in both scattering and energy transfer. Using formula (11) with $\Lambda^{\alpha/\beta} \simeq \Lambda$ and $\alpha = \beta$ for electrons, we obtain a collision integral in the form

$$St[f] = 2\pi\Lambda \frac{e^4}{m^2} \times \left[\frac{\partial}{\partial v_j} \left(\frac{\partial^2 g}{\partial v_j \partial v_k} \frac{\partial f}{\partial v_k} \right) - \frac{\partial f}{\partial v_j} \frac{\partial}{\partial v_j} (\Delta_v g) + 8\pi f^2 \right]. \quad (12)$$

Thus, to determine the distribution function of the electrons in a collapsing magnetic trap, we must generally solve a complex integro-differential equation with the nonlinear right-hand side (12). However, as applied to solar-flare conditions, some simplifications

are possible. Using the expression for the divergence in velocity space in a spherical coordinate system with the axis directed along the velocity vector, we derive the equation (Pastukhov 1984)

$$\frac{\tau_s}{n}\frac{\partial(nF)}{\partial t} = 4\pi F^2 + \frac{1}{2}\frac{\partial^2 G}{\partial x^2}\frac{\partial^2 F}{\partial x^2} + \frac{1}{x^2}\frac{\partial G}{\partial x}\frac{\partial F}{\partial x} + \frac{1}{2x^3}\frac{\partial G}{\partial x}\frac{\partial}{\partial \mu}\left(1-\mu^2\right)\frac{\partial F}{\partial \mu}, \quad (13)$$

where

$$F = V_T^3 f/n, \quad G = g/nV_T.$$

The commonly used simplification that is justly associated with the diffusion approximation is that the coefficient G is calculated from a specified, in particular, Maxwellian distribution (Trubnikov 1963; Sivukhin 1964):

$$G = \left(x + \frac{1}{2x}\right)\mathrm{erf}(x) + \frac{1}{\sqrt{\pi}}e^{-x^2}, \quad (14)$$

where

$$\mathrm{erf}(x) = \frac{2}{\sqrt{\pi}}\int_0^x e^{-\xi^2}d\xi.$$

In the latter case, we obtain an equation that can be applied to states that are not too different from a thermodynamic equilibrium. To be more precise, in the approximation under consideration, we assume that all of the trapped electrons can be divided into two groups: (i) main-group electrons with an almost Maxwellian distribution function and (ii) fast electrons. If the density of the latter is low compared to the density of the main-group electrons, then the scattering by fast electrons can be disregarded. It will suffice to take into account the scattering of fast electrons by main-group electrons and ions.

In the high-velocity limit $x \gg 1$ (in practice, for $x > 2$), Eq. (13) for exponentially decreasing electron distribution functions takes the form

$$\frac{\tau_s}{n}\frac{\partial(nF)}{\partial t} = \frac{1}{x^2}\frac{\partial}{\partial x}\left(F + \frac{1}{2x}\frac{\partial F}{\partial x}\right) + \frac{1}{x^3}\frac{\partial}{\partial \mu}\left(1-\mu^2\right)\frac{\partial F}{\partial \mu}. \quad (15)$$

For magnetic traps with stationary mirrors, Pastukhov (1984) solved Eq. (15) by taking into account the small parameter that corresponded to the ratio of the electron and ion collision times. In the zero approximation in this parameter, the function F must satisfy the steady-state equation with the solution that shows that the Coulomb losses increase with decreasing μ, i.e., with increasing pitch angle. Note that, strictly speaking, the latter equation can be used for distribution functions that do not differ greatly from the Maxwellian function, because the corresponding potentials were used to derive it.

In our case of collapsing magnetic traps, the acceleration of all superhot plasma particles can be significant in the solar corona. The distribution is close to an equilibrium one only at the initial trap compression stage, i.e., for $1 - l \ll 1$. To obtain a solution during the entire stage of decrease in the trap length, when the distribution becomes highly anisotropic, we must use an exact expression for the Rosenbluthe–Trubnikov potential g_β.

For the initial trap compression stage ($l > 0.9$), the longitudinal temperature of the accelerated electrons is $T_{||} = T_{||o}/l^2 < 2 \times 10^8$ K. Therefore, using the nonrelativistic approximation for most electrons is justifiable. However, the electrons soon become relativistic (Bogachev and Somov 2001), which complicates the problem only slightly.

Evolution of the Angular Electron Distribution

By taking into account Coulomb collisions, we can consider the main effect—the angular electron scattering. Meanwhile, the changes in electron energy during Coulomb collisions are small compared to the energy changes due to the more frequent particle reflections from the moving magnetic mirrors. This effect was included in the collisionless solution (8). Therefore, retaining only the angular part of the collision operator in Eq. (15), we consider the simpler equation

$$\tau_s\frac{\partial F}{\partial t} = \frac{1}{x^3}\frac{\partial}{\partial \mu}\left(1-\mu^2\right)\frac{\partial F}{\partial \mu}. \quad (16)$$

Using the standard method of separation of variables, we seek a solution of Eq. (16) in the form

$$F(t,\mu) = X(t)Y(\mu).$$

We obtain the equation

$$\frac{\partial X}{\partial t} + \frac{1}{\tau_s}\frac{\lambda}{x^3}X = 0$$

for the time dependence and the Legendre equation

$$\frac{\partial}{\partial \mu}\left(1-\mu^2\right)\frac{\partial Y}{\partial \mu} + \lambda Y = 0$$

for the angular dependence, where λ is the separation constant. Using definition (1), we obtain the sought-for solution

$$F(l,\mu) = \sum_{n=o}^{\infty} Q_n \exp\left[\frac{t_o}{\tau_s}\frac{\lambda_n}{x^3}(1-l)\right]P_n(\mu), \quad (17)$$

where $P_n(\mu)$ are Legendre polynomials of the first kind, $\lambda_n = n(n+1)$, $n = 0, 1, 2, \ldots$. The coefficients Q_n can be determined from the condition that

the derived solution (17) for $\tau_s^{-1} = 0$ transforms into the collisionless solution (10). Finally, we have

$$\Theta^{-1}(\mu_{cr} - \mu)A(l)^{-1}e^{x^2}F = 1 + \frac{x^2}{3}(1 - l^2) \quad (18)$$
$$\times \left[1 - e^{-\alpha(1-l)}\right] + \mu^2 x^2 \left(1 - l^2\right) e^{-\alpha(1-l)},$$

where

$$\alpha = \frac{6}{x^3}\frac{t_o}{\tau_s}.$$

We see from (10) and (18) that collisions cause the anisotropic ($\sim \mu^2$) addition to decrease. Electron scattering gives rise to an additional isotropic component—the second term on the right-hand side of Eq. (18).

In the case of the initial acceleration stage under consideration, weak isotropization takes place in a collapsing trap for $x = 2$, $l = 0.9$, and $t_o = 10$ s: $\alpha(1 - l) \simeq 0.1$. This is because the isotropization time scale determined by the collision time $\tau_s \simeq 8$ s is too large. It exceeds the loss-cone depletion time $t_c = L/2v = 0.2$ s.

Possible Restrictions on the Particle Acceleration

So far we have considered the approximation of an ideal magnetic trap with $\beta \ll 1$, where β is the gaseous-to-magnetic pressure ratio. Theoretically, such a trap with an initial length L_o between the mirrors converging at velocity v_m has the lifetime t_o (1). Meanwhile, the longitudinal velocity of the accelerated plasma particles rises and the longitudinal particle temperature increases hyperbolically: $T_{||} = T_{o||}/l^2$. As l decreases, the particle density in the trap

$$\frac{n(l)}{n_o} = \frac{R}{\sqrt{1 + R^2 l^2}},$$

the longitudinal gaseous pressure of the accelerated particles

$$P_{||}(l) = 2n(l)k_B T_{||} = 2n_o k_B T_{o||}\frac{R}{l^2\sqrt{1 + R^2 l^2}},$$

and the plasma parameter

$$\beta = \frac{8\pi P_{||}}{B_1^2} = \frac{\beta_{||}(1)}{l^2}\sqrt{\frac{1 + R^2}{1 + R^2 l^2}}$$

increase. When the parameter $\beta_{||}$ reaches a critical value, the inverse effect of the accelerated particles on the magnetic field trap becomes significant.

Let us estimate the length l_{cr} by assuming the critical value to be $\beta_{||} = 1$. At the initial time, $l = 1$ for a solar flare with $n_o \approx 2 \times 10^9$ cm^{-3}, $T_o \approx 10^8$ K, and $B_1 \approx 10$ G, $B_2 \approx 40$ G (the last two parameters correspond to an adiabatic shock wave). In that case, $\beta_{||}(1) \approx 0.03$. However, as the length l decreases, this parameter increases and reaches unity even at $l_{cr} \approx 0.24$. The corresponding maximum longitudinal temperature is $T_{||} \approx 1.3 \times 10^9$ K. A further particle acceleration seems problematic, because a further rise in the pressure of the accelerated particles can lead to the instability and destruction of the magnetic flux tube long before collapse.

An alternative putative scenario is associated with the possible effect of the accelerated particles on the shock front. If the mirror ratio B_1/B_2 decreases with decreasing l, then the particle flux into the loss cone increases and the gas pressure drops. Further, if the shock front with converging mirrors is restored, then the acceleration process resumes before $\beta \sim 1$ is reached. A critical situation arises again and the process is repeated. The particle acceleration takes place in a pulsating regime. In addition, a stopped-front regime, when the mirror motion and, accordingly, the acceleration cease and the trap passes to a quasi-steady-state regime with thermal balance, is also possible, in principle. The hot sources at the tops of the X-ray and radio magnetic loops may be associated with this effect. The trap dynamics can be accompanied by an increase in plasma diamagnetism, which decreases the magnetic field in the central part of the trap, and by a rise in the flux of precipitating energetic particles, which is tantamount to loop cooling.

However, in studying the dynamic properties of a collapsing magnetic trap, it is important to take into account the rapid plasma cooling behind the shock front (Bogachev *et al.* 1998). In the regime of rapid cooling, plasma compression leads to a sharp increase in the mirror ratio and, accordingly, an improvement of the acceleration conditions in the collapsing trap.

CONCLUSIONS

When particular acceleration mechanisms in a cosmic plasma are considered, the role of Coulomb collisions generally reduces to the energy losses of the accelerated particles and, in particular, to the presence of a "loss barrier" at low velocities (see, e.g., Korchak 1980; Bykov *et al.* 2000). As a result, Coulomb collisions decrease the efficiency of any acceleration mechanism. In magnetic traps with stationary mirrors, Coulomb collisions inevitably produce a leakage of particles from the trap attributable to the particle diffusion into the loss cone. Contrary to the aforesaid, we showed here that Coulomb collisions in collapsing magnetic traps play a much less trivial and not so passive role.

We analyzed the effect of Coulomb collisions on the formation of the distribution function of the accelerated electrons in a magnetic trap with converging mirrors in the regime of rare collisions. In the collisionless case, as the trap length decreases, the anisotropy increases because of the increase in longitudinal particle velocity. At the same time, Coulomb collisions of the accelerated particles result in their scattering, i.e., in isotropization of the angular distribution. Thus, Coulomb collisions increase the volume of the region of phase space of the electrons involved in the acceleration. In other words, Coulomb collisions cause an increase in the fraction of the trapped electrons, an increase in the electron acceleration time, and a significant rise in the acceleration efficiency.

Since the collision frequency decreases with increasing particle velocity, Coulomb collisions are most efficient at low velocities. In contrast, the efficiency of the Fermi acceleration mechanism increases with velocity. Coulomb collisions help the Fermi acceleration mechanism in such an unexpected way precisely where this help is actually needed. Our conclusions can serve as a test for more complete numerical models. As examples of numerical calculations that are close to the model under discussion, we point out the studies of Zharkova *et al.* (1995) and Wu *et al.* (2000).

When analyzing the particle acceleration in a dynamic collapsing magnetic trap, one should take into account the inverse effect of the accelerated particles on the trap. This effect can result in a rearrangement of the acceleration regime, its cessation, or even the destruction of the magnetic trap. A more complex self-consistent model, whose development is well beyond the scope of this paper, is required to investigate these processes.

ACKNOWLEDGMENTS

This study was supported by the Russian Foundation for Basic Research, project nos. 02-02-16201 and 99-02-16344.

REFERENCES

1. M. A. Aschwanden, *Particle Acceleration and Kinematics in Solar Flares: A Synthesis of Recent Observations and Theoretical Concepts* (Kluwer Acad. Publ., Dordrecht, 2002), p. 227.
2. S. A. Bogachev and B. V. Somov, Astron. Zh. **78**, 187 (2001) [Astron. Rep. **45**, 157 (2001)].
3. S. A. Bogachev and B. V. Somov, Izv. Ross. Akad. Nauk, Ser. Fiz. **63**, 1555 (1999).
4. S. A. Bogachev, B. V. Somov, and S. Masuda, Pis'ma Astron. Zh. **24**, 631 (1998) [Astron. Lett. **24**, 543 (1998)].
5. G. I. Budker, Fiz. Plazmy Probl. Upravl. Termoyad. Reaktsiĭ **3**, 3 (1958).
6. A. M. Bykov, R. A. Chevalier, D. C. Ellison, and Yu. A. Uralov, Astrophys. J. **538**, 203 (2000).
7. E. Fermi, Astrophys. J. **119**, 1 (1954).
8. A. A. Korchak, Solar Phys. **66**, 149 (1980).
9. V. A. Kovalev and O. S. Korolev, Astron. Zh. **58**, 383 (1981).
10. V. A. Kovalev and B. V. Somov, Pis'ma Astron. Zh. **28**, 554 (2002) [Astron. Lett. **28**, 488 (2002)].
11. V. A. Kovalev and B. V. Somov, Pis'ma Astron. Zh. **29**, 132 (2003) [Astron. Lett. **29**, 111 (2003)].
12. D. E. McKenie and H. S. Hudson, Astrophys. J. Lett. **519**, L93 (1999).
13. V. P. Pastukhov, Vopr. Teor. Plazmy **13**, 160 (1984).
14. M. N. Rosenbluthe, W. McDonald, and D. Judd, Phys. Rev. **107**, 1 (1957).
15. D. V. Sivukhin, Vopr. Teor. Plazmy **4**, 81 (1964).
16. B. V. Somov, *Cosmic Plasma Physics* (Kluwer Academic Publ., Dordrecht, 2000), p. 652.
17. B. V. Somov and T. Kosugi, Astrophys. J. **485**, 859 (1997).
18. B. V. Somov, T. Kosugi, H. S. Hudson, *et al.*, Astrophys. J. **579**, 863 (2002).
19. B. V. Somov, T. Kosugi, and T. Sakao, Astrophys. J. **497**, 943 (1998).
20. D. S. Spicer and A. G. Emslie, Astrophys. J. **330**, 997 (1988).
21. B. A. Trubnikov, Vopr. Teor. Plazmy **1**, 98 (1963).
22. B. A. Trubnikov, Zh. Éksp. Teor. Fiz. **34**, 1341 (1958) [Sov. Phys. JETP **7**, 926 (1958)].
23. G. Wu, A. X. Xu, and G. Huang, Astrophys. Rep. **36**, 99 (2000).
24. V. V. Zharkova, J. C. Brown, and D. V. Syniavskii, Astron. Astrophys. **304**, 284 (1995).

Translated by V. Astakhov

Astronomy Letters, Vol. 29, No. 6, 2003, pp. 416–423. Translated from Pis'ma v Astronomicheskiĭ Zhurnal, Vol. 29, No. 6, 2003, pp. 473–480.

A Method for Averaging the Perturbing Function in Hill's Problem

M. A. Vashkov'yak*

Keldysh Institute of Applied Mathematics, Russian Academy of Sciences, Miusskaya pl. 4, Moscow, 125047 Russia

Received January 8, 2003

Abstract—A modified method for averaging the perturbing function in Hill's problem is suggested. The averaging is performed in the revolution period of the satellite over the mean anomaly of its motion with a full allowance for a variation in the position of the perturbing body. At its fixed position, the semimajor axis of the satellite orbit during the revolution of the satellite is constant in view of the evolution equations, while the remaining orbital elements undergo secular and long-period perturbations. Therefore, when the motion of the perturbing body is taken into account, the semimajor axis of the satellite orbit undergoes the strongest perturbations. The suggested approach generalizes the averaging method in which only the linear (in time) term is included in the perturbing function. This method requires no expansion in powers of time. The described method is illustrated by calculating the perturbations of the semimajor axes for two distant satellites of Saturn, S/2000 S1 and S/2000 S5. An approximate analytic solution is compared with the results of numerical integration of the averaged system of equations of motion for these satellites.

Key words: *Hill's problem, averaging of perturbing function, Saturn's satellites.*

INTRODUCTION: FORMULATION OF THE PROBLEM

Various methods for substituting the complete perturbing function R with its average are used to analyze the evolution of orbits in the restricted three-body problem. Thus, in analyzing the evolution on time scales much longer than the revolution periods of a zero-mass point P and a perturbing point P' and when their mean motions are incommensurable, independent double averaging over the mean longitudes λ and λ' of points P and P', respectively, is used in the first approximation of the perturbation theory. This Gaussian averaging scheme requires calculating the integral

$$W(a,e,i,\omega) = \frac{1}{4\pi^2}\int_0^{2\pi}\int_0^{2\pi} R(a,e,i,\omega,\Omega,\lambda,\lambda')d\lambda d\lambda'. \quad (1)$$

Here, a and e are the semimajor axis and eccentricity of the orbit of point P, respectively; and i and ω are the orbital inclination and the pericenter argument referred to the orbital plane of point P', respectively. In the simplest case, point P' is assumed to move in a circle of radius a' relative to a central attractive point S and perturb the Keplerian elliptical orbit of point P. In calculating integral (1), we assume that the orbital elements of point P (a, e, i, ω, Ω) are constant.

Single averaging of the perturbing function R only over the mean longitude λ of point P is used to analyze the evolution of the orbit of point P on time scales of the order of the revolution period of the perturbing point P' under the condition $a(1+e) < a'$ (the internal case of the problem). The corresponding averaging scheme of N.D. Moiseev (Moiseev 1945) requires calculating the integral

$$V(a,e,i,\omega,\Omega-\lambda') = \frac{1}{2\pi}\int_0^{2\pi} R(a,e,i,\omega,\Omega,\lambda,\lambda')d\lambda. \quad (2)$$

When calculating this integral, we assume that the orbital elements of point P (a, e, i, ω, Ω) are also constant; averaging over λ can be substituted with averaging over the mean anomaly M. The mean longitude λ' varies linearly with time, and the function R can be represented as a power series on small time scales:

$$R = R(t^*) + \frac{dR}{dt}(t-t^*) + \frac{1}{2}\frac{d^2R}{dt^2}(t-t^*)^2 + \ldots, \quad (3)$$

*E-mail: vashkov@spp.keldysh.ru

1063-7737/03/2906-0416$24.00

where t^* is the time that corresponds to a particular current position of point P within the revolution (e.g., its passage through the apocenter). This approach was first applied by M.L. Lidov, who used averaging of the perturbing accelerations (which is equivalent to averaging of the perturbing function) to calculate the gravitational perturbations of planetary satellites (Lidov 1961), and by Batrakov and Chernetenko (1994). Note that if only the first term is retained in series (3), then the problem becomes conservative ($\partial R/\partial M = 0$) and, as a result, the semimajor axis a of the orbit of point P remains constant. Actual perturbations of the semimajor axis can be revealed only by taking into account the remaining terms of this series.

Here, we suggest a method for calculating the averaged perturbing function of Hill's problem in closed form without using any expansion in powers of time. An approximate solution of the equation

$$\frac{da}{dt} = \frac{2}{na}\frac{\partial V}{\partial M_0}, \tag{4}$$

where n and M_0 are the mean motion of point P and its mean anomaly at initial epoch t_0, respectively, allows us to determine the perturbations of the semimajor axis of the orbit of point P attributable to the motion of the perturbing point P'.

Consider the satellite case of the restricted circular three-body problem, which is also called Hill's problem, where point P moves near a central point S of mass m so that the following condition is satisfied:

$$a(1+e) \ll a'. \tag{5}$$

A perturbing point P' of mass m' moves in a circular orbit of radius a', and its orbital plane is taken as the principal coordinate plane (xSy). The perturbing function of the problem is

$$R(a,e,i,\omega,\Omega,M,\lambda') = R_0(a,e,i,\omega,\Omega,M) + R_1(a,e,i,\omega,\Omega,M,\lambda'), \tag{6}$$

where

$$R_0(a,e,i,\omega,\Omega,M) = \frac{\mu'}{2a'^3}\left[\frac{3}{2}(x^2+y^2) - r^2\right], \tag{7}$$

$$R_1(a,e,i,\omega,\Omega,M,\lambda') = \frac{3\mu'}{4a'^3}\left[\left(x^2-y^2\right)\cos 2\lambda' + 2xy\sin 2\lambda'\right]. \tag{8}$$

Here, μ' is the product of the gravitational constant and the mass of the perturbing point; r is the radius vector of the satellite; and x and y are its Cartesian coordinates, which are related to the orbital elements by the standard formulas of unperturbed Keplerian elliptical motion and which are 2π-periodic functions of the mean longitude λ, the mean anomaly M, and the eccentric anomaly E:

$$\frac{1}{a}\begin{pmatrix} x \\ y \end{pmatrix} = (\cos E - e)\begin{pmatrix} P_1 \\ P_2 \end{pmatrix} + \sqrt{1-e^2}\begin{pmatrix} Q_1 \\ Q_2 \end{pmatrix}\sin E, \quad \frac{r}{a} = 1 - e\cos E, \tag{9}$$

$$P_1 = \cos\Omega\cos\omega - \sin\Omega\sin\omega\cos i, \quad Q_1 = \frac{\partial P_1}{\partial\omega}, \tag{10}$$

$$P_2 = \sin\Omega\cos\omega + \cos\Omega\sin\omega\cos i, \quad Q_2 = \frac{\partial P_2}{\partial\omega}.$$

The mean longitude λ' of the perturbing point depends linearly on time and, consequently, on M and M_0 via the formulas

$$\lambda' = \lambda'_0 + n'(t-t_0) = \lambda'_0 + \delta(M - M_0), \tag{11}$$

where

$$\delta = \frac{n'}{n}, \quad n' = \frac{\sqrt{\mu+\mu'}}{a'^{3/2}}, \quad n = \frac{\sqrt{\mu}}{a^{3/2}},$$

and μ is the product of the gravitational constant by the mass of the central point.

The perturbing function V averaged over the satellite revolution can be obtained more easily by averaging over the eccentric anomaly E of the satellite (given that it is related to M by Kepler's equation $E - e\sin E = M$):

$$V(a,e,i,\omega,\Omega,M_0) = V_0(a,e,i,\omega) + V_1(a,e,i,\omega,\Omega,M_0), \tag{12}$$

where

$$V_0 = \frac{1}{2\pi}\int_0^{2\pi} R_0(E)(1-e\cos E)dE, \tag{13}$$

$$V_1 = \frac{1}{2\pi}\int_0^{2\pi} R_1(E,\lambda')(1-e\cos E)dE. \tag{14}$$

The function R_1 depends not only on the elements in (12) but also on the rapid variable

$$\lambda' = \lambda'_0 + \delta(E - e\sin E - M_0). \tag{15}$$

CALCULATING THE AVERAGED PERTURBING FUNCTION

The standard expression for the function V_0 can be taken, in particular, from Lidov (1961) and Kozai (1962):

$$V_0 = \frac{\mu'}{a'^3}a^2 G(e,i,\omega), \tag{16}$$

where

$$G(e,i,\omega)=\frac{3}{8}\left[\frac{2}{3}+e^2-\sin^2 i+\frac{1}{2}e^2\sin^2 i\,(5\cos 2\omega-3)\right]. \quad (17)$$

Introducing a new integration variable to simplify the subsequent calculations,

$$\xi=E-\pi, \quad (18)$$

we derive the following general expression for the function V_1:

$$V_1=\frac{\mu' a^2}{4\pi a'^3}\int\limits_{-\pi}^{\pi} f(\xi,\cos\xi,\sin\xi)d\xi, \quad (19)$$

where f is a polynomial function of the above variables. Since the part of this function that is odd in ξ vanishes when integrated from $-\pi$ to π, retaining only the terms that are even in ξ in the integrand f, we obtain

$$V_1=\frac{\mu' a^2}{2\pi a'^3}\int\limits_0^{\pi}\left\{\sum_{k=0}^{3}(-1)^k\bar{A}_k\cos^k\xi\times\cos\left[2\delta(\xi+e\sin\xi)\right]+\bar{A}_4[(1+e^2)\cos\xi+e(1+\cos^2\xi)]\sin[2\delta(\xi+e\sin\xi)]\sin\xi\right\}d\xi. \quad (20)$$

Here,

$$\bar{A}_k=A_k\cos 2D+B_k\sin 2D,\quad k=0,1,2,3,$$
$$\bar{A}_4=B_4\cos 2D-A_4\sin 2D,$$
$$D=\lambda_0'+\delta(\pi-M_0),$$

and the coefficients A_k, B_k are defined by the formulas

$$A_0=\frac{3}{2}\left[e^2\left(P_1^2-P_2^2\right)+\left(1-e^2\right)\left(Q_1^2-Q_2^2\right)\right], \quad (21)$$

$$A_1=\frac{3}{2}e[\left(2+e^2\right)\left(P_2^2-P_1^2\right)+\left(1-e^2\right)\left(Q_2^2-Q_1^2\right)],$$

$$A_2=\frac{3}{2}[(1+2e^2)\left(P_1^2-P_2^2\right)+\left(1-e^2\right)\left(Q_2^2-Q_1^2\right)],$$

$$A_3=\frac{3}{2}e\left[\left(P_2^2-P_1^2\right)+\left(1-e^2\right)\left(Q_1^2-Q_2^2\right)\right],$$

$$A_4=3\sqrt{1-e^2}\left(P_1Q_1-P_2Q_2\right),$$

$$B_0=3\left[e^2P_1P_2+\left(1-e^2\right)Q_1Q_2\right],$$

$$B_1=-3e\left[(2+e^2)P_1P_2+\left(1-e^2\right)Q_1Q_2\right],$$

$$B_2=3\left[(1+2e^2)P_1P_2-\left(1-e^2\right)Q_1Q_2\right],$$

$$B_3=3e\left[-P_1P_2+\left(1-e^2\right)Q_1Q_2\right],$$

$$B_4=3\sqrt{1-e^2}(P_1Q_2+P_2Q_1).$$

Using expressions for the powers of trigonometric functions in terms of the functions of multiple arguments, we obtain

$$V_1=\frac{\mu' a^2}{2\pi a'^3}\sum_{l=\pm1}\sum_{k=k^*}^{3}C_{k,l}\times\int\limits_0^{\pi}\cos[(k+2l\delta)\xi+2l\delta e\sin\xi]d\xi. \quad (22)$$

Here,

$$k^*=(1-l)/2,\quad C_{k,l}=G_{k,l}\cos\varphi+H_{k,l}\sin\varphi, \quad (23)$$

$$\varphi=2(\Omega-D)=2[\Omega-\lambda_0'+\delta(M_0-\pi)],$$

$$G_{k,l}=\hat{G}_{k,l}+\bar{G}_{k,l}\cos 2\omega,\quad H_{k,l}=\bar{H}_{k,l}\sin 2\omega,$$

and the coefficients $\hat{G}_{k,l}$, $\bar{G}_{k,l}$, $\bar{H}_{k,l}$ can be expressed in terms of the orbital elements as

$$\hat{G}_{0,1}=\frac{3}{8}(2+3e^2)\sin^2 i,\bar{G}_{0,1}=\frac{15}{8}e^2(2-\sin^2 i),$$

$$\bar{H}_{0,1}=-\frac{15}{4}e^2\cos i,$$

$$\hat{G}_{1,-1}=\frac{9}{32}e(4+e^2)\sin^2 i,\quad \bar{G}_{1,-1}=\frac{3}{32}e[20+2e^2-10\sin^2 i-5e^2\sin^2 i+20\sqrt{1-e^2}\cos i],$$

$$\bar{H}_{1,-1}=-\frac{15}{16}e[(2+e^2)\cos i+\sqrt{1-e^2}(2-\sin^2 i)],$$

$$\hat{G}_{1,1}=\hat{G}_{1,-1},$$

$$\bar{G}_{1,1}=\frac{3}{32}e[20+2e^2-10\sin^2 i-5e^2\sin^2 i-20\sqrt{1-e^2}\cos i],$$

$$\bar{H}_{1,1}=-\frac{15}{16}e[(2+e^2)\cos i-\sqrt{1-e^2}(2-\sin^2 i)],$$

$$\hat{G}_{2,-1}=\frac{9}{16}e^2\sin^2 i,\quad \bar{G}_{2,-1}=\frac{3}{16}[4+2e^2-2\sin^2 i-e^2\sin^2 i+4(1+e^2)\sqrt{1-e^2}\cos i],$$

$$\bar{H}_{2,-1} = -\frac{3}{8}[(2+e^2)\cos i - (1+e^2) \times \sqrt{1-e^2}(2-\sin^2 i)], \quad \hat{G}_{2,1} = \hat{G}_{2,-1}, \tag{24}$$

$$\bar{G}_{2,1} = \frac{3}{16}[4+2e^2-2\sin^2 i - e^2\sin^2 i - 4(1+e^2)\sqrt{1-e^2}\cos i],$$

$$\bar{H}_{2,1} = -\frac{3}{8}[(2+e^2)\cos i + (1+e^2)\sqrt{1-e^2}(2-\sin^2 i)],$$

$$\hat{G}_{3,-1} = \frac{3}{32}e^3\sin^2 i, \quad \bar{G}_{3,-1} = \frac{3}{32}e[4-2e^2 - 2\sin^2 i + e^2\sin^2 i + 4\sqrt{1-e^2}\cos i],$$

$$\bar{H}_{3,-1} = \frac{3}{16}e[(e^2-2)\cos i - \sqrt{1-e^2}(2-\sin^2 i)], \quad \hat{G}_{3,1} = \hat{G}_{3,-1},$$

$$\bar{G}_{3,1} = \frac{3}{32}e[4-2e^2-2\sin^2 i + e^2\sin^2 i - 4\sqrt{1-e^2}\cos i],$$

$$\bar{H}_{3,1} = \frac{3}{16}e[(e^2-2)\cos i + \sqrt{1-e^2}(2-\sin^2 i)].$$

We derived formulas (22)–(24) by substituting expressions (10) into (21) and taking into account (18) and (20).

The definite integral in formula (22) can be calculated by using special functions.

We have from reference books

$$\int_0^\pi \cos(\nu\xi - z\sin\xi)d\xi = \pi\mathbf{J}_\nu(z), \tag{25}$$

where $\mathbf{J}_\nu(z)$ is the Anger function, which is a generalization of the Bessel function for noninteger values of the parameter ν. In addition, the Anger functions are known to be related to the Lommel ($s_{\rho,\nu}(z)$) and hypergeometric $F(\alpha,\beta,\gamma;\zeta)$ functions:

$$\mathbf{J}_\nu(z) = \frac{1}{\pi}\sin\nu\pi[s_{0,\nu}(z) - \nu s_{-1,\nu}(z)], \tag{26}$$

$$s_{\rho,\nu}(z) = \frac{z^{\rho+1}}{(\rho-\nu+1)(\rho+\nu+1)} \times F(1, \frac{\rho-\nu+3}{2}, \frac{\rho+\nu+3}{2}; -\frac{z^2}{4}). \tag{27}$$

In the latter expression, none of the numbers $\rho \pm \nu$ are integers.

In our case,

$$\nu = k + 2l\delta; \quad z = -2l\delta e; \quad \rho = 0, -1, \tag{28}$$

and, in addition, the following equalities hold for $l = \pm 1$:

$$-\frac{z^2}{4} = -\delta^2 e^2$$

and

$$\sin\nu\pi = (-1)^k \sin 2l\delta\pi = (-1)^k l \sin 2\delta\pi.$$

Transforming expression (22) yields the final formula for the perturbing function V of Hill's problem averaged over the satellite revolution:

$$V = \frac{\mu' a^2}{a'^3}\left\{G + \frac{\sin 2\pi\delta}{2\pi}\sum_{l=\pm1}\sum_{k=k^*}^{3}\Phi_{k,l} \times \left[\left(\hat{G}_{k,l} + \bar{G}_{k,l}\cos 2\omega\right)\cos\varphi + \bar{H}_{k,l}\sin 2\omega\sin\varphi\right]\right\}, \tag{29}$$

where

$$\Phi_{k,l}(e) = (-1)^k\left[\frac{l}{\nu}F\left(1, \frac{2-\nu}{2}, \frac{2+\nu}{2}; -\delta^2e^2\right) - \frac{2\delta e}{1-\nu^2}F\left(1, \frac{3-\nu}{2}, \frac{3+\nu}{2}; -\delta^2e^2\right)\right], \tag{30}$$

$\varphi(\Omega, M_0, \lambda_0')$, $\hat{G}_{k,l}(e,i)$, $\bar{G}_{k,l}(e,i)$, $\bar{H}_{k,l}(e,i)$ are given by formulas (23), (24).

THE DERIVATIVES OF THE AVERAGED PERTURBING FUNCTION WITH RESPECT TO ORBITAL ELEMENTS

Since we are not concerned with the specific position of the satellite in its orbit in the averaged problem, we can eliminate the equation for the variation of M_0 from the system of six evolution equations and, hence, do not need to calculate the derivative of V with respect to a.

The derivatives of the function V with respect to Ω and M_0 are easiest to calculate, because only the angle φ depends on these elements. Therefore,

$$\frac{\partial V}{\partial\Omega} = 2\frac{\partial V}{\partial\varphi}, \quad \frac{\partial V}{\partial M_0} = 2\delta\frac{\partial V}{\partial\varphi}, \tag{31}$$

where

$$\frac{\partial V}{\partial\varphi} = \frac{\mu' a^2\sin 2\pi\delta}{2\pi a'^3}\sum_{l=\pm1}\sum_{k=k^*}^{3}\Phi_{k,l}[-(\hat{G}_{k,l} + \bar{G}_{k,l}\cos 2\omega)\sin\varphi + \bar{H}_{k,l}\sin 2\omega\cos\varphi]. \tag{32}$$

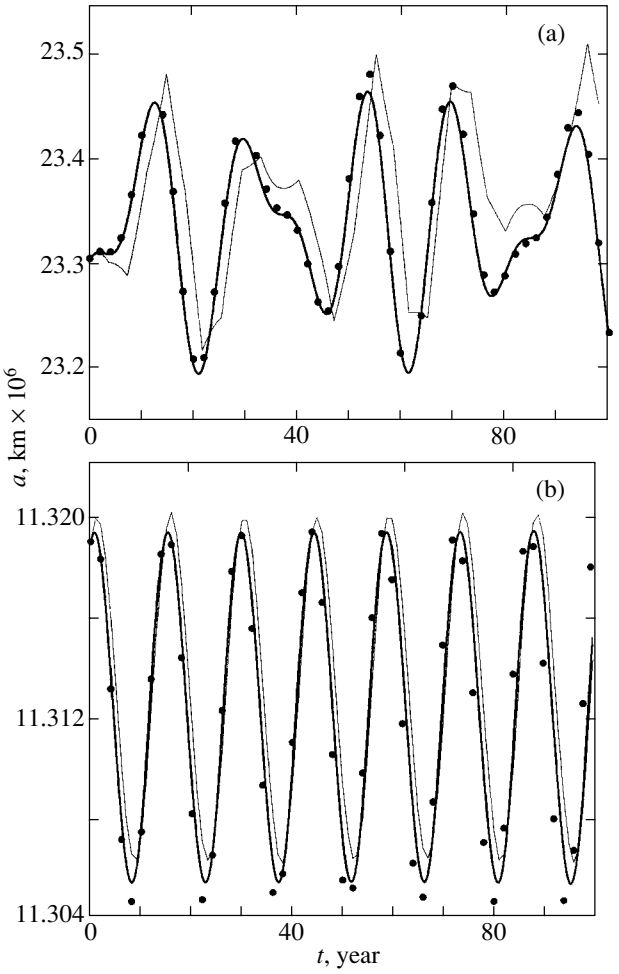

Time variations in the orbital semimajor axis for the satellites (a) S/2000 S1 (ω circulation) and (b) S/2000 S5 (ω libration).

The derivative of V with respect to ω is also easy to determine:

$$\frac{\partial V}{\partial \omega} = \frac{\mu' a^2}{a'^3}\left\{-\frac{15}{8}e^2\sin^2 i\sin 2\omega + \frac{\sin 2\pi\delta}{\pi}\sum_{l=\pm1}\sum_{k=k^*}^{3}\Phi_{k,l}[-\bar{G}_{k,l}\sin 2\omega\cos\varphi + \bar{H}_{k,l}\cos 2\omega\sin\varphi]\right\}.$$

The derivative of V with respect to i can be calculated using the formula

$$\frac{\partial V}{\partial i} = \frac{\mu' a^2}{a'^3}\left\{\frac{\partial G}{\partial i} + \frac{\sin 2\pi\delta}{2\pi} \times \sum_{l=\pm1}\sum_{k=k^*}^{3}\Phi_{k,l}\left[\left(\frac{\partial \hat{G}_{k,l}}{\partial i} + \frac{\partial \bar{G}_{k,l}}{\partial i}\cos 2\omega\right)\cos\varphi + \frac{\partial \bar{H}_{k,l}}{\partial i}\sin 2\omega\sin\varphi\right]\right\},$$

where

$$\frac{\partial G}{\partial i} = \frac{3}{8}\left[e^2(5\cos 2\omega - 3) - 2\right]\sin i\cos i,$$

$$\frac{\partial \hat{G}_{0,1}}{\partial i} = \frac{3}{4}\left(2 + 3e^2\right)\sin i\cos i,$$

$$\frac{\partial \bar{G}_{0,1}}{\partial i} = -\frac{15}{4}e^2\sin i\cos i,$$

$$\frac{\partial \bar{H}_{0,1}}{\partial i} = \frac{15}{4}e^2\sin i,$$

$$\frac{\partial \hat{G}_{1,-1}}{\partial i} = \frac{9}{16}e\left(4 + e^2\right)\sin i\cos i,$$

$$\frac{\partial \bar{G}_{1,-1}}{\partial i} = -\frac{15}{16}e\left[(2 + e^2)\cos i + 2\sqrt{1 - e^2}\right]\sin i,$$

$$\frac{\partial \bar{H}_{1,-1}}{\partial i} = \frac{15}{16}e\left(2 + e^2 + 2\sqrt{1 - e^2}\cos i\right)\sin i,$$

$$\frac{\partial \hat{G}_{1,1}}{\partial i} = \frac{\partial \hat{G}_{1,-1}}{\partial i},$$

$$\frac{\partial \bar{G}_{1,1}}{\partial i} = -\frac{15}{16}e\left[(2 + e^2)\cos i - 2\sqrt{1 - e^2}\right]\sin i,$$

$$\frac{\partial \bar{H}_{1,1}}{\partial i} = \frac{15}{16}e\left(2 + e^2 - 2\sqrt{1 - e^2}\cos i\right)\sin i,$$

$$\frac{\partial \hat{G}_{2,-1}}{\partial i} = \frac{9}{8}e^2\sin i\cos i,$$

$$\frac{\partial \bar{G}_{2,-1}}{\partial i} = -\frac{3}{8}\left[(2 + e^2)\cos i + 2(1 + e^2)\sqrt{1 - e^2}\right]\sin i,$$

$$\frac{\partial \bar{H}_{2,-1}}{\partial i} = \frac{3}{8}\left[2 + e^2 - 2(1 + e^2)\sqrt{1 - e^2}\cos i\right]\sin i,$$

$$\frac{\partial \hat{G}_{2,1}}{\partial i} = \frac{\partial \hat{G}_{2,-1}}{\partial i},$$

$$\frac{\partial \bar{G}_{2,1}}{\partial i} = -\frac{3}{8}\left[(2 + e^2)\cos i - 2(1 + e^2)\sqrt{1 - e^2}\right]\sin i,$$

$$\frac{\partial \bar{H}_{2,1}}{\partial i} = \frac{3}{8}\left[2 + e^2 + 2(1+e^2)\sqrt{1-e^2}\cos i\right]\sin i,$$

$$\frac{\partial \hat{G}_{3,-1}}{\partial i} = \frac{3}{16}e^3 \sin i \cos i,$$

$$\frac{\partial \bar{G}_{3,-1}}{\partial i} = \frac{3}{16}e\left[(e^2-2)\cos i - 2\sqrt{1-e^2}\right]\sin i,$$

$$\frac{\partial \bar{H}_{3,-1}}{\partial i} = \frac{3}{16}e\left(2 - e^2 + 2\sqrt{1-e^2}\cos i\right)\sin i,$$

$$\frac{\partial \hat{G}_{3,1}}{\partial i} = \frac{\partial \hat{G}_{3,-1}}{\partial i},$$

$$\frac{\partial \bar{G}_{3,1}}{\partial i} = \frac{3}{16}e\left[(e^2-2)\cos i + 2\sqrt{1-e^2}\right]\sin i,$$

$$\frac{\partial \bar{H}_{3,1}}{\partial i} = \frac{3}{16}e\left(2 - e^2 - 2\sqrt{1-e^2}\cos i\right)\sin i.$$

The expression for the derivative of V with respect to e is the most cumbersome one:

$$\frac{\partial V}{\partial e} = \frac{\mu' a^2}{a'^3}\left\langle \frac{\partial G}{\partial e} + \frac{\sin 2\pi\delta}{2\pi} \times \sum_{l=\pm 1}\sum_{k=k^*}^{3}\left\{\Phi_{k,l}\left[\left(\frac{\partial \hat{G}_{k,l}}{\partial e} + \frac{\partial \bar{G}_{k,l}}{\partial e}\cos 2\omega\right)\cos\varphi + \frac{\partial \bar{H}_{k,l}}{\partial e}\sin 2\omega \sin\varphi\right] + \frac{d\Phi_{k,l}}{de}\left[(\hat{G}_{k,l} + \bar{G}_{k,l}\cos 2\omega)\cos\varphi + \bar{H}_{k,l}\sin 2\omega \sin\varphi\right]\right\}\right\rangle,$$

where

$$\frac{\partial G}{\partial e} = \frac{3}{4}e\left[1 + \frac{1}{2}\sin^2 i\,(5\cos 2\omega - 3)\right],$$

$$\frac{\partial \hat{G}_{0,1}}{\partial e} = \frac{9}{4}e\sin^2 i, \quad \frac{\partial \bar{G}_{0,1}}{\partial e} = \frac{15}{4}e(2 - \sin^2 i),$$

$$\frac{\partial \bar{H}_{0,1}}{\partial e} = -\frac{15}{2}e\cos i,$$

$$\frac{\partial \hat{G}_{1,-1}}{\partial e} = \frac{9}{32}\left(4 + e^2\right)\sin^2 i,$$

$$\frac{\partial \bar{G}_{1,-1}}{\partial e} = \frac{3}{32}\left[20 + 6e^2 - 10\sin^2 i - 15e^2\sin^2 i + \frac{20\cos i}{\sqrt{1-e^2}}(1-2e^2)\right],$$

$$\frac{\partial \bar{H}_{1,-1}}{\partial e} = -\frac{15}{16} \times \left[\left(2 + 3e^2\right)\cos i + \frac{2-\sin^2 i}{\sqrt{1-e^2}}(1-2e^2)\right],$$

$$\frac{\partial \hat{G}_{1,1}}{\partial e} = \frac{\partial \hat{G}_{1,-1}}{\partial e},$$

$$\frac{\partial \bar{G}_{1,1}}{\partial e} = \frac{3}{32}\left[20 + 6e^2 - 10\sin^2 i - 15e^2\sin^2 i - \frac{20\cos i}{\sqrt{1-e^2}}(1-2e^2)\right],$$

$$\frac{\partial \bar{H}_{1,1}}{\partial e} = -\frac{15}{16}\left[\left(2 + 3e^2\right)\cos i - \frac{2-\sin^2 i}{\sqrt{1-e^2}}(1-2e^2)\right],$$

$$\frac{\partial \hat{G}_{2,-1}}{\partial e} = \frac{9}{8}e\sin^2 i,$$

$$\frac{\partial \bar{G}_{2,-1}}{\partial e} = \frac{3}{8}e\left[2 - \sin^2 i + \frac{2\cos i}{\sqrt{1-e^2}}(1-3e^2)\right],$$

$$\frac{\partial \bar{H}_{2,-1}}{\partial e} = -\frac{3}{8}e\left[2\cos i - \frac{2-\sin^2 i}{\sqrt{1-e^2}}(1-3e^2)\right],$$

$$\frac{\partial \hat{G}_{2,1}}{\partial e} = \frac{\partial \hat{G}_{2,-1}}{\partial e},$$

$$\frac{\partial \bar{G}_{2,1}}{\partial e} = \frac{3}{8}e\left[2 - \sin^2 i - \frac{2\cos i}{\sqrt{1-e^2}}(1-3e^2)\right],$$

$$\frac{\partial \bar{H}_{2,1}}{\partial e} = -\frac{3}{8}e\left[2\cos i + \frac{2-\sin^2 i}{\sqrt{1-e^2}}(1-3e^2)\right],$$

$$\frac{\partial \hat{G}_{3,-1}}{\partial e} = \frac{9}{32}e^2\sin^2 i,$$

$$\frac{\partial \bar{G}_{3,-1}}{\partial e} = \frac{3}{32}\left[4 - 6e^2 - 2\sin^2 i + 3e^2\sin^2 i + \frac{4\cos i}{\sqrt{1-e^2}}(1-2e^2)\right],$$

$$\frac{\partial \bar{H}_{3,-1}}{\partial e} = \frac{3}{16}\left[\left(3e^2 - 2\right)\cos i - \frac{2-\sin^2 i}{\sqrt{1-e^2}}(1-2e^2)\right], \quad \frac{\partial \hat{G}_{3,1}}{\partial e} = \frac{\partial \hat{G}_{3,-1}}{\partial e},$$

$$\frac{\partial \bar{G}_{3,1}}{\partial e} = \frac{3}{32}\left[4 - 6e^2 - 2\sin^2 i + 3e^2\sin^2 i - \frac{4\cos i}{\sqrt{1-e^2}}(1-2e^2)\right],$$

$$\frac{\partial \bar{H}_{3,1}}{\partial e} = \frac{3}{16}\left[\left(3e^2-2\right)\cos i + \frac{2-\sin^2 i}{\sqrt{1-e^2}}(1-2e^2)\right].$$

We differentiate the function $\Phi_{k,l}(e)$ using the standard relation

$$\frac{dF(\alpha,\beta,\gamma;z)}{dz} = \frac{\alpha\beta}{\gamma}F(\alpha+1,\beta+1,\gamma+1;z);$$

therefore,

$$\frac{d\Phi_{k,l}}{de} = 2(-1)^k\delta$$
$$\times\left[\frac{2\delta^2e^2(3-\nu)}{(1-\nu^2)(3+\nu)}F\left(2,\frac{5-\nu}{2},\frac{5+\nu}{2};-\delta^2e^2\right)\right.$$
$$-\frac{l\delta e(2-\nu)}{\nu(2+\nu)}F\left(2,\frac{4-\nu}{2},\frac{4+\nu}{2};-\delta^2e^2\right)$$
$$\left.-\frac{1}{1-\nu^2}F\left(1,\frac{3-\nu}{2},\frac{3+\nu}{2};-\delta^2e^2\right)\right].$$

Thus, this section contains the complete set of formulas required to explicitly calculate the partial derivatives of the function V with respect to the elements e, i, ω, Ω, and M_0 and the right-hand sides of the averaged equations that describe the evolution of the satellite orbit.

APPROXIMATE CALCULATION OF THE TIME DEPENDENCE OF THE SEMIMAJOR AXIS OF THE SATELLITE ORBIT

In this paper, we focus on the variation of the semimajor axis, which cannot be found if only the first term

$$V_0 = \frac{\mu' a^2}{a'^3}G \tag{33}$$

is retained in the function V (29).

Given formulas (31) and (32), Eq. (4) takes the form

$$\frac{da}{dt} = \frac{2\mu' a n' \sin 2\pi\delta}{\pi a'^3 n^2}\sum_{l=\pm1}\sum_{k=k^*}^{3}\Phi_{k,l} \tag{34}$$
$$\times\left[-\left(\hat{G}_{k,l}+\bar{G}_{k,l}\cos 2\omega\right)\sin\varphi\right.$$
$$\left.+\bar{H}_{k,l}\sin 2\omega\cos\varphi\right].$$

To properly apply the derived equation on a time scale longer than the satellite-revolution period T, the quantity φ should be assumed to be a discrete function of the satellite revolution number $m = 1 + E\left(\frac{t-t_0}{T}\right)$. Setting $M_0 = \pi$ (the initial position of the perturbing body corresponds to the time the satellite passes through the apocenter) and taking into account the fact that the mean longitude λ' changes by $n'T = 2\pi\frac{n'}{n} = 2\pi\delta$ in time T ($\Delta m = 1$), we conclude that φ should be calculated using the formula

$$\varphi = \left[\Omega - \lambda'_0 - 2(m-1)\pi\delta\right]. \tag{35}$$

For an approximate analysis, in the equations that describe the variations in the remaining satellite orbital elements e, i, ω, and Ω, we use the truncated expression (33) for the function V.

Thus, the standard system of four evolution equations for the double-averaged Hill problem, where a is assumed to be a variable quantity, is supplemented with the fifth equation (34) for the variation in the semimajor axis. Below, we compare the results by numerically integrating the averaged system constructed in this way both in the case of discrete φ variation, according to (35), and in the continuously differentiable case:

$$m = 1 + \frac{t-t_0}{T}, \tag{36}$$

$$\varphi = 2\left[\Omega - \lambda'_0 - 2\frac{t-t_0}{T}\pi\frac{n'}{n}\right] = 2\left[\Omega-\lambda'\right].$$

In this case, we can also derive the analytic dependence $a(t)$. We use dependence (36) and assume, to a first approximation, that the orbital elements a, e, and i on the right-hand side of Eq. (34) are constant and that the angular variables ω and Ω are linear functions of time:

$$\omega = \omega_0 + \dot{\omega}(t-t_0), \quad \Omega = \Omega_0 + \dot{\Omega}(t-t_0),$$

where

$$\dot{\omega} = \frac{2\pi}{T_\omega}, \quad \dot{\Omega} = \frac{2\pi}{T_\Omega}.$$

Integrating (34) under the above assumptions yields

$$a = a_0\left[1 + \frac{\mu' n' \sin 2\pi\delta}{\pi a'^3 n^2}\sum_{l=\pm1}\sum_{k=k^*}^{3}\Phi_{k,l}g(t)\right], \tag{37}$$

where

$$g(t) = \frac{1}{2\zeta}\left\{\frac{\bar{G}_{k,l}+\bar{H}_{k,l}}{1-\frac{\dot{\omega}}{\zeta}}\left[\cos(2\omega-\varphi)\right.\right. \tag{38}$$
$$\left.-\cos(2\omega_0-\varphi_0)\right] + \frac{\bar{G}_{k,l}-\bar{H}_{k,l}}{1+\frac{\dot{\omega}}{\zeta}}\left[\cos(2\omega+\varphi)\right.$$
$$\left.\left.-\cos(2\omega_0+\varphi_0)\right] + 2\hat{G}_{k,l}(\cos\varphi-\cos\varphi_0)\right\},$$

$$\zeta = \dot{\Omega} - n'.$$

In the case of librational variation in ω, we can roughly assume that $\omega = \pm\pi/2$ and $\dot{\omega} = 0$.

The figure compares the calculated variations in the orbital semimajor axes of two recently discovered Saturn's satellites. For the satellite S/2000 S1, $T_\Omega \approx 250$ years, $T_\omega \approx 146$ years, and ω exhibits circulation-type variations. For S/2000 S5, $T_\Omega \approx 838$ years and ω exhibits libration-type variations. The dots in the figure indicate the a values obtained from formulas (37) and (38). The solid lines represent the results obtained by numerically integrating the averaged system in elements (the thin lines correspond to discrete variation in φ and the heavy lines correspond to variation in φ according to formula (36)). On the century-long interval, the two figures show distinct variations (which are particularly discernible for the satellite S5) with a period equal to half the revolution period T' of the perturbing body (the Sun), or about 15 years. The variations for the satellite S5 with this period ($T \approx 1.23$ years) have an amplitude of about 8000 km. The corresponding amplitude for S1 ($T \approx 3.64$ years), which is Saturn's most distant discovered satellite and the one most strongly perturbed by the Sun, is about 150 000 km. The degree of closeness of the analytic and numerical solutions decreases with increasing δ.

CONCLUSIONS

Since the part of the perturbing function R_1 that depends on both E and λ' is not a periodic (or, to be more precise, is an almost periodic) function of E for arbitrary n and n', in general, a time average should be calculated when averaging it. This averaging operator is used in the generalized Delone–Hill scheme (Moiseev 1945) and involves calculating the integral

$$\bar{V} = \lim_{\tau\to\infty} \frac{1}{\tau} \int_0^\tau R[\lambda(t), \lambda'(t)]dt.$$

However, we can avoid calculating it on short time intervals by using function (29) and relations (35) and (36).

In actual motion, in addition to perturbations with a period $T'/2$, the semimajor axes of satellite orbits also undergo short-period perturbations with the satellite revolution periods. These perturbations can be determined only by constructing a complete analytic or numerical theory.

REFERENCES

1. Yu. V. Batrakov and Yu. A. Chernetenko, *Motion of Binary Comet*, Ed. by A. López García *et al.* (Astron. Observ. Univ. Valencia, 1994), p. 461.
2. Y. Kozai, Astron. J. **67**, 591 (1962).
3. M. L. Lidov, Issk. Sputniki Zemli **8**, 5 (1961).
4. N. D. Moiseev, Tr. Gos. Astron. Inst. Shternberga, **XV**, 1, 100 (1945).

Translated by A. Dambis